Doctoral Dissertation

Reinforced Effect on Brick Wall Using Timber Wall as a Retrofitting Method

(改修方法として木材壁を使用したレンガ壁への補強効果)

Department of Architecture
Graduate School of Engineering
Hiroshima University

Ariunaa Ganbaatar

2022 年 10 月

CONTENTS

LIST OF FIGURES

LIST OF TABLES

Acknowledgements

First, I would like to express my appreciation for my supervisor, Associate professor Takuro Mori for his experience, valuable advice, and knowledge. I am very grateful to my supervisor for leading my doctoral research by taking the first time to study the brick masonry structure and taking a big risk. I am proud and thankful for his courage. My deepest gratitude to Professor Naohiro Nakamura, Professor Hiroshi Tagawa, Associate Professor Shinya Matsumoto, and Associate Professor Hiroyuki Miura for guiding my research work during their busy working days.

I would like to express my thanks to Professor Sunjidmaa Danzandorj and other staff of the MJEED project, for supporting me during last three years.

I would like to thank deep gratitude to Ph.D candidate Ryo Inoue and our lab mates, who have always helped me with all the experiments during last three years.

I would like to express my deep gratitude to associate Professor Shinya Matsumoto at Kindai University for allowing us to test the brick wall's specimens.

Thank you, Professor Otgonbayar Peljee, Professor Duinkherjav Yagaanbuyant, Professor Ganzorig Erdene, Associate professor Oyunchimeg Mendbayar and Erdenebold Bayar, and MUST (Mongolian University of Science and Technology) workmates and other dearest people, I will always be in the depth of your help and encouragement.

Finally, I would like to thank my mother, my family, and friends who have encouraged me along the way.

ABSTRACT

There are many ways to strengthen an unreinforced brick masonry wall. One of the strengthening methods applies timber, which is a lightweight and easy installation. In this research, the strengthening method of brick wall is used with timber material. The main point of this research covers the material properties, the connection between brick and timber, and reinforced effect of the brick wall using timber wall.

Chapter I involves introduction, including background, literature review, objective, and method. Background section mentioned seismic assessment and failure caused by the earthquake to the unreinforced masonry buildings. In unreinforced masonry structures, retrofitting methods are carried out by various materials. In the literature review section including in-plane shear behavior, the results of a wood-reinforced study are presented. This study proposed a retrofitting method using timber and included the objective and method. To evaluate the proposed retrofitting method, the experimental and prediction estimation were carried out in this research.

Chapter II includes the material properties used in this study. The main material of this research is masonry material. Therefore, the clay brick, cement mortar, brick-mortar interface element and small masonry specimen were determined by experiment. Lumber, epoxy resin, and bolt's material properties were taken from applicable standards.

Chapter III consists of the strength properties of connection between brick and timber. The connection between timber and brick masonry wall plays an important role. In this study, the experimental and theoretical methods were investigated, and pullout and shear strengths of chemical anchor were employed as the connection between clay brick and SPF (spruce, pine, fir) lumber. Three bolt diameters (ø8, ø10, ø12 mm) were utilized in nine pullout tests and two types of eighteen shear tests. Four types of prediction models estimated the pullout strength of the chemical anchor. Prediction failure modes include steel failure, cone failure, bond failure and combined bond-cone failure. The European Yield Theory (EYT) expects the shear strength of the chemical anchor, involving six failure modes. The results of all experiments were discussed as failure mode, strength, and stiffness under monotonic load. Finally, the effective result of this study highlights A12 specimens using ø12 mm bolt and employing the epoxy resin in brick and lumber.

Chapter IV consists of the experimental result of the reinforced effect of the brick wall evaluated by the cyclic horizontal load. This research aimed to utilize timber material to enhance the in-plane shear strength and deformation capacity of the brick wall. The proposed strengthening method is light-weight and easy to assemble, and includes a timber frame, plywood

panel, M12 threaded rod with chemical epoxy, and the hold-down anchor. To evaluate the effectiveness of the strengthened brick wall, three walls, including the BW wall (the brick wall), BW-T wall (the strengthened brick wall with timber), and BW-TA wall (the strengthened brick wall with timber and the hold-down anchor), were tested under the cyclic horizontal load and the static compression load. Maximum horizontal load of BW and BW-T wall are almost same value. For BW-TA wall, horizontal load increased around 20 percent compared with BW wall's result. Three wall's initial stiffness shows same value. Drift angle of BW-TA defined by diagonal measurement was increased by 4.8 at maximum load compared with BW-T wall. BW and BW-T walls presented same failure mode which is rocking failure. Failure mode of BW-TA wall showed diagonal compression failure.

Chapter V covers the prediction of brick wall (BW wall) and reinforced brick wall with timber (BW-TA wall). In this study, the load-drift angle relationship of BW wall is predicted by the simple theories. Masonry wall was assumed by elastic and homogeneous. BW-TA wall was assessed by the proposed prediction calculation of Kamiya and Inayama Murakami model. The initial stiffness of prediction-1 (prediction-2) is 21% (14.7%) greater than the experimental stiffness. The ultimate horizontal load of prediction-1 (prediction-2) is 33% (same) greater than the experimental value. The proposed theoretical method (Kamiya and Inayama Murakami model) has shown good matching in results by determining the initial stiffness and the ultimate horizontal load of the BW-TA wall.

Chapter VI summarized the results, conclusions, limitations, and future study of this research. I proposed conclusions of material properties, pull-out and shear strength of brick and lumber connection, experimental and prediction of the unreinforced and reinforced brick wall. The future study is that this research will define the target strength of the reinforced brick wall with timber material and study will also contribute to the numerical analysis of the reinforced brick wall with timber. The proposed retrofitting method will be installed in the existing unreinforced brick buildings. The strengthening method of out-of-plane behavior in the masonry building will be proposed and carried out by the experimental and theoretical methods.

CHAPTER I.

INTRODUCTION

1.1. Background

The unreinforced masonry structures have a high risk of earthquakes, evidenced by postearthquake damages and research. The seismic evaluation of three to five-story buildings constructed in the 1970s was assessed because of the 2019 earthquake in Albania [5]. A push-over analysis was performed for each building, and the buildings showed a nonlinear response, and diagonal in-plane cracks appeared in most masonry buildings. The damage and failure of masonry structures were studied after the 2017 earthquake in Greece [6] and highlight the vulnerabilities that cause damage and the prevention factors. The study [2] also inspected the unreinforced and timber-reinforced masonry structures, and failure modes were observed in the in-plane, out-of-plane, and combined directions. After the Croatia earthquake in 2020 [7], site investigations of residential buildings were conducted, and they inspected postearthquake assessments, damage classifications, and failure patterns in the masonry buildings. There is research material on the damage to buildings and structures caused by strong earthquakes in other countries [8,9]. Based on the above earthquake lessons, it is important to predict a seismic assessment of the masonry buildings, determine the failure mechanism, and consider the possibility of the strengthening method. Severe damage to URM buildings due to seismic load is related to the composite material

characteristics of masonry structures, including brick and mortar. Masonry material has high compressive strength and low shear and tensile strength. Masonry walls can be easily broken based on the weak strength under horizontal loads. It is important to take countermeasures to reduce earthquake risk and prevent earthquake hazards. Therefore, it is inevitable to evaluate and carry out strengthening the unreinforced masonry buildings. Failure can develop in the in-plane and out-of-plane under the action of horizontal loads. The horizontal load can create a shear force and bending moment in the in-plane of the masonry wall. Due to the in-plane shear behavior, sliding and diagonal failures occur under the shear load, and rocking and crushing failure under the bending moment, respectively [1,10]. It is possible to happen the above failures individually or combined in the unreinforced masonry building have not been taken against seismic actions [6].

1.2. Literature review

Researchers and engineers [11–13] have been carrying out various methods to strengthen the unreinforced masonry buildings. The fundamental concept of strengthening/retrofitting approaches is to (i) reduce the influence of external loading, (ii) upgrade the individual element's load-carrying capacity, and (iii) improve the integrity of masonry structure [14].

There has been an increasing number of studies on the strengthening technique of using timber frames and panels for unreinforced masonry structures [15–17]. Timber stud [16] is used on seismic retrofit of masonry walls. In study [16], 90 mm × 45 mm timber studs were located in the unreinforced masonry wall to increase the out-of-plane capacity. Mechanical screws (D12/L230 mm) were used to secure the timber stud to the masonry wall. The timber frames and boards [15] were employed to strengthen the masonry piers. When fixing the wooden frame to the masonry wall, a 90 mm × 50 mm metal angle is connected to timber

with a 70 mm long screw, and a 10 mm threaded rod with chemical adhesive is connected to the masonry wall [15]. The two-story full-size unreinforced masonry building with an innovative timber retrofit was tested on the shake table [17]. Connecting the timber to the masonry structure, ø10 mm threaded rods were installed at a depth of 50 mm and fastened with epoxy resin. An on-site experiment [18]was conducted to strengthen the masonry structure, and two types of screws (M12/L180 and M10/L230) were tested to attach the cross laminated timber (CLT) panel to the masonry wall. The method of strengthening was able to increase the in-plane shear strength of the wall by 40 percent [18]. The study [19] carried out OSB board threaded dry rod, and the chemical anchor was connected to the masonry wall. The bolts were fixed to the masonry wall only, and the installation depth was 50 mm. The cross-laminated timber panel was used to strengthen the unreinforced masonry wall [20].

One of the most important aspects of timber structures is the connection. The bolt or screw fasteners were utilized to secure the unreinforced masonry wall to timber. There are two types of anchors, mechanical and chemical. The chemical anchor uses a threaded rod or reinforcing bar set in predrilled holes with adhesive compounds [21]. In a mechanical anchor system, forces on the heavily loaded anchor are generally transferred uniformly to the concrete along the length of the embedded portion of the anchor [22]. When estimating the strength of an anchor, two fundamental strengths act on the fastener. These include the pullout strength acting along with the bolt and the shear strength perpendicular to the bolt. The mechanical properties of metal anchors [23] were tested on historical stone masonry. The fastener types of metal, chemical, and mortar were inspected on tension and shear loads and compared with theoretical assumptions. The experimental result [23] concluded pullout

strength of the chemical anchor showed more values than the other two. The experimental study [24] identified the shear strength of five types of screw anchors, including ø12 mm, ø12.5, and ø16.6 mm threaded diameters for connecting masonry structures to wood. Dry screw anchors [24] have been a possible solution for connecting masonry and wood materials. It has been concluded that it may be better to use chemical adhesives for irregular stone masonry. The study [25] determined anchors' tensile and shear strength for limestone structures. Three different diameter bolts were tested with two bond agents (epoxy adhesive and cement-based grout) [25]. The tensile strength of the chemical anchor is greater than cement-based grout, and it was concluded that the shear strength showed similar values. An experimental study of pullout strength [26] was conducted on masonry walls, and the bolts were bonded with epoxy resin and were placed in the head and bed-joint and brick in the brick masonry wall. The test result [26] concluded that the bolt's pullout strength placed in the mortar was greater than the bricks'.

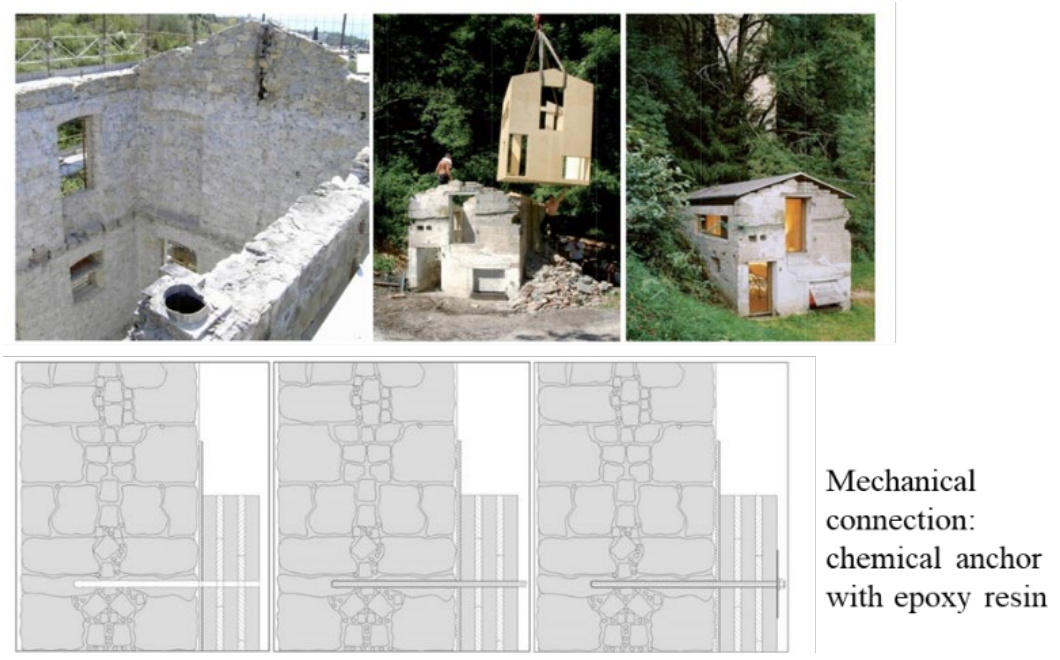

Facadism and CLT technology: An innovative system for masonry construction refurbishment (2014)

(a)

Seismic strengthening of existing concrete and masonry buildings with crosslam timber panels (2014)

(b)

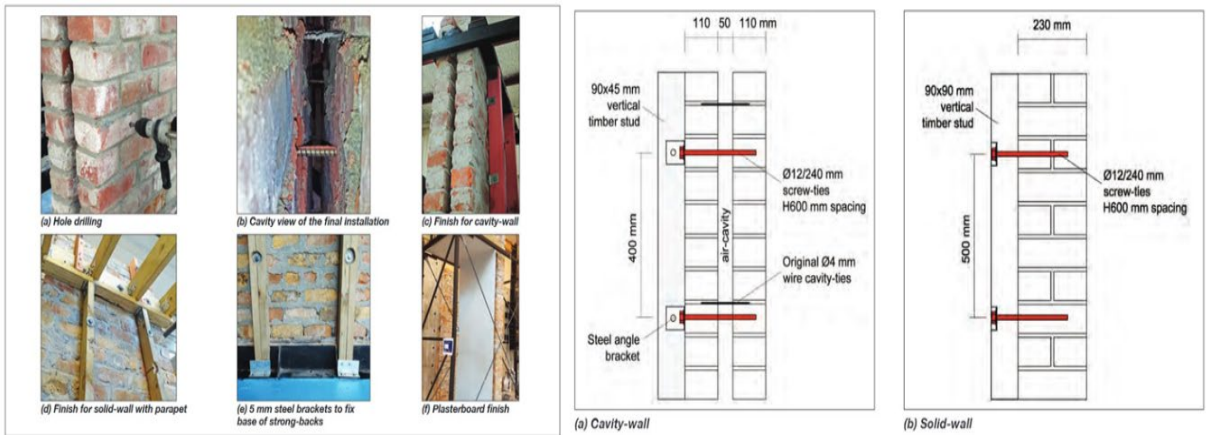

Seismic retrofit of masonry walls using timber strong-backs (2017)

(c)

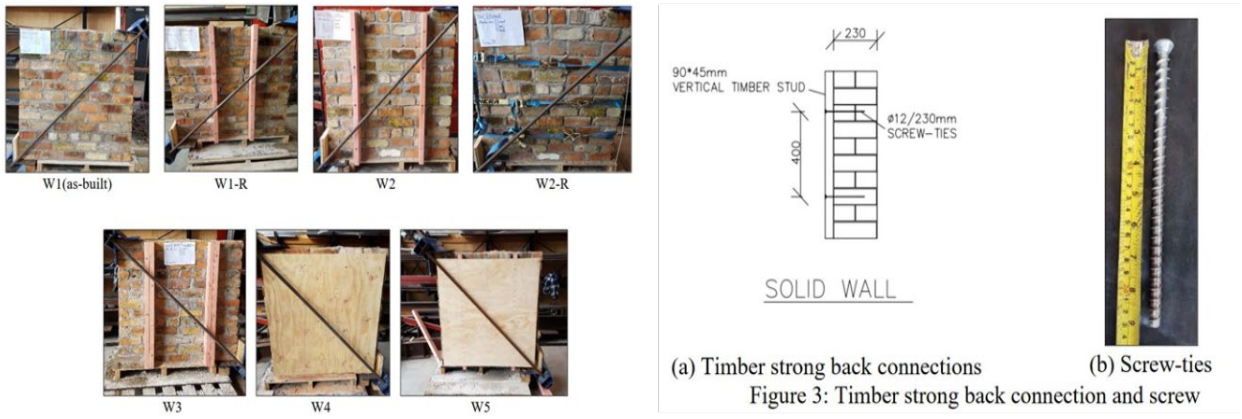

In-plane testing of URM wall panels retrofitted using timber strong-backs (2019)

(d)

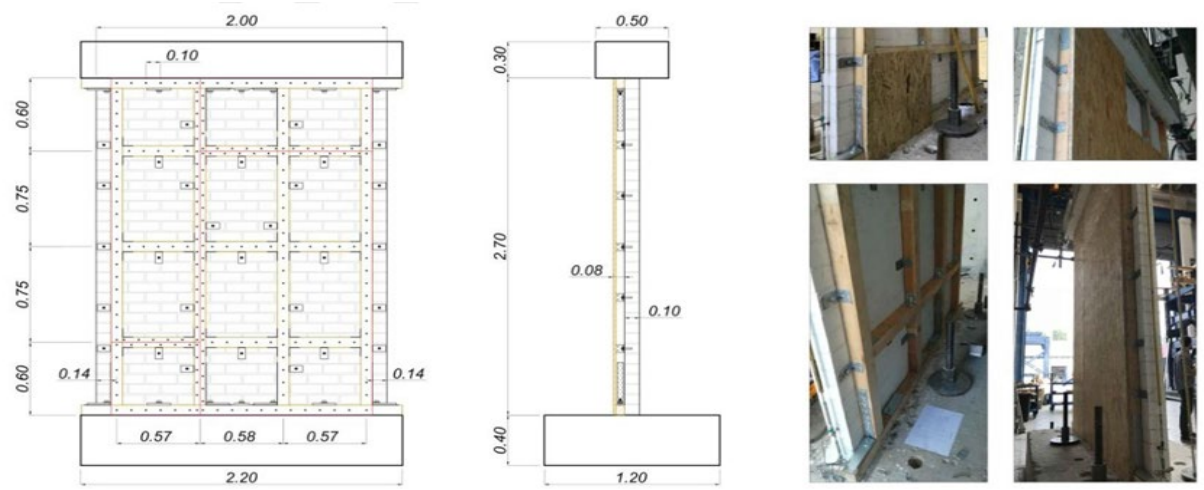

Cyclic response of masonry piers retrofitted with timber frames and boards (2021)

(e)

On-site testing of masonry shear walls strengthened with timber panels (2021)

(i)

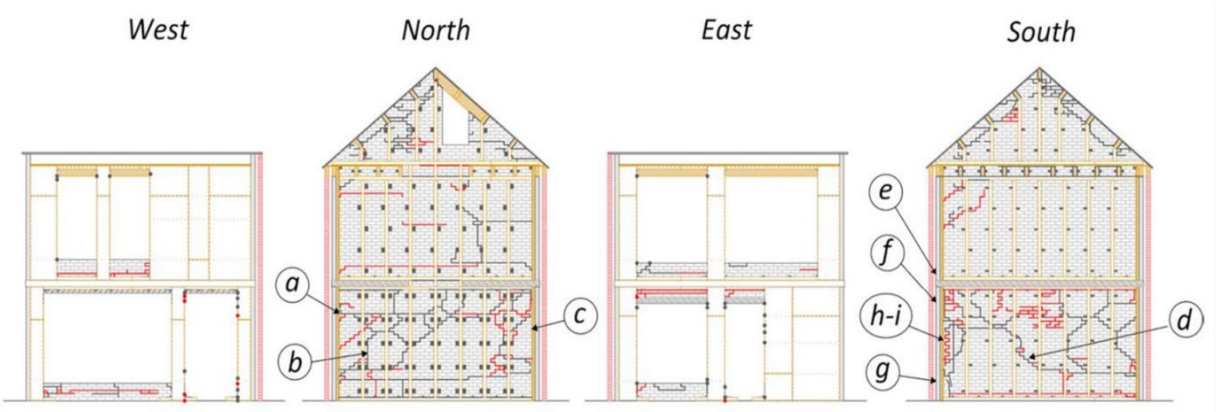

Full-scale shake-table tests on two unreinforced masonry cavity-wall buildings: Effect of an innovative timber retrofit (2021)

(j)

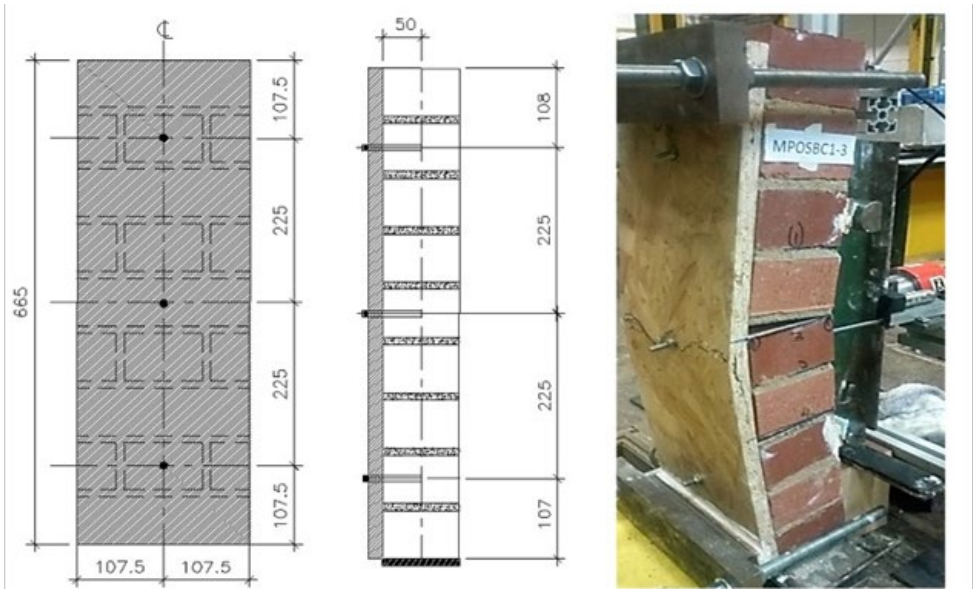

Retrofitting masonry walls against out-of-plane loading with timber based panels (2021)

(k)

Figure 1.2. Strengthening methods using timber. (a) Study [27]; (b) Study [20]; (c) Study [16]; (d) Study [28]; (e) Study [15]; (i) Study [18]; (j) [17]; Study [19].

For masonry construction refurbishment [27], the existing masonry building was covered by cross-laminated timber (CLT). The application of facadism method indicated to intervene on masonry construction and save the heritage masonry buildings [27]. Cross laminated timber (CLT) panels were used to strengthen the unreinforced masonry wall and the strap is attached to the URM wall with a chemical anchored steel rod [20]. The strength increases by 40%, and the ductility improves by 100% under high vertical load. Masonry piers were retrofitted with timber frames and boards under cyclic response [15], and the timber frame connected mechanical steel fasteners to masonry wall and boards were nailed to the frame. The lateral strength due to its high flexibility could increase by 35% and the ultimate displacement rising by 167% [15]. The diagonal compression tests were carried out the unreinforced masonry wall panels retrofitted using timber strong-backs and plywood overlays [28], and 8 mm diameter screw-ties were screwed into the masonry wall. The result of experiment shows a high ductile behavior, the screw-tie connections have a high buckling

resistance [28]. Timber strong-back was used to prevent out-of-plane failure of masonry walls for seismic retrofit [16] and strong back is simple and cost-effective retrofit solution. The mechanical screw-ties were the connection between timber and masonry wall, and the experimental result illustrates a significant reduction displacement and an increased the peak ground acceleration of three times than the unreinforced masonry wall [16]. On-site testing of masonry shear walls strengthened with timber panels (CLT-cross laminated timber and LVL-laminated veneer lumber) [18] was carried out on three clay-brick walls under in-plane semi-cyclic quasi-static loading, and the connection between timber and masonry was used to screw fasteners and steel bracket was fixed to prevent panel uplift. The outcome of the experiment presents the in-plane shear force of damaged specimen increases by 20% and 40% for the undamaged masonry wall, and drift levels of both specimens was up to 2% [18]. An innovative timber retrofit solution was implemented on the unreinforced masonry cavity-wall buildings under full-scale shake-table tests [17]. The timber retrofitting solution improves both the in-plane and out-of-plane capacities of the buildings, and for near-collapse conditions, a peak ground acceleration increases from 0.39g to 0.78g [17]. The retrofitting technique against out-of-plane loading for masonry wall emphasizes oriented strand boards (OSB) panels, and chemical and mechanical connections [19]. The flexural strength of the strengthened wall using chemical anchor was 7 times greater than the unreinforced masonry wall and for employing mechanical anchor was 5 times higher than the plain wall [19]. The study of timber based integrated techniques [29] investigates to improve energy efficiency and seismic behavior of existing masonry buildings. The numerical result shows timber panel decreases thermal transmittance by 78% and the proposed solution improve stiffness and shear response of wall [29]. The advantage of

timber is a lightweight and easy-to-assemble material. The experimental result shows that the wooden material used in the strengthening method could increase strength by around 30 percent, and the displacement could improve by more than 100 percent. The screw and chemical anchors were used to connect brick and timber in the above studies.

Applying epoxy resin in the retrofitting method improves the strength of the connection. Most of the studies have investigated using the screw rather than bolt securing to the masonry wall. There are few studies where epoxy resin has been used to connect the timber and bolt when the epoxy resin bonds the bolt in the masonry wall. Our study evaluated the strength performance of the joint brick and wood and proposed the calculating method of their performance.

The results of the above reinforced masonry studies emphasized the use of timber material to increase the strength and deformation of an unreinforced masonry wall. The use of lightweight materials has the additional advantage of reducing the weight of the strengthened structure. This study emphasizes the in-plane shear behavior of the strengthening solution for the unreinforced brick masonry wall using the SPF (spruce, pine, and fir) frame and plywood panel. As advantage of our retrofitting technique is compared with other research, it is cost-effective and lightweight material, easy assembling, and masonry-to-timber connection has high stiffness. The effective connection which is an M12 bolt with a chemical anchor [30] was selected in this study. The aim of this study is to investigate the reinforced effect on brick walls using timber walls and the experimental study and prediction method to determine the initial stiffness and ultimate load for unreinforced brick walls and reinforced brick walls. The benefit of this study is the usage of local material, light members, and estimation of reinforced masonry using a simple formula.

1.3.Objectives

The aim of this study is to investigate reinforced effect of brick wall with timber material. The strengthening material includes timber frame, plywood panel, bolt, and chemical adhesive. The main objectives of this study are:

- To define material properties of brick, cement mortar, brick-to-mortar interface element and small masonry specimen
- To determine joint strengths by experiment and prediction
- To investigate brick wall and reinforced brick wall experiment under cyclic lateral load
- To predict brick wall and reinforced brick wall with timber

1.4. Methods

In this research, experimental and prediction calculations were conducted and compared. Chapter II shows the material properties of brick, mortar, brick-to-mortar interface elements, and small masonry walls. All material properties were obtained by experiments followed under related standards. Chapter III presents strength properties of connection between brick and lumber material. Pullout and shear strength of connection were obtained by experiment and proposed prediction calculation. Chapter IV and Chapter V include the result of brick and reinfroced brick wall experiments and prediction estimation.

CHAPTER II.

MATERIAL PROPERTIES

2.1.Brick

2.1.1. Dimension, density, and absorption

The red clay brick was tested in this study. To define the material properties of the clay brick, ASTM C67/C67M-20 standard [31] was followed. The bricks used in the experiment were purchased from a Japanese building materials store. The width, length, height, and weight of the brick were measured by the 10 specimens in Table 2.1.

Table 2.9. Dimension, density, and absorption of brick

State	Brick size *(mm)*			Weight *(g)*	Volume *(cm^3)*	Density *(g/cm^3)*	Water absorption *(%)*
	Length *(l)*	Width *(b)*	Height *(h)*				
Mean	210.3	97.4	61.8	2381.3	1265.8	1.9	0.3
SD	1.9	1.2	1.0	17.6	35.2	0.05	0.04
CV,%	0.9	1.3	1.7	0.7	2.8	2.5	14.81

The water absorption in Figure 2.1 is considered to define durability including quality of brick, weathering, burning degree and pores in brick. Brick specimen was weighted and then submerged in the clean water at 15^0C for the 24 hours. Specimens were taken and wiped off the surface water with a cloth and then specimens were weighted. The cold-water absorption of brick in Table 2.1 is determined from equation (2.1).

$$Absorption, \% = 100 \cdot \left(\frac{W_s - W_d}{W_d}\right) \quad (2.1)$$

Where, W_d is dry weight of the specimen (g); W_s is saturated weight of the specimen after submersion in cold water.

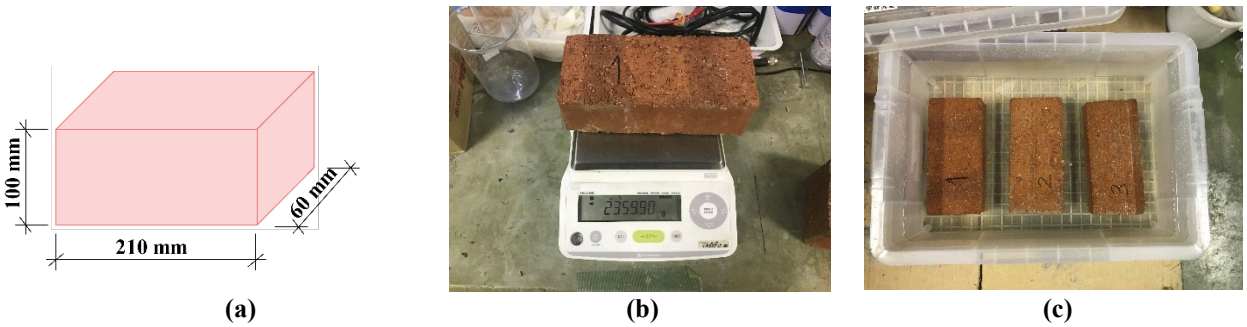

Figure 2.1. Brick. (a) Brick dimension; (b) Weight brick; (c) Brick in water.

2.1.2. Specimen and set-up of flexural and compression experiments

Figure 2.2a presents the schematic set-up of flexural test. The load on the specimen shall be adjusted at a continuous uniform speed 1mm/min.

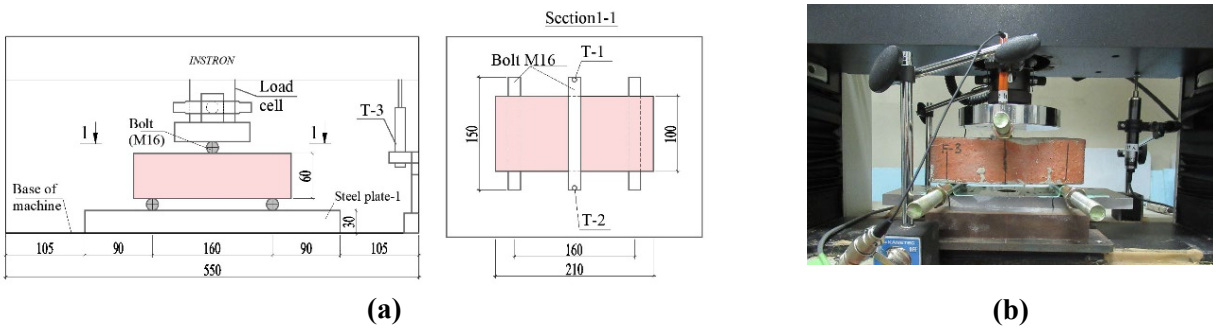

Figure 2.2. Set-up of flexural test. (a) Schematic set-up; (b) Photo of set-up.

The rupture of modulus in the specimen is determined by the equation (2.2).

$$S = 3W \cdot \left(\frac{l/2 - x}{b \cdot h^2}\right) \tag{2.2}$$

Where; S is modulus of rupture (N/mm^2); W is maximum load (N); l is distance between support (mm); b is width of specimen; d is height of specimen; x is average distance from the midspan of specimen (mm).

Figure 2.3 shows the experimental set-up of brick's compression test. The full-size brick shall be tested until it is broken. Two displacement transducers were used to measure the vertical displacement and it is placed front and backside of specimen.

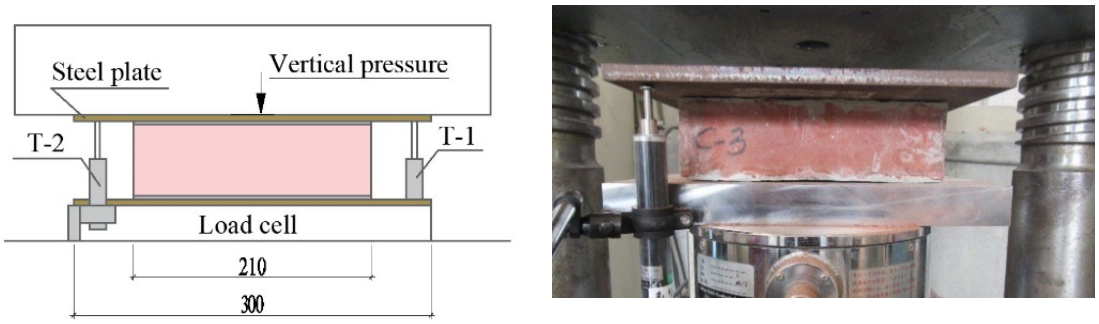

(c) **(d)**

Figure 2.3. Set-up of brick compression test. (a) Schematic set-up; (b) Set-up photo

The compressive strength of each specimen is determined by equation (2.3).

$$C = \frac{W}{A} \tag{2.3}$$

Where, C is compression strength (N/mm^2); W is maximum load (N); A is the gross sectional area (mm^2).

2.1.3. Result of flexural and compression experiment

To obtain material properties of the clay brick, 10 specimens for flexural test and 6 specimens for compression test were tested in this study. The mean flexural strength is 3.9 N/mm^2 and the mean compression strength is 31.4 N/mm^2 in Table 2.2. The mean elastic modulus of six specimens is 1201.9 N/mm^2 and it is determined from 5 to 30 percent of the maximum compression strength in Figure 2.4c.

Table 10.2. Material properties of brick

Properties	Flexural strength	Compression strength	Elastic modulus
Specimen number	10	6	6
Mean (N/mm^2)	3.9	31.4	1201.9
St.dev (N/mm^2)	1.1	3.6	298.8
CV, %	27.9	11.5	24.8

As can be seen from Figure 2.4b, the failure is complete when the load reaches its maximum value. It means that vertical cracks formed at the bottom edge of the brick when the load reaches its maximum value. The failure was over very quickly. Therefore, the displacements did not continue in the diagram of Figure 2.4a. Figure 2.4c illustrates the

compression stress and axial strain curve. Figure 2.4d is failure photo of the compression test and the tensile vertical crack appeared on the specimen. The crack distribution is evenly distributed over the brick area. During the test, the outer edge of the brick began to crumble. When the vertical load was complete, the brick core remained.

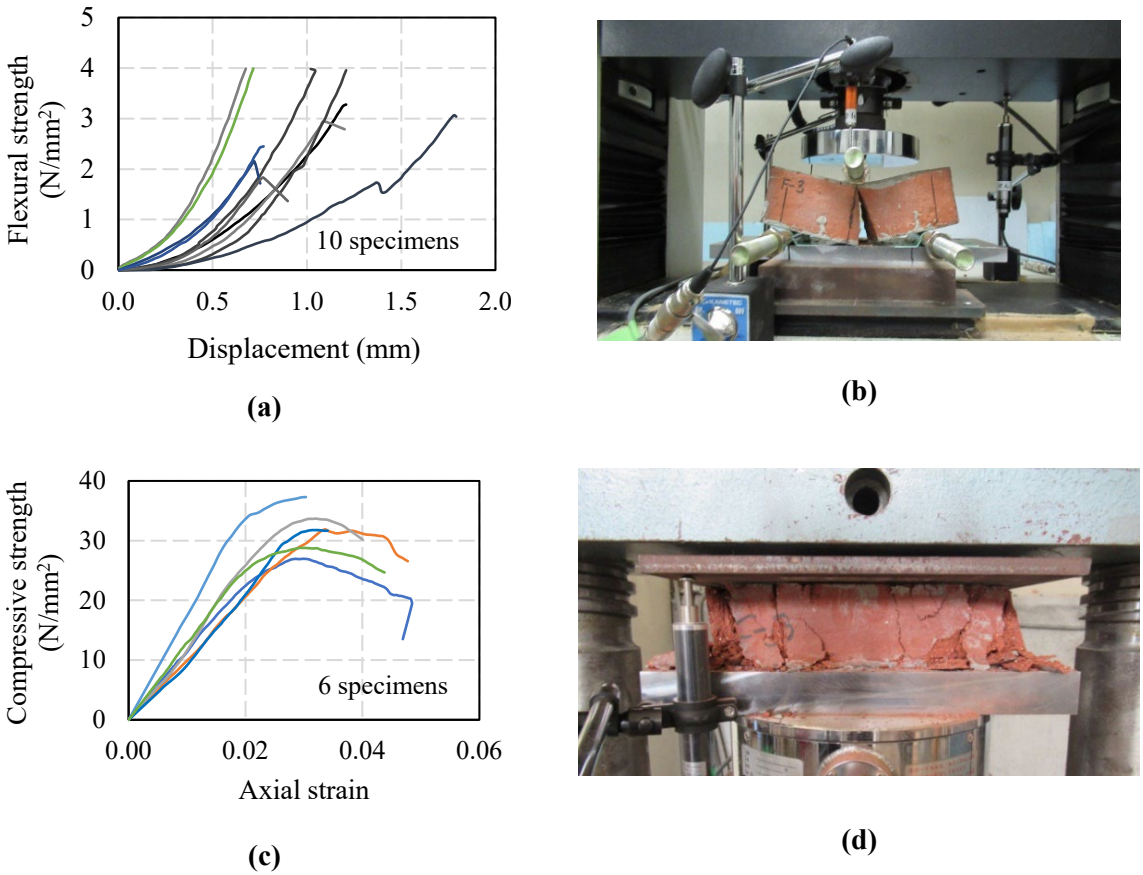

Figure 2.4. Result of flexural and compression test for brick. (a) Flexural strength-displacement curve; (b) Failure photo of flexural test; (c) Compression strength stain curve; (d) Failure photo of compression test.

2.2. Mortar

In this study, cement mortar is used in the experiment, and specimens were prepared in two different conditions. First, the prism mortar specimens were prepared under laboratory conditions and were tested after 28 days according to ASTM C349-18 [32] and ASTM C348-20 [33] standards. Second, cylinder mortar specimens were taken from the same mortar at the brick wall construction and were cured in similar conditions to brick wall. The uniaxial compressive test of cylinder specimens was carried out after preparing six months.

2.2.1. Preparation (mixing, casting) and set-up of mortar

Mixing ratio of cement and sand was 1:6. ASTM C128-01 [34] is followed to define the density of sand and cement. Density of Portland cement is 1.454 g/cm^3 and density of sand is 1.649 g/cm^3. Water cement ratio is 0.5. To prepare sand, the properly weighted sand was rinsed with water and then dust was removed, and sand was dried in Figure 2.5a. If mortar is not used at time, it is stored in container without losing the moisture of the sand in Figure 2.5b. Before preparing the mortar specimen, metal mold was pre-lubricated (oil) as shown in Figure 2.5b. Sand and cement are mixed with mechanical mixer in Figure 2.6a. After mixing well, water is added and stir well again. Mortar is added gradually in the oiled mold to prevent forming pores. Once mortar is well compacted, mortar is covered with plastic bag to retain moisture. The prepared mortar is stored in the mold for 2 days in Figure 2.6b, then remove it from the mold and immerse it in water at 65% humidity for 24 hours in Figure 2.6c. Then samples shall be kept at 20° C and 65% humidity for 21 days.

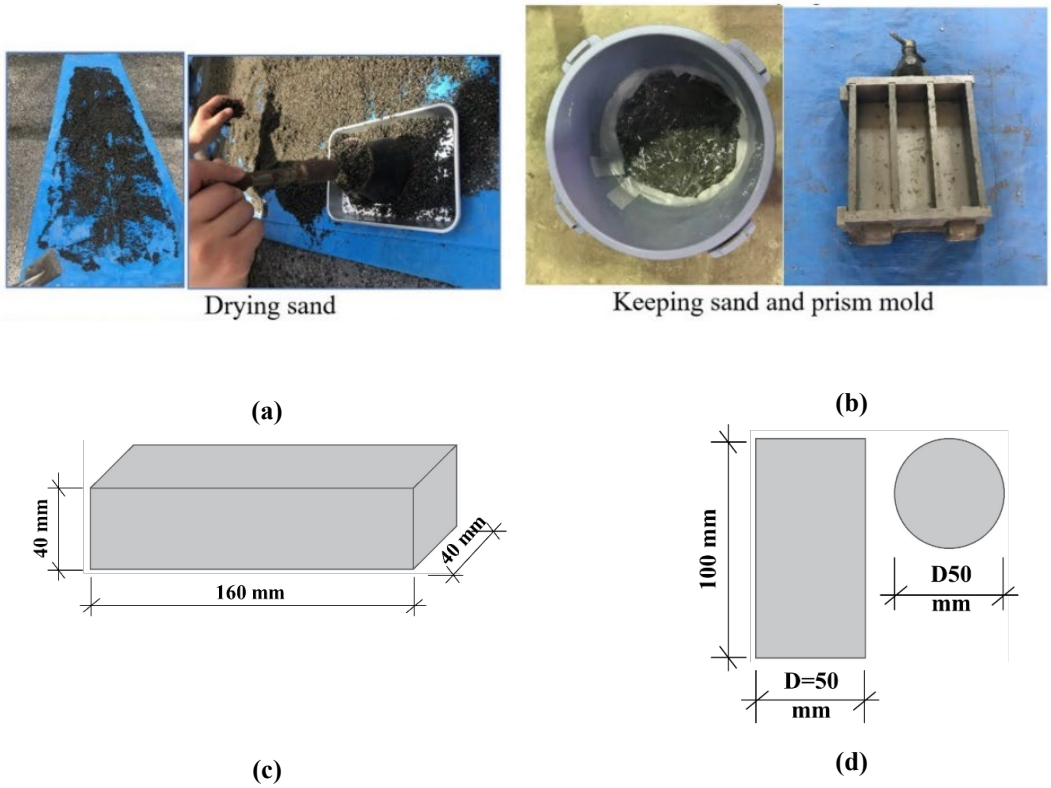

Figure 2.5. (a) Drying sand; (b) mold; (c) prism specimen; (d) cylinder specimen

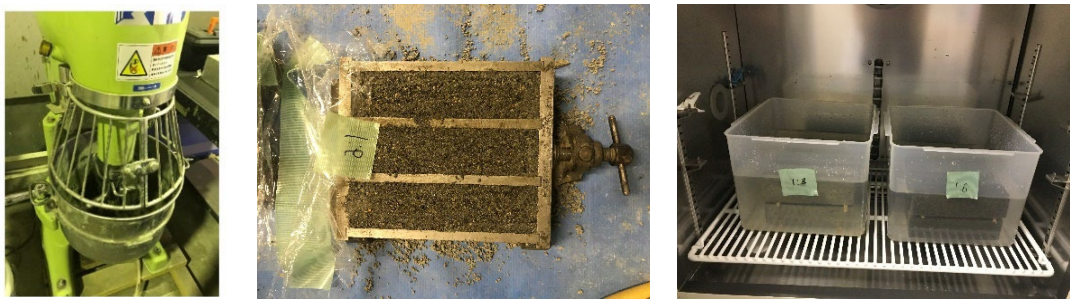

Figure 2.6. (a) Mechanical mixer; (b) Mortar specimen with mold; (c) Prism mortar in water

Figure 2.7 presents the experimental set-up of flexural and compression test of prism mortar. The support distance of flexural test is 130 mm. The compression load was applied uniformly until specimen is broken. Three specimens were tested to define the flexural strength. The flexural strength is calculated by equation (2.4).

$$S_f = 0.0028 \cdot P \tag{2.4}$$

Where, S_f is flexural strength (N/mm^2); P is maximum load (N).

The compression strength is calculated by the equation (2.5).

$$S_C = \frac{P}{A} \tag{2.5}$$

Where, P is maximum load (N); A is average cross-sectional area of top and bottom sides (mm^2).

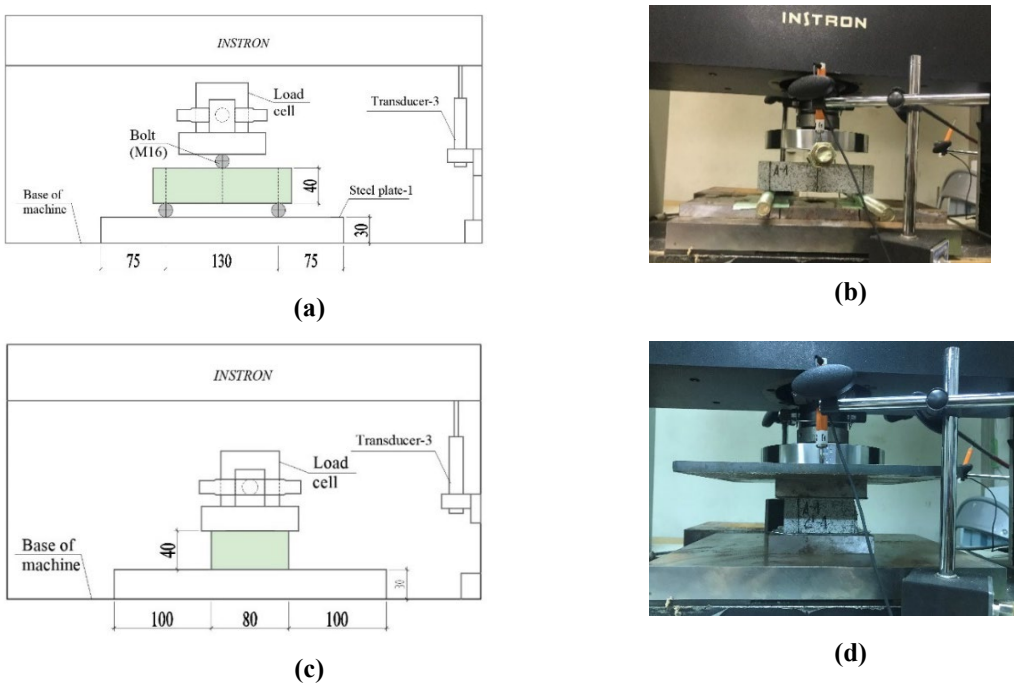

Figure 2.7. Flexural and compression test set-up of prism mortar. (a) Schematic set-up of flexural test; (b) Photo of flexural test; (c) Schematic set-up of compression test; (d) Photo of compression test.

2.2.2. Result of flexural and compression experiment for prism and cylinder mortar

To obtain the material properties of prism mortar, 3 specimens for flexural test and 5 specimens for compression test were tested in this study. The mean flexural strength is 2.5 N/mm^2 and the mean compression strength is 5.9 N/mm^2 in Table 2.3.

Table 2.11. Material properties of prism specimen (28 days)

Properties	Flexural strength	Compression strength
Specimen number	3	5
Mean (N/mm^2)	2.5	5.9
St.dev (N/mm^2)	0.2	0.5
CV, %	5.8	8.1

Mortar specimens were applied the vertical load when specimen is broken. Figure 2.8a illustrated the flexural strength and displacement curve of the prism mortar. As can be seen from Figure 2.8a, failure is complete when the load reaches its maximum value. It means that the vertical cracks formed at the bottom edge of the brick when the load reaches its maximum value in Figure 2.8b. Figure 2.8c illustrates the compression stress and displacement curve. Figure 2.8d is the failure photo of the compression test and the tensile vertical crack appeared on the specimen. The crack distribution is evenly distributed over the brick area.

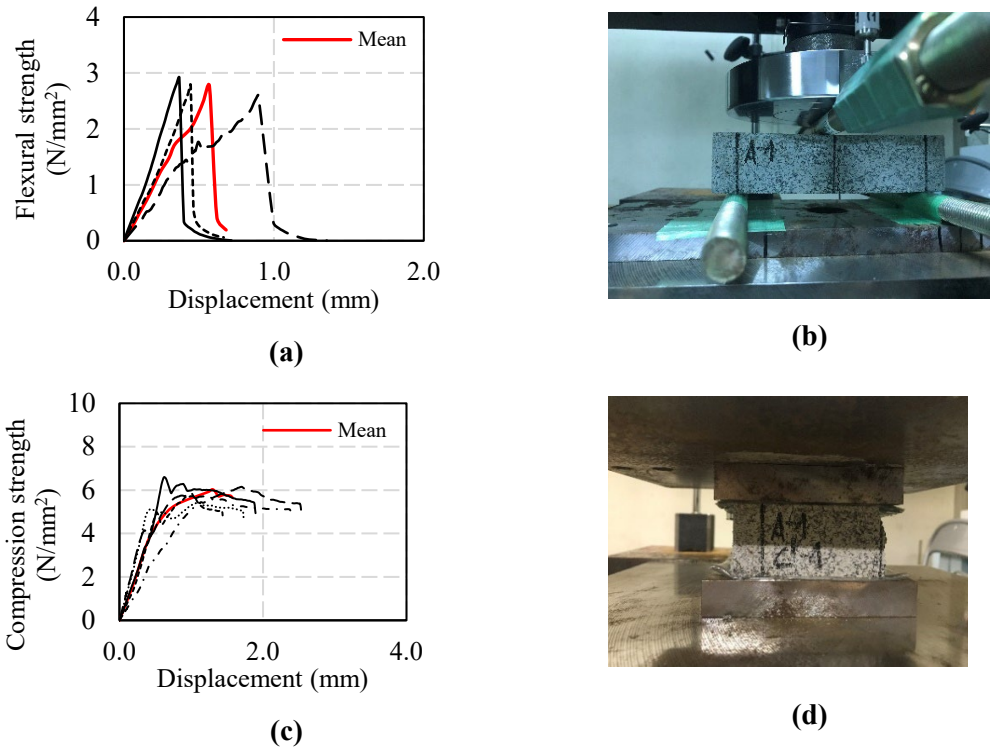

Figure 2.8. Result of flexural and compression test for mortar. (a) Flexural strength-displacement curve; (b) Failure photo of flexural test; (c) Compression strength and displacement curve; (d) Failure photo of compression test.

Second, cylinder mortar specimens were tested under the compression load. The uniaxial compression test of cylinder specimens was carried out after preparing six months. The compression strength is 10.9 N/mm^2 and variational coefficient is 11.9 percent. The elastic

modulus was defined by two different measurement such as transducer and strain gauge and the results are different in Table 2.4.

Table 2.12. Test result of cement mortar of cylinder specimen (6 months)

Properties	**Density** *(kg/m³)*	**Compressive strength** *(N/mm²)*	**Young's modulus** *(N/mm²)*	
			Transducer	Strain gauge
Specimen number	5	5	5	5
Mean value	1926.9	10.9	3225.8	8952.4
SD	35.0	1.3	657.7	2037.5
CV, %	1.92	11.9	20.4	22.8

Figure 2.9 shows the experimental photo and result of the cylinder cement mortar. The four displacement measurements were used in this experiment shown in Figure 2.9a. The displacement measurements were placed in the corners of top steel plate on the cylinder specimen. Failure of cylinder specimen is in the vertical direction on the specimen.

(a) **(b)** **(c)**

Figure 2.9. Compression test of cylinder cement mortar. (a) Photo of set-up. (b) Failure photo of cylinder specimen; (c) Compression strength displacement curve.

The 28 day's compression strength of prism mortar specimen increased almost two times lower than the 6-months compressive strength.

2.3. Shear properties of small masonry specimen

2.3.1. Specimen preparation and set-up

The brick mortar shear specimen consists of three bricks and two-layer mortar. Mortar thickness is 10 mm, and dimension of specimen is 210 mm x 200 mm x 100 mm. Cement

sand ratio of mortar is 1:6. EN 1052-3:2002 [35] was followed to determine the frictional coefficient and adhesion strength. In that case, the pre-compression shear test was carried out. Specimen construction and curing condition were followed by ASTM C1314-18 [36], and the polyethylene plastic sheet was covered on the specimen after preparation.

The experimental set-up for the pre-compression shear test is highlighted in Figure 2.10. In this study, there are three different pre-compression stress such as 0.2 N/mm^2, 0.6 N/mm^2, and 0.8 N/mm^2. As for the EN 1052-3:2002 [35] standard, the maximum pre-compression stress is 1 N/mm^2. When the pre-compression stress was assumed by 1 N/mm^2, the load cell capacity (50kN) of the universal testing machine was not enough in our case. Therefore, we reduced the pre-compression stress until 0.8 N/mm^2. As shown in Figure 2.10, the shear specimen is clamped by two C channel beams. The four M12 bolts were tightened on both sides of the shear specimen to create the pre-compression stress.

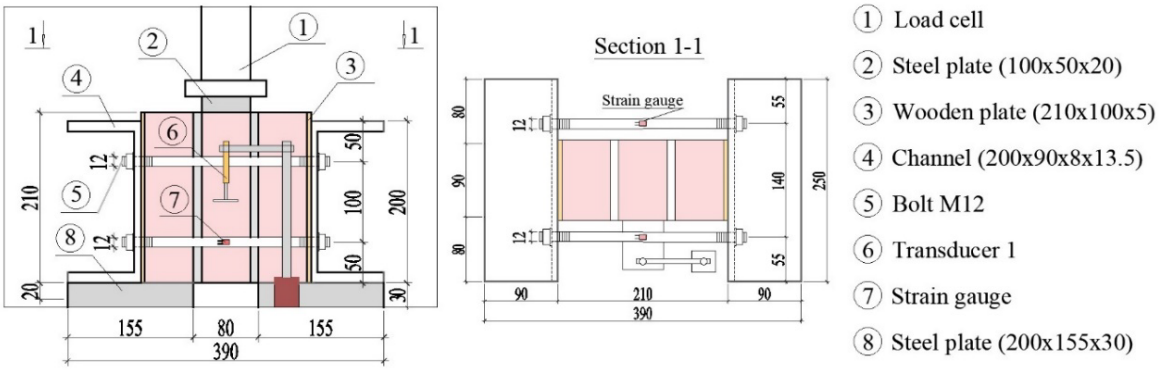

Figure 2.10. Experimental set-up of brick-mortar shear specimen.

Shear strength is defined by equation (2.6):

$$\tau = \frac{F}{2 \cdot A} \tag{2.6}$$

Where, τ is shear strength (N/mm^2); F is vertical load (N); A is cross-sectional area of interface element (mm^2).

2.3.2. Preparation of the pre-compression stress

Before assembling the shear specimen, the elastic modulus of bolt was defined by tensile test. The top and bottom side of bolt is fixed to the base of machine and metal jig. Two strain gauges are attached in the middle of bolt. Then specimen shown in Figure 2.11 is tested by tensile test in elastic region not until failure. The load is presumed by 10 kN. Four bolt's elastic modulus was determined in this study. The mean elastic modulus is 208343.8 N/mm^2 and the coefficient of variation is 1.9 percent.

When bolts were tightened by the wrench, the data logger could present the strain value. As the desired strain value indicated on the data logger, the tightening process was stopped for each pre-compression stress. To measure the pre-load on each bolt, the expected strain value is defined by equation (2.7).

$$\varepsilon_1 = \frac{P}{A \cdot E} \tag{2.7}$$

Where, P is the axial load (N), A is cross-sectional area of M12 bolt (mm^2), E is elastic modulus (N/mm^2).

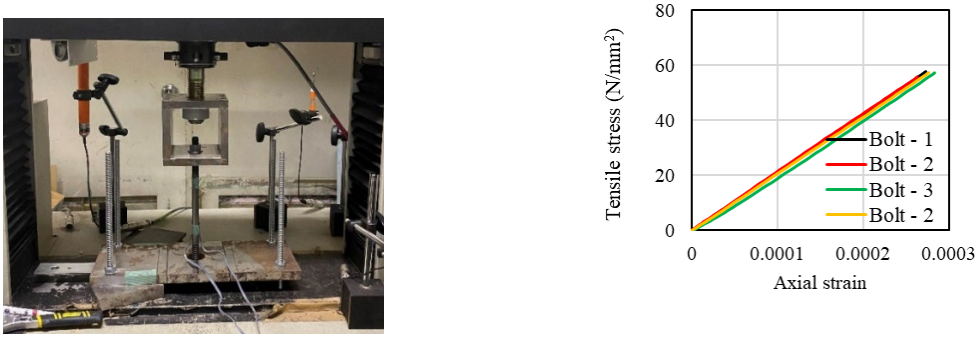

(a) **(b)**

Figure 2.11. Tensile test set-up for bolt. (a) Set-up photo; (b) Tensile stress-axial strain curve.

We can obtain the axial load on each bolt and each pre-compression stress. The axial load is 1050 N on the one bolt for 0.2 N/mm^2 pre-compression stress, 3150 N for the 0.6 N/mm^2 pre-compression stress, and 4250 N for the 0.8 N/mm^2 pre-compression stress, respectively.

The expected strain for each load and bolt is shown in Table 2.5. As indicated 'E' in Table 2.5, it was obtained from the tensile test on M12 bolt.

Table 2.13. Expected axial strain on each M12 bolt

Bolt	***E***	***A***	**Axial strain (10^{-6})**		
M12	(N/mm^2)	(mm^2)	0.2 N/mm^2	0.6 N/mm^2	0.8 N/mm^2
1	211755	113.1	43.8	131.5	177.5
2	211476	113.1	43.9	131.7	177.7
3	203468	113.1	45.6	136.8	184.7
4	206676	113.1	44.9	134.7	181.8

The experimental pre-compression load is calculated from equation (2.7) and result is shown in Table 2.6. We can obtain the expected pre-stress by the strain gauge measurement.

Table 2.14. Experimental result of the pre-load and pre-stress value

Expected pre-stress (N/mm^2)	**0.2**	**0.6**	**0.8**
Test (N/mm^2)	0.21	0.60	0.81
SD (N/mm^2)	0.02	0.01	0.01
CV, %	7.1	1.4	1.4

After adjusting the pre-compression stress on the shear specimen, the uniform vertical load was applied to the shear specimen until failure.

2.3.3. Result of brick-mortar interface shear test

Figure 2.12 presents the experimental result of the brick-mortar interface shear test. Figure 2.12a shows the relation between shear strength and displacement for the 0.2 N/mm^2 pre-compression stress. The mean maximum shear strength is 0.2 N/mm^2 and variational coefficient is 9 percent for the three specimens in Table 2.7. The initial stiffness of three specimens for 0.2 N/mm^2 pre-compression stress is close to each other, and shear modulus is 63.7 N/mm^2 and variational coefficient is 24.2 percent in Figure 2.12a. The experimental result of the 0.2 N/mm^2 pre-compression gave a good result.

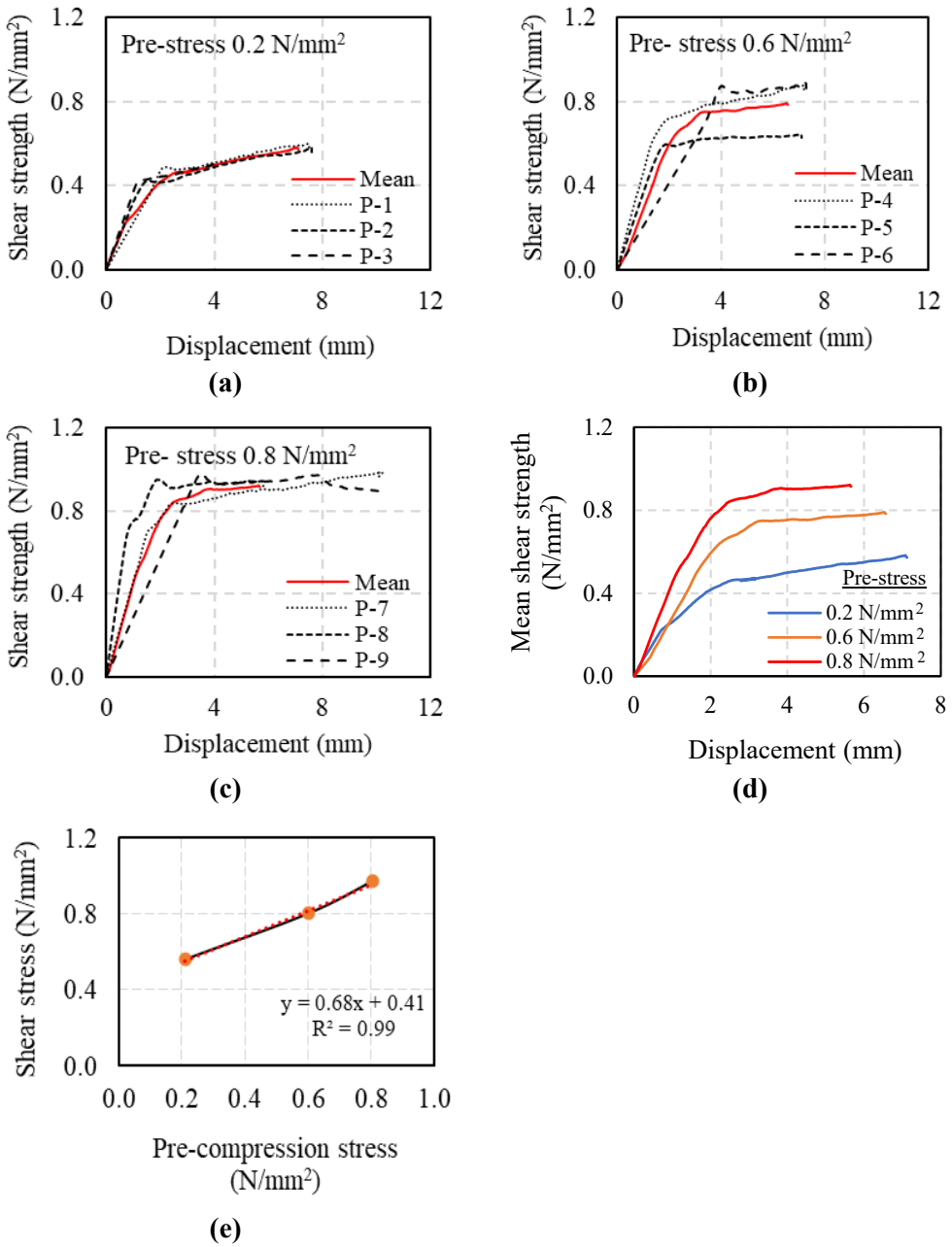

Figure 2.12. Result of shear test. (a) Pre-compression stress 0.2 N/mm^2; (b) Pre-compression stress 0.6 N/mm^2; (c) Pre-compression stress 0.8 N/mm^2; (d) Comparison result; (e) Relation between shear and pre-compression stress.

Figure 2.12b illustrates the shear stress and displacement curve of the 0.6 N/mm^2 pre-compression stress. The mean maximum shear strength is 0.8 N/mm^2 and variational coefficient is 17.3 percent in Table 2.7. The mean shear modulus is 72.4 N/mm^2 and variational coefficient is 38 percent for the 0.6 N/mm^2 pre-compression stress. In that case,

the maximum shear strength shows a reasonable result, but the initial slope is slightly different. Figure 2.12c shows the shear strength and displacement curve of the 0.8 N/mm^2 pre-compression stress. The mean maximum shear strength is 1 N/mm^2 for the 0.8 N/mm^2 pre-compression stress and variational coefficient is 2 percent in Table 2.7. The shear modulus is 115.3 N/mm^2 but variational coefficient shows high value 58.6 percent. Figure 2.12e presents the relation between shear stress and pre-compression stress. We can obtain the frictional coefficient and initial shear stress from Figure 2.12e. In that case, the frictional coefficient is 0.68 and the initial shear stress is the 0.41 N/mm^2. As shown in the above shear stress and displacement curve, the mean maximum shear stress can present a good result. But the initial stiffness is slightly different. Figure 2.12d highlights the comparison between three different pre-compression shear stress. As seen from the Figure 2.12d, the shear stress depends on the pre-compression stress. The pre-compression stress increases while the shear stress increases.

Table 2.15. Experimental result of brick-mortar interface shear test

Pre-compression stress (*N/mm^2*)	**0.2**		**0.6**		**0.8**	
Test result (*N/mm^2*)	Shear stress	Shear modulus	Shear stress	Shear modulus	Shear stress	Shear modulus
	0.6	63.7	0.8	72.4	1.0	115.3
SD (*N/mm^2*)	0.05	15.4	0.14	27.8	0.02	67.6
CV, %	9.0	24.2	17.3	38.3	2.0	58.6

Figure 2.13 presents the failure mode of brick-mortar interface shear test for three different pre-compression stress. Failure mode of the 0.2 N/mm^2 pre-compression shear test is related to the sliding failure in Figure 2.13a. Sliding failure mode occurs interface between brick and mortar. There is no failure on brick and mortar. Figure 2.13b illustrates sliding failure mode of the 0.6 N/mm^2 pre-compression stress. The sliding failure happens between brick and mortar, but the small mortar of the upper side was broken during loading.

Figure 2.13c shows the failure mode of the 0.8 N/mm^2 pre-compression shear test. Failure mode is the sliding failure appeared in the three specimens. The specimen shown in Figure 2.13c failed the sliding failure and mortar was broken in the middle of specimen. As shown in Figure 2.13, the sliding failure occurred in all specimens and failure happens between brick and mortar. No failure was observed between brick and mortar at the 0.2 N/mm^2 pre-compression shear specimen. As the pre-compression stress increases, cracks in the mortar are observed in Figure 2.13b,c.

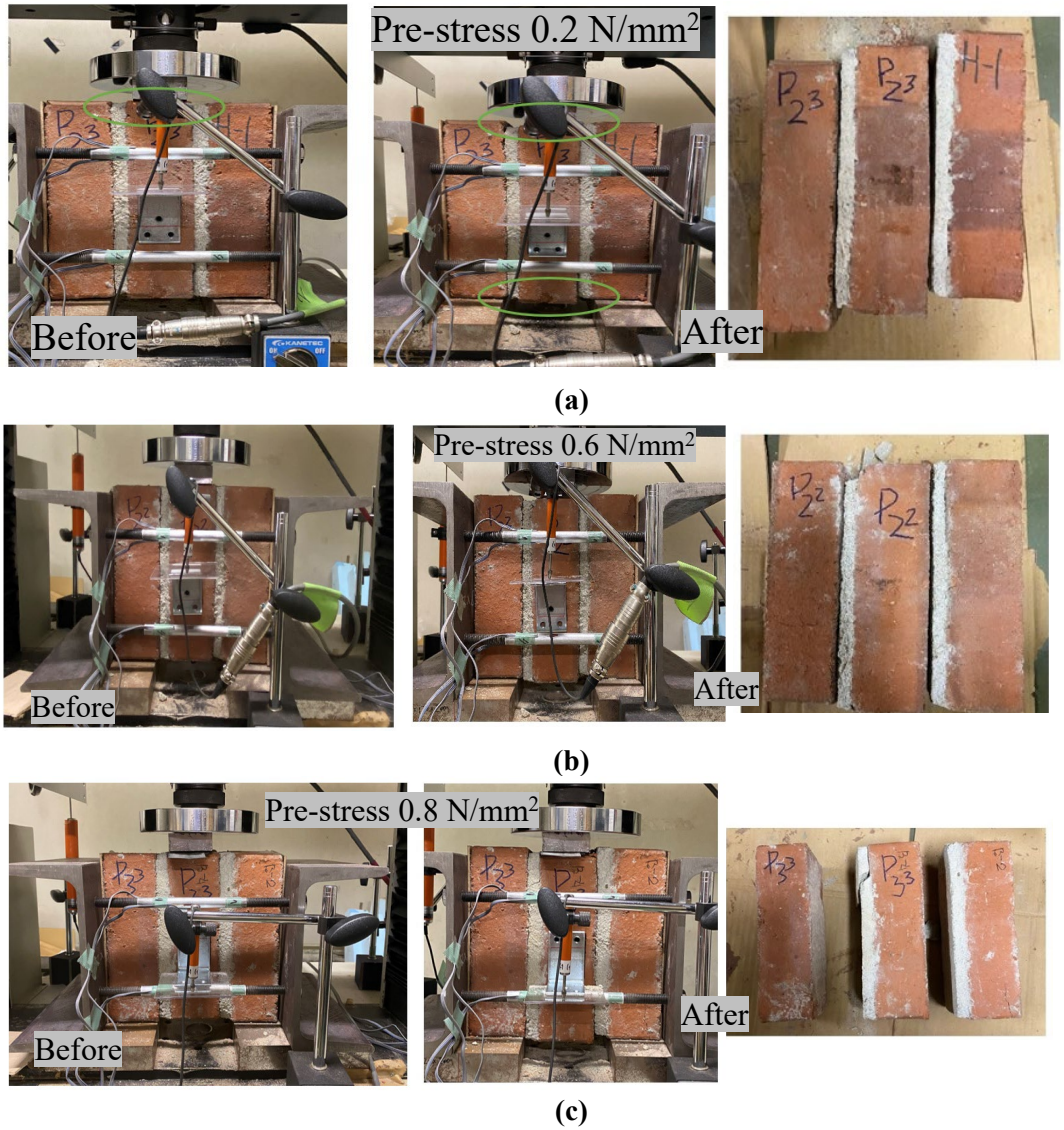

Figure 2.13. Failure of shear test. (a) Pre-compression stress 0.2 N/mm^2; (b) Pre-compression stress 0.6 N/mm^2; (c) Pre-compression stress 0.8 N/mm^2.

2.4. Small masonry compression experiment

2.4.1. Specimen and set-up

Masonry specimens were prepared and tested under the vertical compression load to determine the compression strength of masonry. ASTM C1314-18 [36] standard was followed in this study. Specimen size is 210 mm x 200 mm x 100 mm and height-to-thickness ratio is 2. Five masonry specimens were tested, and one specimen has three brick and two-layer mortars. After building each specimen, specimens were covered with a polyethylene plastic sheet and stored for 28 days. Before testing two days, a polyethylene plastic sheet was removed. Figure 2.14 shows the experimental set-up of the masonry compression test.

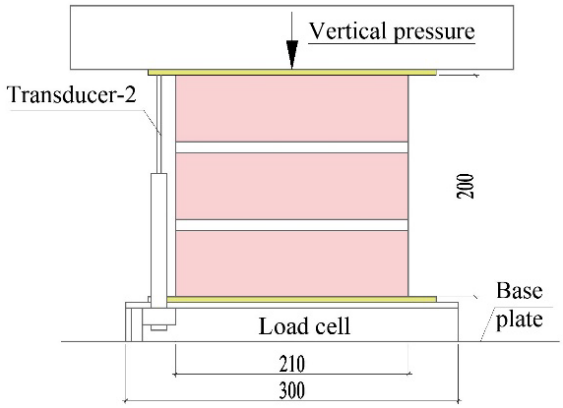

Figure 2.14. Experimental set-up of the masonry compression test.

The masonry compression strength is determined by equation (2.8):

$$\sigma = \frac{F}{A} \tag{2.8}$$

Where, σ is shear strength (N/mm^2); F is the vertical load (N); A is cross-sectional area (mm^2).

2.4.2. Experimental result

Figure 2.15a,b shows the failure of the uniaxial compressive test, and a tensile crack started to appear on the specimen when the compression load was approaching the maximum value. Figure 2.15c illustrates the compression stress-displacement diagram of the experiment of the masonry prism and 5 specimens were tested under the compression load. Two displacement measurements were placed under the prism specimen's the top steel plate to measure the vertical displacement. The elastic modulus was defined at 5 to 30 percent of the maximum compression load.

(a) **(b)** **(c)**

Figure 2.15. Brick masonry compression test. (a) Front and back view of failure; (b) Compressive stress-axial strain diagram of the uniaxial test.

Material properties of the masonry compression experiment are shown in Table 2.8. Ratio of shear modulus (G) and elastic modulus (E) in Table 2.8 can be defined by result of the pre-compression shear test and the masonry compression test. According to Eurocode 6 [37], the G/E ratio is relatively high value 0.4 compared with our experimental result. The study [10] defined the low G/E ratio by experiment and the G/E ratio is around 0.1 for 1 N/mm^2 the pre-compression stress.

Table 2.16. Result of prism masonry compression test

Compression strength	**Elastic modulus** *(N/mm²)*	**Pre-compression stress**	***G/E***	
			Test	EC-6
14.4 [28%]	1202.9 [31%]	0.2	0.05	0.4
		0.6	0.06	
		0.8	0.10	

2.5. Conclusions

In this chapter, the red clay brick, cement mortar, and small masonry specimens were tested and determined material properties. Material properties obtained from experiments can be used in the prediction of connection strength, unreinforced and reinforced brick walls.

Brick used in experiment has high quality, high burning degree, no weathering behavior, and low pores in bricks. The flexural strength of the mean 10 specimens is 3.9 N/mm^2. The compression strength of the mean six specimens is 31.4 N/mm^2. The elastic modulus of the mean 6 specimens is 1201.9 N/mm^2.

Cement mortar is conducted to determine flexural and compression strength. The flexural strength is 2.5 N/mm^2 and the compression strength is 5.9 N/mm^2 at 28^{th} day. The compression strength is 10.9 N/mm^2 and the elastic modulus is 3225 N/mm^2 after 6 months. The 28 day's compression strength of prism mortar specimen increased almost two times lower than the 6-months compressive strength.

Material properties of shear strength was defined by small masonry specimen. The pre-compression shear experiment was carried out in this section. Frictional coefficient is 0.68 and initial shear strength is 0.41 N/mm^2 by the pre-compression shear test. The pre-compression stress increased while the shear strength increased.

Small masonry specimen was tested in this section to determine the compression strength. The compression strength of the mean five specimens is 14.4 N/mm^2. G/E ratio is 0.05 for the 0.2 N/mm^2 pre-compression shear test, 0.06 for the 0.6 for the 0.6 N/mm^2 pre-compression shear test, and 0.1 for the 0.8 N/mm^2 pre-compression shear test.

CHAPTER III.

STRENGTH PROPERTIES OF CONNECTION BETWEEN BRICK AND SPF LUMBER

3.1. Introduction

One of the most important aspects of timber structures is connection. The bolt or screw fasteners were utilized to secure the unreinforced masonry wall to timber. There are two types of anchors, mechanical and chemical. The chemical anchor uses a threaded rod or reinforcing bar set in predrilled holes with adhesive compounds [21]. In a mechanical anchor system, forces on the heavily loaded anchor are generally transferred uniformly to the concrete along the length of the embedded portion of the anchor [22]. When estimating the strength of an anchor, two fundamental strengths act on the fastener. These include the pullout strength acting along with the bolt and the shear strength perpendicular to the bolt. The mechanical properties of metal anchors [23] were tested on historical stone masonry. The fastener types of metal, chemical, and mortar were inspected on tension and shear loads and compared with theoretical assumptions. The experimental result [23] concluded pullout strength of the chemical anchor showed more values than the other two. The experimental study [24] identified the shear strength of five types of screw anchors, including ø12 mm, ø12.5, and ø16.6 mm threaded diameters for connecting masonry structures to wood. Dry screw anchors [24] have been a possible solution for connecting masonry and wood

materials. It has been concluded that it may be better to use chemical adhesives for irregular stone masonry. The study [25] determined anchors' tensile and shear strength for limestone structures. Three different diameter bolts were tested with two bond agents (epoxy adhesive and cement-based grout) [25]. The tensile strength of the chemical anchor is greater than cement-based grout, and it was concluded that the shear strength showed similar values. An experimental study of pullout strength [26] was conducted on masonry walls, and the bolts were bonded with epoxy resin and were placed in the head and bed-joint and brick in the brick masonry wall. The test result [26] concluded that the bolt's pullout strength placed in the mortar was greater than the bricks'.

Timber may be beneficial to use as a simple strengthening approach to withstand seismic loads and increase the strength of the unreinforced masonry wall. Applying epoxy resin in the retrofitting method improves the strength of the connection. Most of the studies have investigated using the screw rather than bolt securing to the masonry wall. There are few studies where epoxy resin has been used to connect the timber and bolt when the epoxy resin bonds the bolt in the masonry wall. Various retrofitting methods have been proposed in the investigations. Our study considered that the strengthening method of the brick construction, which can be composed of wood, bolts, and adhesive, could be proposed as a simple method. This study evaluated the strength performance of the joint brick and wood and proposed the calculating method of their performance.

3.2. Material properties

Brick is the substrate material in this study. To predict the pullout strength and shear strength of composite material (brick-to-lumber) in the analytical estimation, the compressive strength of brick is one of the important parameters. Experimentation was used to determine the material properties of the brick. The applicable standard and recommendations are used to determine the mechanical qualities of SPF lumber, bolts, and epoxy resin. Material properties of brick is highlighted in chapter II.

3.2.1. SPF Lumber

An abbreviation of SPF is three species of spruce, pine, and fir. The size of SPF lumber used in this study is 2 × 4 (38 mm × 89 mm). The SPF lumber material is lightweight, has a clear appearance, has high strength, and has good working properties. The Standard for Structural Design of Timber Structures [38] was used to determine the material parameters of SPF lumber in visual grading class No.2. Table 3.1 lists the standard material properties.

Table 3.1. Standard material properties of SPF lumber

Material	Compressive Strength	Tensile Strength	Bending Strength	Shear Strength	Elastic Modulus	Bearing Strength
			(N/mm^2)			
SPF	17.4	11.4	21.6	1.8	9600	25.8

3.2.2. Bolt

The SS400 bolts (threaded steel rods), including M8, M10, and M12, were employed for the pullout and shear test. The ultimate tensile strength of the SS400 bolt is 400 N/mm^2, and the yield tensile strength is 240 N/mm^2. The yield strength in bending for the M10 and M12 bolts is assumed by 310 N/mm^2 and 413 N/mm^2 for the M8 bolt [39].

3.2.3. Epoxy resin

The chemical adhesive (epoxy resin) was adopted in this study to bond the brick to bolt and the wood to bolt. The chemical adhesive (HIT-RE 500 V3, Hilti, Inc., TX, US) performed better in shorter embedment depths, had the fastest curing time, and had a safer installation in the drilled holes. After injecting the epoxy into the drilled hole for the brick or wooden part, the curing period was 24h. Table 3.2 shows the chemical adhesive material parameters obtained from HILTI's product technical handbook [40].

Table 3.2. Material properties of chemical adhesive

Properties	Bond Strength (2 Days Curing)	Compressive Strength	Compressive Modulus	Tensile Strength (7 Days Curing)
		(N/mm^2)		
Adhesive	10.8	82.7	2600	49.3

3.3. Specimen and experimental set-up

3.3.1. Pull-out test

This study carried out experiments to define the pullout strength acting on the adhesive-bonded anchor. The pullout test was performed on 9 specimens with epoxy resin injected into the brick.

3.3.1.1 Specimen

Test specimen providing the pullout strength includes bricks, bolts, and epoxy resin. Three types of specimens with different bolt diameters, including M8, M10, and M12, were prepared for the pullout test. The bolt position and dimension are illustrated in Figure 3.1. A vibration drill bored a predrilled hole in the brick. The diameter of the hole was 2 mm larger than the bolt's diameter. The holes in the bricks were meticulously cleaned to improve the epoxy resin's adherence. The length of the bolt was 100 mm. The hole was filled to two-thirds with chemical adhesive, and the bolt was slowly poured into it. According to the

guideline of the epoxy resin [40], the requirement of hole diameter was 2 mm larger than the bolt's diameter, and the minimum depth for concrete was 60 mm in the M8 bolt [40]. In this test, the depth of the bolt was assumed by 50 mm based on the symmetry condition.

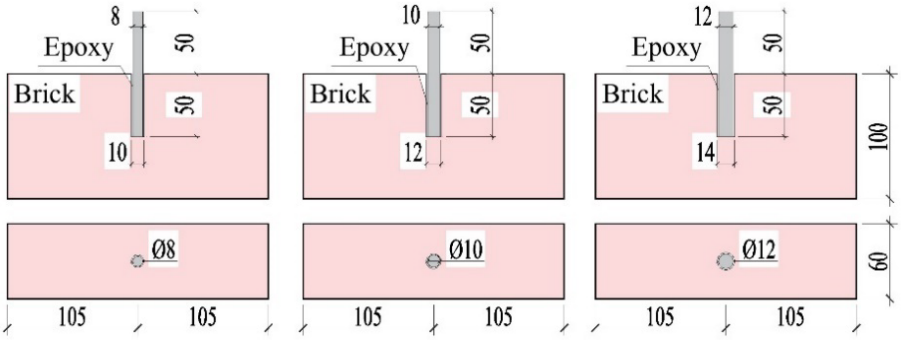

(a) **(b)** **(c)**

Figure 3.1. Bolt position and dimension on brick. (**a**) Specimen using M8 bolt; (**b**) Specimen using M10 bolt; (**c**) Specimen using M12 bolt.

3.3.1.2 Set-up

Figure 3.2 shows the setup used in the pullout experiment. The experiments were carried out on the universal testing machine (Instron 4204), and the setup follows ASTM E754–80 [41]. In this experiment, a jig was prepared by pulling the bolts upwards. The jig was square and was attached to the load cell at the top side. The specimen's bolt was linked to the bottom of the jig. The top and bottom connections inside the jig were tightened with a washer and nut. The steel plate is placed perpendicular to the brick part, as indicated in Figure 3.2. Four bolts secure the steel plate to the base of the test machine.

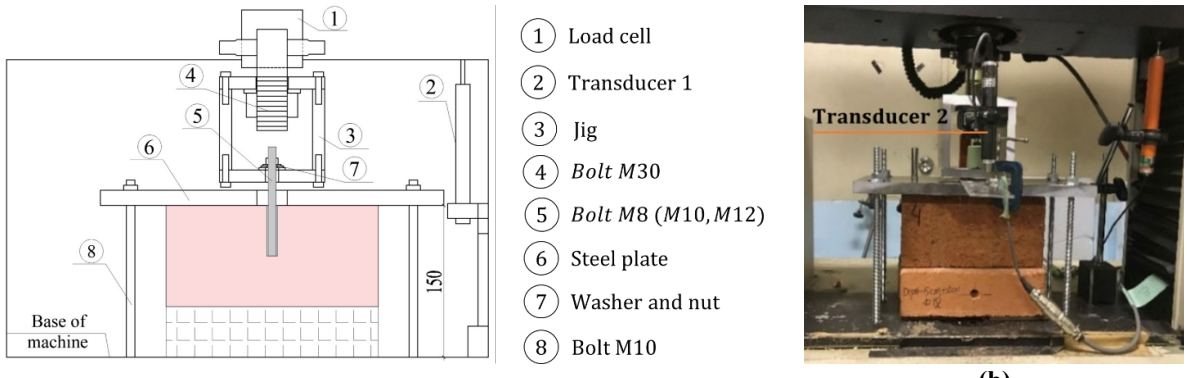

(a) **(b)**

Figure 3.2. Setup of pullout test. (**a**) Schematic setup; (**b**) Photo of setup.

The steel plate sustained the brick from moving upwards when the specimen was pulled up. The speed of the load was 2 mm/min. Monotonic loading was during the test, and the specimen was loaded until a failure. Three displacement gauges were used to measure the deformation. Transducer 1 was positioned in the cross-plane connecting the load cell. Figure 3.2b shows the placement of transducers 2 and 3 in front of and behind the specimen. The displacement was defined as the mean of the displacements measured by transducers 2 and 3 and is referred to as the relative displacement.

3.3.2. Dowel-Bearing test

The test that determines the dowel-bearing strength of wood is called the dowel-bearing test [42]. The reference value of the dowel-bearing strength of wood, metal, aluminum, and concrete is shown in NDS standard. In the case of composite materials (brick-to-lumber), the European Yield Theory (EYT) is often used to predict the shear strength of the bolted connection in the calculation of timber structures. European Yield Theory determines the failure mode and the minimum load causing damage. In the estimation of EYT, one of the most important parameters is the dowel-bearing strength of the main material (brick). The dowel-bearing strength of the main material should be three times the compressive strength of concrete or masonry, according to theoretical modeling in the NDS standard. The dowel-bearing strength of the brick material was defined experimentally in this study.

3.3.2.1 Specimen

According to the ASTM D5467 standard [42], which defines the dowel-bearing strength of a wooden structure, specimen preparation and test instruction was carried out in this study. The size of the brick specimen was 100 × 60 × 60. The specimen was initially drilled in the center of the brick as part of the preparation process. The hole was then sliced in half, and

the hole diameter was the same as the bolt diameter. To determine the bearing strength of brick, three types of bolts (M8, M10, and M12) were examined.

3.3.2.2 Set-up

Figure 3.3 shows the half-hole testing setup of the bearing strength of brick. During the experiment, the vertical load and displacement were measured. The specimen was placed on the steel plate, and then the uniform compressive load was applied to the bolt along the length. Transducer 1 measures the vertical displacement during loading. The load was conducted until a failure.

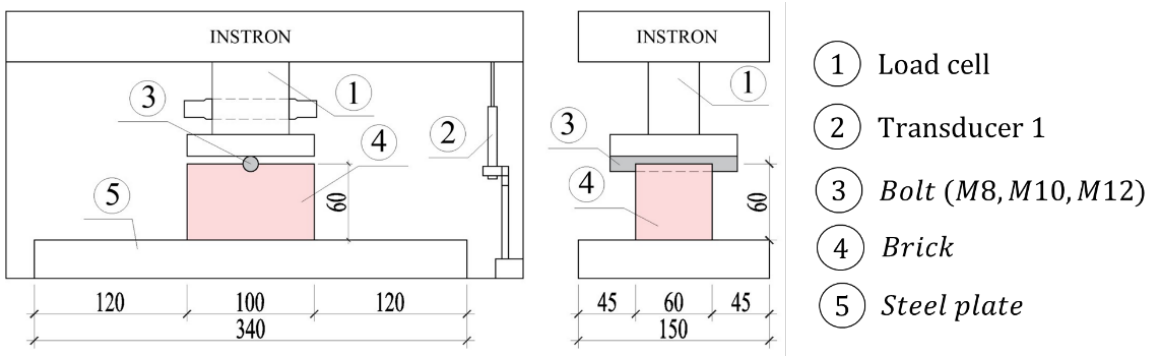

Figure 3.3. Schematic setup of dowel-bearing test.

3.3.3. Shear test

It is assumed that strengthening an unreinforced masonry structure with the wooden material will increase the shear strength of the masonry wall subjected to the horizontal load. The dowel fasteners are often bonded to the masonry wall with chemical adhesive. In addition, chemical adhesive was used to improve the adhesion of bolts and wood materials. Our study examined the difference between when the chemical adhesive is used and not used for the wood-to-bolt section when the chemical anchor is utilized in the masonry wall.

3.3.3.1 Specimen

We prepared two types of shear specimens (C-type and A-type) in Table 3.3. One is indexed by C-type, which is chemical epoxy not used in the lumber-to-bolt. The nut and

washer were used to tighten the end of the bolt on the lumber side. As for the A-type specimen, epoxy resin was utilized in the lumber-to-bolt. Both types of specimens have the same chemical anchor for the brick. Specimens for the shear test consist of brick, SPF lumber, bolt with nut and washer, and chemical adhesive. Two lumber material was placed on both sides of the brick. The brick sides indicate the “B” side and “A” side shown in Figure 3.4a. Because the bolt positions are varied, it is necessary to assemble brick and lumber material. The “A“ side of the brick was fastened to the “A“ side of the lumber, and the “B“ sides were the same. Three alternative bolt sizes (M8, M10, and M12) are included in both C-type and A-type specimens. Specimen name, the density of lumber material, bolt diameter, and the number of specimens is shown in Table 3.3.

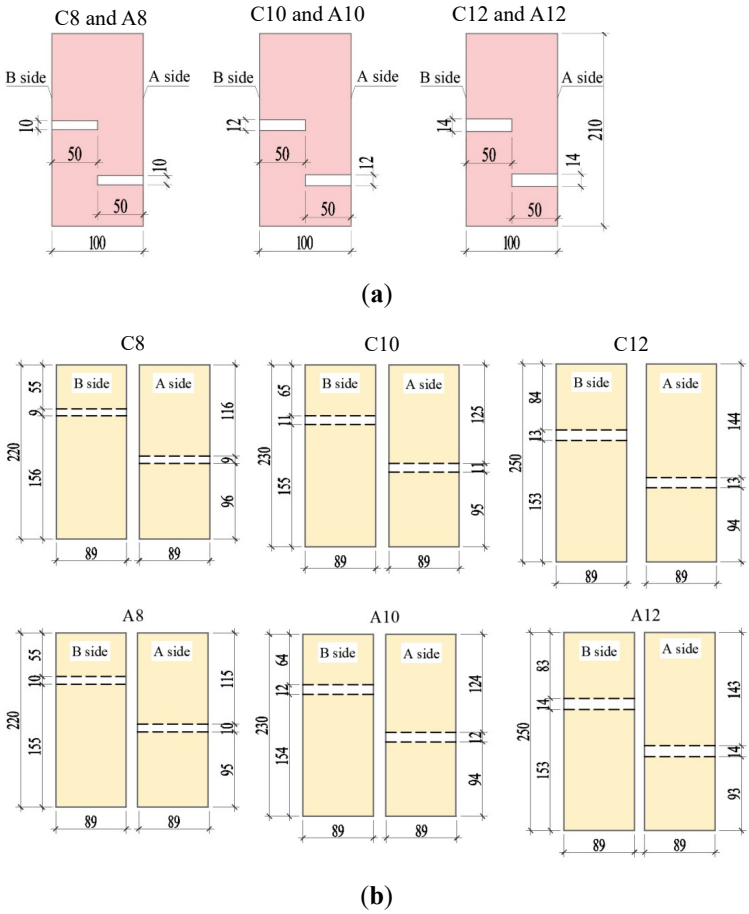

Figure 3.4. Dimension and bolt position. (**a**) Brick; (**b**) SPF lumber.

The 60 mm side of the brick was drilled with two holes for connecting bolts with chemical adhesive. The hole positions in the brick are indicated in Figure 3.4a. As for the brick, the nominal hole diameter was 2 mm larger than the bolt diameter, and the depth was 50 mm for both types of specimens. For the SPF lumber, the hole diameter was 1 mm larger than the bolt diameter for C-type specimens and 2 mm larger for A-type specimens. Figure 3.4b depicts the dimension and hole position in the SPF lumber. According to the Japanese standard for timber building, the minimum edge distance of a bolt hole in the lumber is seven times the diameter of the bolt (7d) [38]. The edge distance will prevent the lumber material from cracking before loading. The average density of lumber was 480 kg/m^3 in this experiment. The lumber length depends on bolt diameters, such as 220 mm, 230 mm, and 250 mm in the shear test. Two SPF lumber for one shear specimen has the same density. The width of lumber was 89 mm. The bolt was placed across the width of the lumber. The total length of the bolt was 200 mm. The necessary nuts and washers for M8, M10, and M12 were employed.

Table 3.3. List of specimens

Adhesive Using	**Name of Specimen**	**The Density of Lumber** *(kg/m^3)*	**Diameter of Bolt** *(mm)*	**Number of Specimens**
With epoxy resin	A8	467.2	8	3
	A10	509.2	10	3
	A12	494.8	12	3
Without epoxy resin	C8	469.2	8	3
	C10	474.4	10	3
	C12	480.8	12	3

The first step of the assembly process is that the epoxy resin was gradually poured into the “A” side or “B” side’s brick hole, and then the bolt was slowly inserted. After the bolt reached the bottom of the hole, the bolt was moved up and down several times. For the second step of the C-type specimen, the brick specimens with bolts were attached to lumbers using nuts and washers. For the A-type specimen, epoxy resin was poured into the hole of

the lumber, and then the brick specimen with bolt was attached with the lumber material instantly tightened by nuts and washers.

3.3.3.2 Set-up

The shear test setup shows in Figure 3.5, and the experiments were carried out on the universal testing machine (Instron 4204). The load cell capacity is 50 kN. During the test, the speed of load was 2 mm/min. Transducers 1 recorded the movement of the crosshead. Under the load cell, transducer 2 measured the down lift of the steel plate. To measure a relative displacement, transducers 3 and 4 were placed on the opposite side of the brick. To establish a flat surface before subjecting the load, nonshrink cement was applied to the top of the brick.

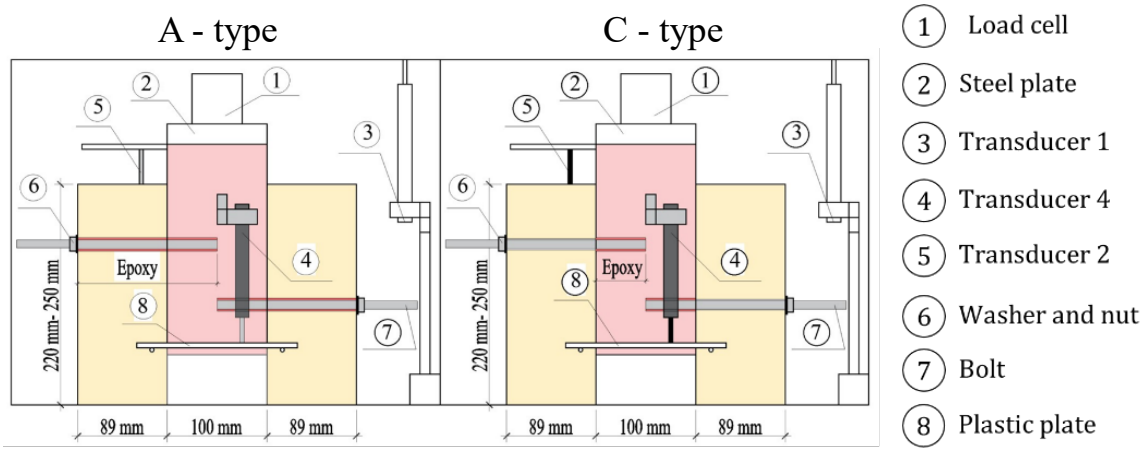

(a)

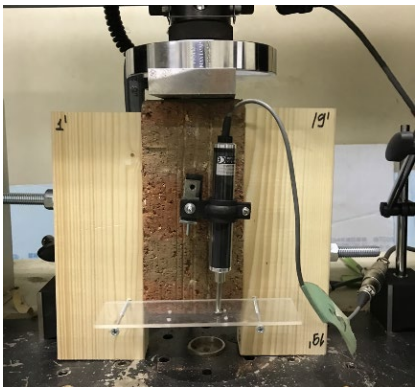

(b)

Figure 3.5. Specimen of shear test (**a**) Schematic setup; (**b**) Scene of the test setup.

3.4. Result of experiment

3.4.1. Pullout Performance

The result of the pullout test is illustrated in Table 3.4, and Figure 3.6 shows the experimental failures of three types of specimens. The chemical adhesive attaches completely to the bolt in each experiment shown in Figure 3.6. Table 3.4's coefficient of variation is indicated by the value in brackets.

Table 3.4. The result of pullout experiment

Specimen №	**The number of Specimens**	**Bolt Diameter** *(mm)*	**The Max. Pullout Strength** *(kN)*	**Displacement at Max. Load** *(mm)*	**Stiffness** *(kN/mm)*
P-8	3	8	8.8 (29.7)	0.9 (22.9)	15.7 (32.7)
P-10	3	10	9.5 (37.5)	0.7 (37.4)	26.6 (14.1)
P-12	3	12	12.1 (42.7)	0.4 (39.2)	46.1 (34.6)

(**a**) (**b**) (**c**)

Figure 3.6. Pullout failure on bricks. (**a**) P-8-1 specimen; (**b**) P-10-1 specimen; (**c**) P-12-3 specimen.

Figure 3.7 illustrates the load-displacement diagram of the pullout test, including the 5th percentile value in the graphs. The load-displacement diagrams in Figure 3.7 show that the load goes linearly to reach its maximum load and then decreases. Failure modes in Figure 3.6 illustrate the state of the combined cone–bond failure mode until the pullout load approaches its maximum value during the test. In addition, the microcracks created around the bolt on the top of the brick can be seen in Figure 3.6. Then the bricks specimens were split into two parts as the failure extended rapidly to the short side of the upper edge when the maximum load decreased. As shown in Figure 3.7d, the mean maximum pullout strength

increases with rising bolt diameter. As seen in Table 3.4, the displacement at maximum load progresses with declining bolt diameter. Figure 3.7d shows the highest pullout strength for the brick specimen with the M12 bolt specimen. The maximum stiffness likewise indicates the brick with an M12 bolt in Table 3.4. The maximum load of the M8 bolt specimen is 8% lower than that of the M10 bolt specimen and 37.5 percent lower than that of the M12 bolt specimen. The maximum pullout strength of M10 is 27.6% lower than M12 specimens. The stiffness of M12 is the highest result, and it is 2.9 times higher than the M8 specimen and 1.7 times for M10.

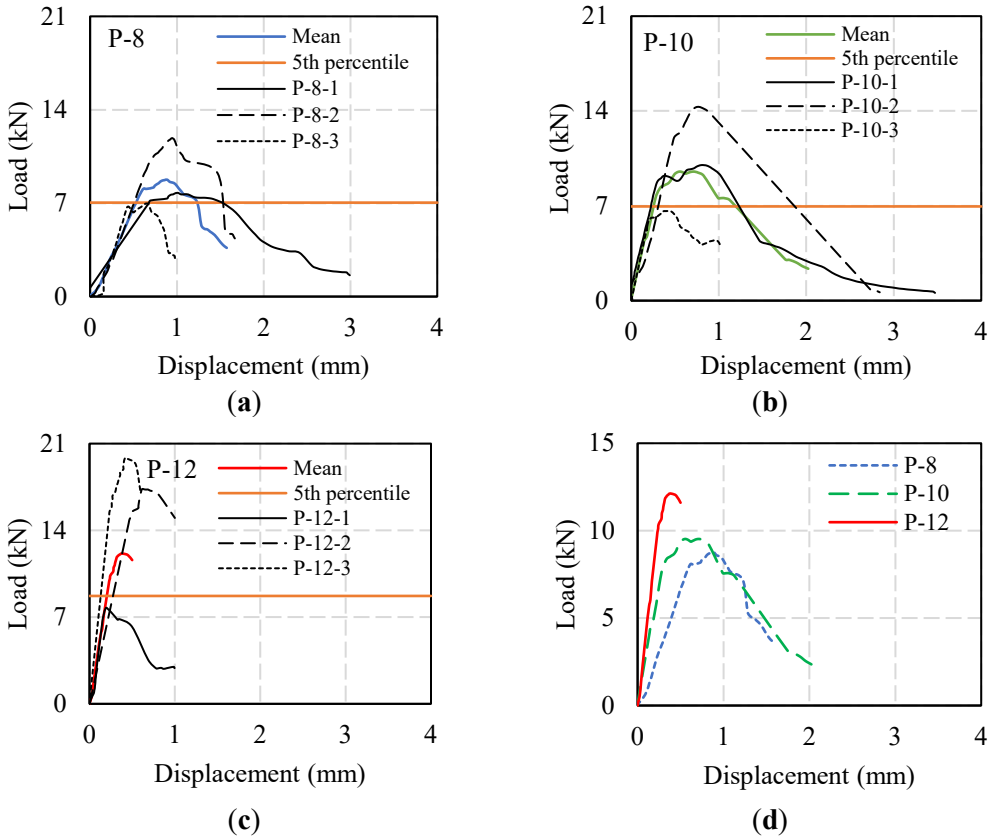

Figure 3.7. Load-displacement diagram of pullout test. (**a**) Specimen with M8 bolt; (**b**) specimen with M10 bolt; (**c**) specimen with M12 bolt; (**d**) comparison between three types of specimens.

3.4.2. Dowel-Bearing Performance

Figure 3.8 illustrates the failure of the dowel-bearing test of the brick. During the test, the load was directed evenly downwards until the specimen was broken.

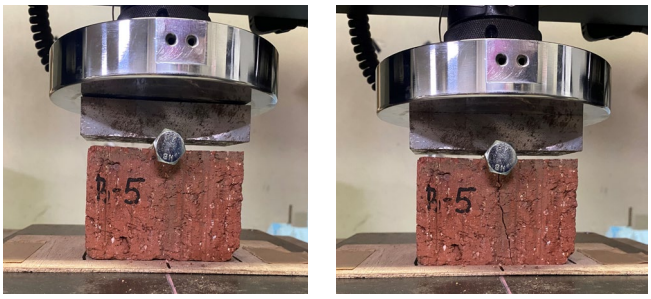

(**a**) (**b**)

Figure 3.8. Photo of dowel-bearing test of brick. (**a**) Specimen before experiment; (**b**) Failure of specimen.

Figure 3.8b shows that the cracks in specimens initiated from the top side of the brick and propagated in the vertical direction. Table 3.5 shows the experimental result of the three types of specimens. The value in the bracket indicates the coefficient of variation in Table 3.5. The mean dowel-bearing strengths of the three types of specimens are similar.

Table 3.5. Result of dowel-bearing experiment

Bolt	**The Number of Specimens**	**Load** *(kN)*	**Dowel-Bearing Strength** *(N/mm^2)*
M8	3	14.6	40.9 (66)
M10	3	19.3	46.2 (44)
M12	3	26.7	43.0 (14)
Mean			**43.4 (6.2)**

The mean strength of the dowel-bearing test (43.4 N/mm^2) is slightly reduced to 42 kN/mm^2 in the prediction calculation (EYT) for the shear resistance of the composite element.

3.4.3. Shear Performance

The experimental load-displacement diagrams of shear specimens are illustrated in Figure 3.9. We estimated the yield load for the dowel type connection of composite element obtained from the 5% offset method by McLain 1993 [43]. The yield and maximum load in Table 3.6 and Figure 3.9 are two times lower than the experimental load because the computation model is a single shear model. The yield and maximum strength, slip modulus,

and ductility ratio are shown in Table 3.6. The ductility ratio was derived by the relationship between the displacement at yield and maximum load.

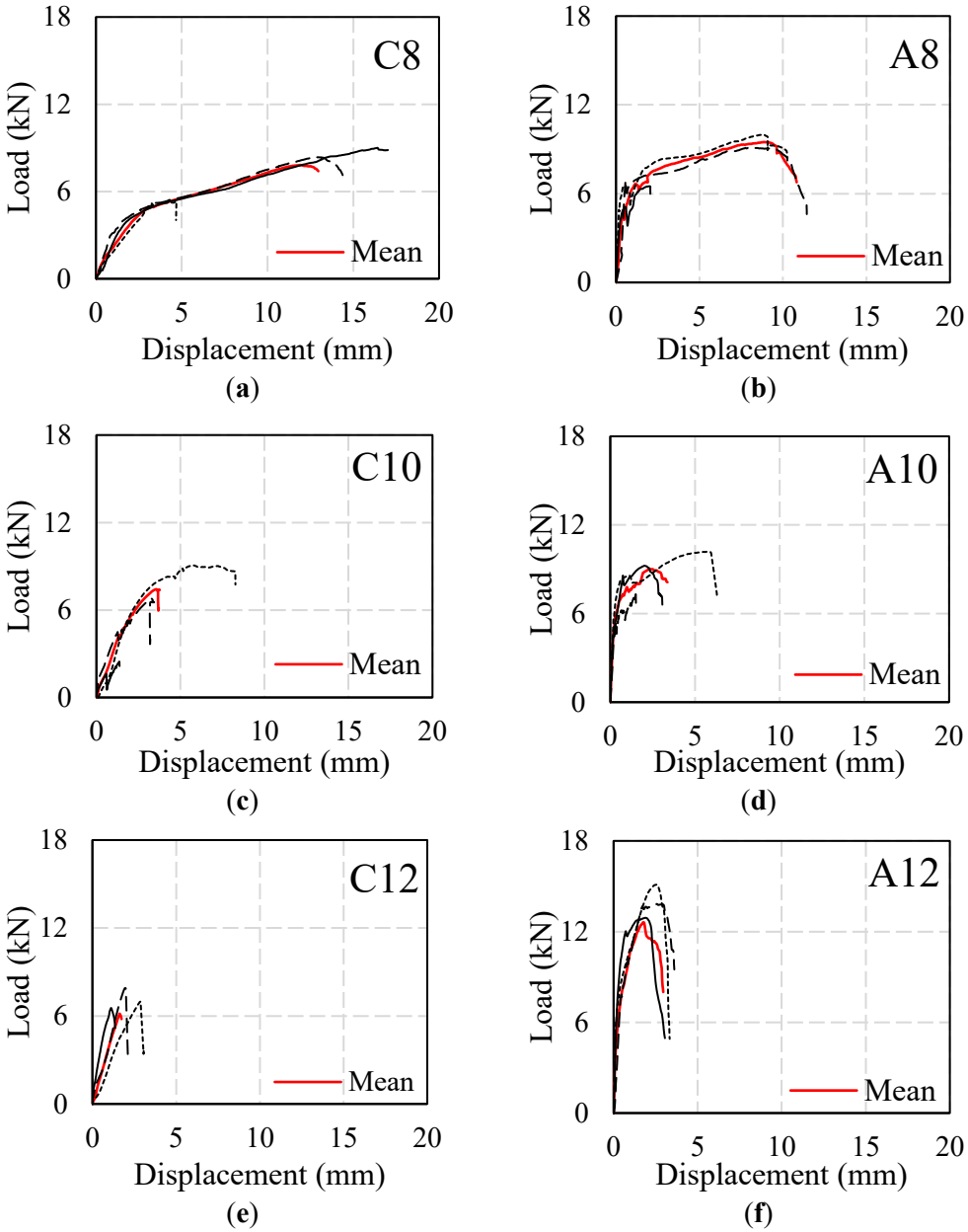

Figure 3.9. Load—displacement diagram of shear test. (**a**) C8-type; (**b**) A8-type; (**c**) C10-type; (**d**) A10-type; (**e**) C12-type; f) A12-type.

The red line highlighted in Figure 3.9 is the mean value of the three specimens. The displacement in the plastic region of one specimen in Figure 3.9a–d and the load in Figure 3.9c are less than the other two specimens. In that situation, the average value of three

specimens is estimated until the yield load of the lowest result. Beyond the yield load, the mean of two specimens is calculated in the plastic region. The load-displacement diagram in Figure 3.9a,b demonstrates the ductility characteristics. The A8 specimens had a ductility ratio of 2.45 times that of the C8 type. The yield and maximum load of A8 specimens are higher than C8 specimens by approximately 1.8 kN.

Table 3.6. Experimental result of shear test

№	Yield Load *(kN)*	Max. Load *(kN)*	Displacement at Yield Load *(mm)*	Displacement at Max. Load *(mm)*	Slip Modulus *(kN/mm)*	Ductility Ratio
C8	4.3	7.8	2.2	15.5	1.9	7.0
C10	4.3	7.4	1.5	3.7	2.8	2.4
C12	-	6.2	-	1.6	2.2	-
A8	6.2	9.5	0.5	9.2	8.7	17.2
A10	7.0	9.0	0.5	1.3	24.2	3.1
A12	11.2	12.6	0.9	2.1	30.5	1.9

Figure 3.9c,d illustrate the test result of C10 and A10 specimens. For C10 and A10 specimens, the experimental load-displacement diagram presents different results. The dimensions of the brick holes firstly checked the differences in the results of shear tests. It was concluded that the preparation of the brick hole was good. In the second, it is predicted due to excessive tightening of the bolts. During the test specimen preparation, the tightening strength of the bolt was not predetermined and measured. It is assumed that a constant tightening force gives the specimen. This reason may rely on the different results. Table 3.6 shows that the mean yield load of C10 and N8 specimens are the same. The C10 specimens have a ductility ratio that is similar to the A10 specimen. C10 specimens have a larger slip modulus than C8 specimens, although it is 12 times lower than A10 specimens. A8 and C8 specimens are approximate values for maximum shear stresses, although there is a significant discrepancy in slip modulus.

As seen from the load-displacement diagram of the C12 specimen, the load is linearly going to the maximum load and then suddenly broken. The C12 specimen shows brittle

behavior. For A12 specimens, the ductility ratio is close to the result of C10 and A10 specimens. The slip modulus of A12 is 14 times greater than C12 specimens. The maximum shear load of A12 is twice higher than C12.

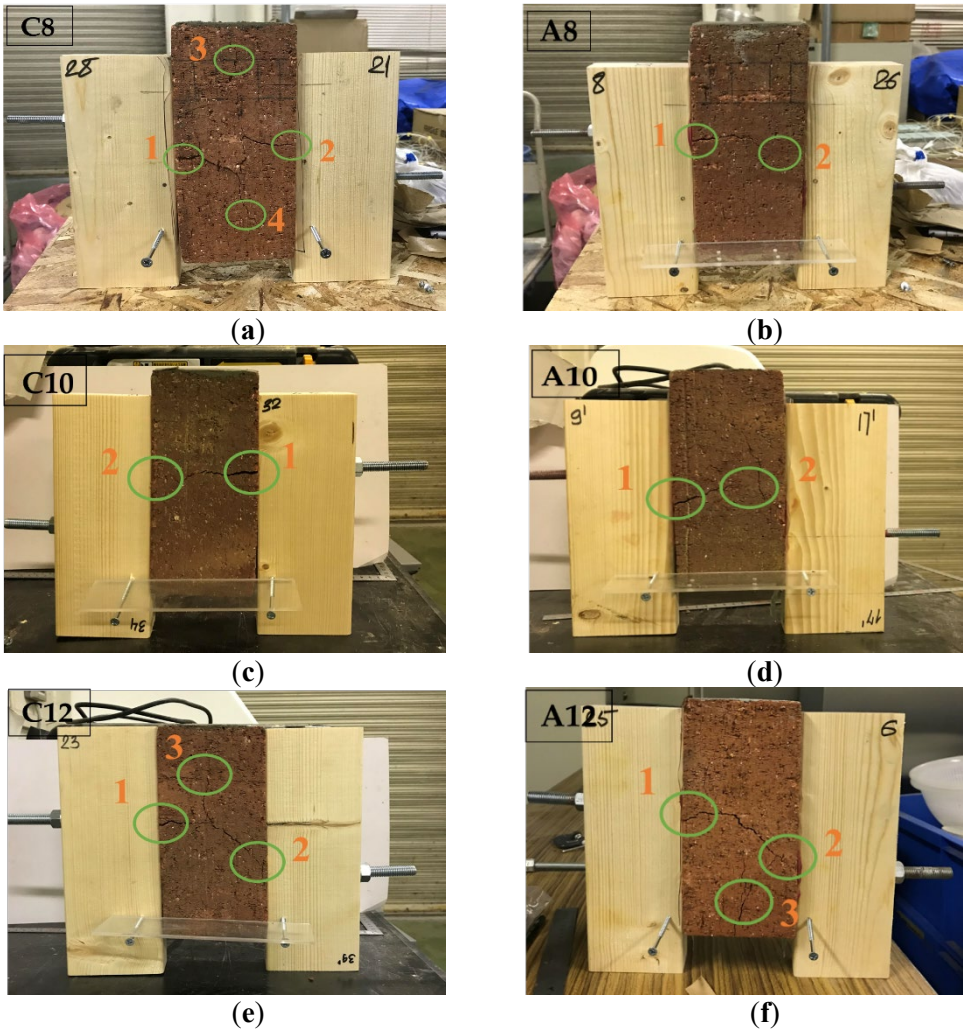

Figure 3.10. Crack on brick (main member). (**a**) N8-1 specimen; (**b**) A8-1 specimen; (**c**) N10-2 specimen; (**d**) A10-2 specimen; (**e**) N12-3 specimen; (**f**) A12-2 specimen.

Figure 3.10 shows the crack pattern of the shear test specimen. The cracks in A-type and C-type specimens were the approximate failures for all specimens, and the cracks appeared in the main member (brick). The crack started at point "1" and extended to points "2", "3", and "4" in Figure 3.10. The direction of the crack was horizontal or diagonal.

A visual inspection is presented in Figure 3.11. For C8 and A8 specimens, the bolt is deformed, and it is indicated by a red dashed line in Figure 3.11a,b. The wood part had no cracks, and the shape of the hole transferred to oval. Figure 3.11c–f shows no deformation on M10 and M12 bolts. Between the bolt-to-brick and the bolt-to-lumber, the chemical adhesive is well attached. It was not easy to separate lumber and bolt in Figure 3.11b,d,f.

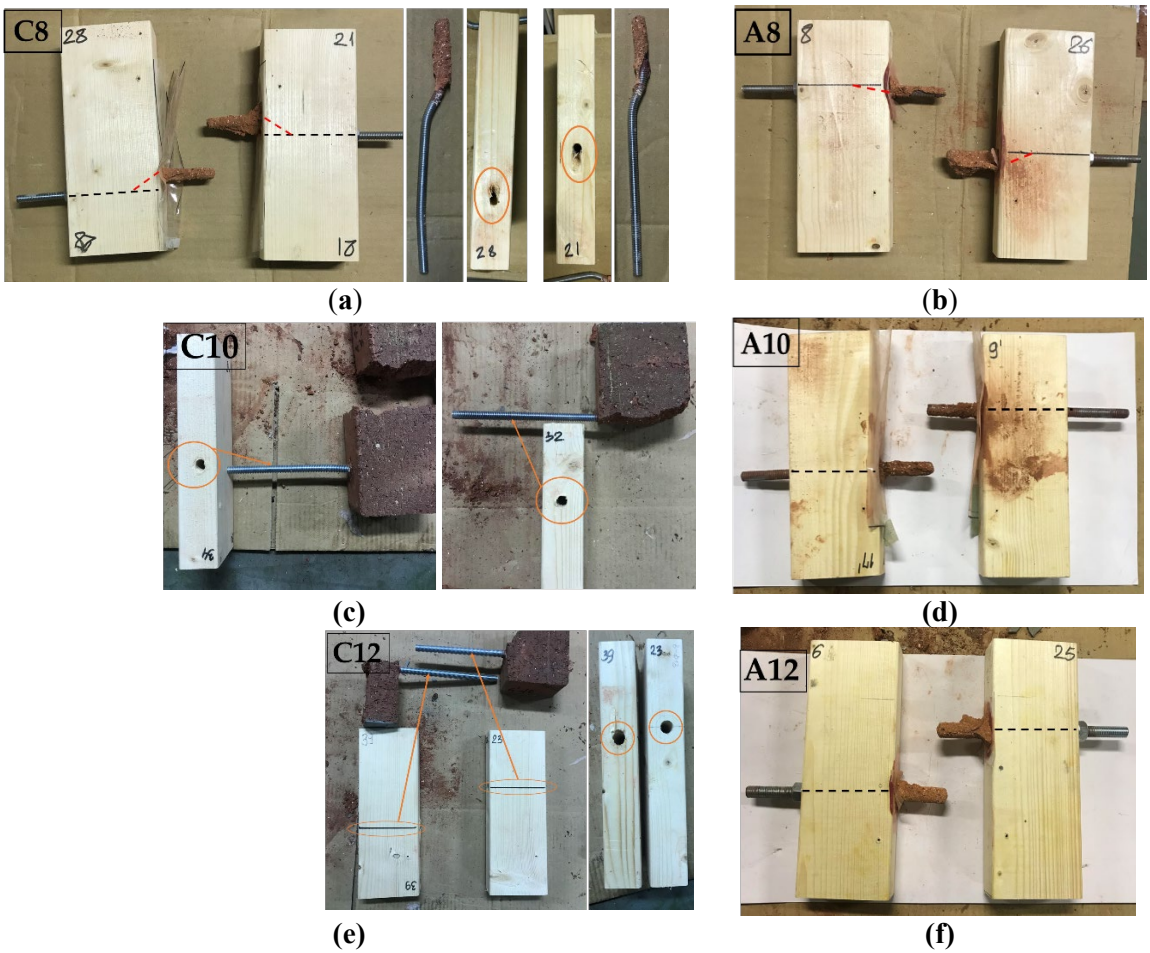

Figure 3.11. Deformation of bolt and hole of wood (side member). (**a**) C8-1 specimen; (**b**) A8-1 specimen; (**c**) C10-2 specimen; (**d**) A10-2 specimen; (**e**) C12-3 specimen; (**f**) A12-2 specimen.

3.5. Prediction of strength performance

3.5.1. Pullout strength

Theoretically, there are four types of prediction pullout failures, depending on the type of damage. The four prediction failure modes in Figure 3.12 include steel failure, cone failure, bond failure, and combined cone–bone failure [21,22,26]. Figure 3.12 illustrates the predictive states which may show such failure mode for the single brick material. When the bolt's tensile strength is less than the adhesive anchor's strength, the steel failure mode occurs [25]. This is frequently the case for long-depth anchors, according to studies. The first formula defines the steel failure formula in Table 3.7. Cone failure predicted by the second formula in Table 3.7 occurs when the depth of bolt installation is shallow [21].

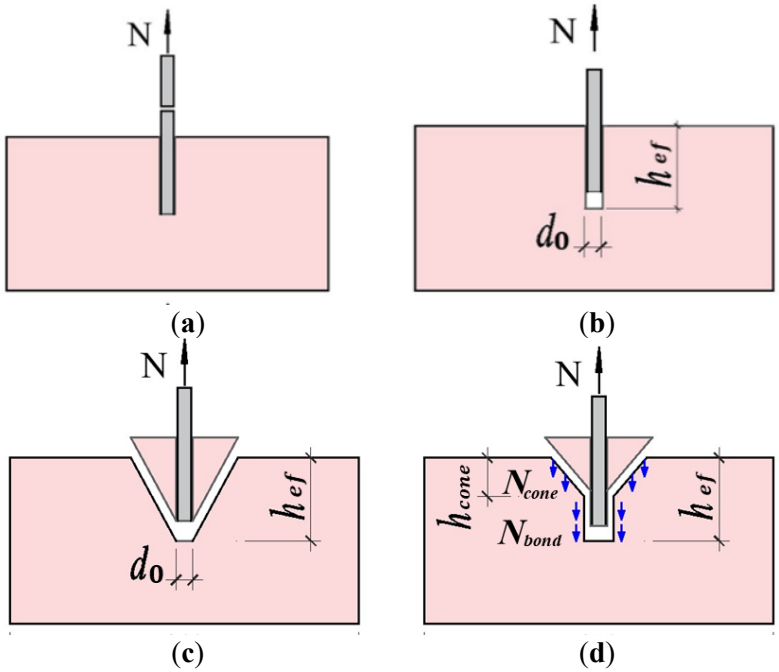

Figure 3.12. Predicted failure modes of pullout (**a**) Steel; (**b**) Bond; (**c**) Cone; (**d**) Combined cone–bond.

Where; N is pullout load (kN); N_{cone} is cone pullout load for combined cone–bond failure (kN); N_{bond} is a bond pullout load for combined cone–bond failure (kN); d_0 is hole diameter (mm); h_{ef}— effective depth of chemical adhesive (mm); h_{cone} is the chemical adhesive depth of cone for combined cone–bond failure (mm).

Table 3.7. Prediction formula of pullout strength.

№	Failure Mode	Formula
3.1	Steel	$N_u = A_s \cdot f_y$
3.2	Cone	$N_{u,m} = 0.92 \cdot h_{ef}^2 \cdot \sqrt{f_c}$
3.3	Bond (Uniform bond stress)	$N_{u,m} = \tau_0 \cdot \pi \cdot d_0 \cdot h_{ef}$
	Bond (Elastic bond stress)	$N_{u,m} = \tau_{max} \cdot \pi \cdot d_0 \cdot \left(\frac{\sqrt{d_0}}{\lambda'} tan \frac{\lambda' h_{ef}}{\sqrt{d_0}}\right)$
3.4	Combine (Uniform bond stress)	$N_{u,m} = 0.92 \cdot h_{cone}^2 \cdot \sqrt{f_c} + \tau_0 \cdot \pi \cdot d_0 \cdot \left(h_{ef} - h_{cone}\right)$
	Combine (Elastic bond stress)	$N_{u,m} = 0.92 \cdot h_{cone}^2 \cdot \sqrt{f_c} + \tau_{max} \cdot \pi \cdot d_0 \cdot \left(\frac{\sqrt{d_0}}{\lambda'} tan \frac{\lambda' \left(h_{ef} - h_{cone}\right)}{\sqrt{d_0}}\right)$

Where A_s is the cross-section area of bolt (mm^2) f_y is yielding strength of bolt (N/mm^2), h_{ef} is effective depth of chemical adhesive (mm), f_c is the compressive strength of brick (N/mm^2), τ_0 is the uniform bond stress (N/mm^2), d_0 is the hole diameter (mm), τ_{max} is the maximum bond stress (N/mm^2), λ' is elastic constant, and h_{cone} is the chemical adhesive depth of cone for combined cone–bond failure.

The cone failure formula depends on the compressive strength of the material and the installation depth. When the effective height of the bolt is at least equal to the depth of the bolt, this formula should be employed. Shear stress on the embedded surface area of the anchor exceeds the adhesive bond strength before any mode of failure [25]. In the literature review, there are two bond models: the uniform bond stress model and the elastic bond stress model [21,44]. Studies have shown that the values of these two models give the same value up to an installation depth of $40\sqrt{d_0}$ [22]. The prediction calculations for bond failure are based on the results of concrete shear tests. According to Mansur's formula , the pure shear stress of the concrete is considered by Equation (3.5). The concrete's compressive strength is directly related to the equation parameter. Concrete and brick both have material features that are similar.

$$\tau_0 = 0.56 \cdot f_c^{0.615} \tag{3.5}$$

By substituting the compressive strength of the brick into Equation (3.5), the shear stress is considered by 4.77 N/mm^2.

The combined cone–bond failure mode is given by equation (3.4) in Table 3.7. According to the study of Ronald A. Cook, the conditions for the location of one anchor are specified. The depth of the bolt is at least equal to the anchor site. Splitting cracking is expected if the anchor location is smaller than the distance criteria. In the splitting fracture, the flexural strength of brick is estimated to be 3.9 N/mm^2, (Table 2.2). As the anchor at a distance is similar to the depth of the bolt, the maximum load capacity will develop as per Equation (3.3) in Table 3.7 [22].

3.5.2. Shear strength

The bolted connection is often used to connect wood to brick. For the case of bolted connections, they receive horizontal loads in most cases for timber design. The European Yield Theory (EYT) was used to estimate the bolt's horizontal load strength. The NDS standard for estimating shear resistance of the single shear model [45] is relevant to this research. To calculate the shear resistance of the brick-to-lumber specimen, the single shear model was used. The single shear model consists of the main element, side element, and bolt. The main element in our case was brick, and the side element was SPF lumber. Failure mode, diameter, bending strength, length, and dowel-bearing strength are all factors that affect EYT [46]. There are six modes for determining the type of failure modes. The state of the load operating on the element determines the six modes. Both elastic and plastic states are included in the EYT. The elastic state depends on the dowel-bearing capacity of the main and side materials. The plastic state depends not only on the bearing capacity but also on the dowel-bending moment. In the elastic state, there is no deformation of the bolt. Only the main or side material is damaged. The fastener deforms in the plastic state due to dowel-

bending, suggesting the creation of a plastic hinge. Figure 3.13 depicts the single shear model's likely failure condition as well as the loads occurring on the elements.

Mode I failure is illustrated in Figure 3.13a,b, and the dowel-bearing strength can cause damage to the main or side member. The bolt did not deform, and it indicates the elastic state. Mode II failure is shown in Figure 3.13c. The fastener rotated but did not deform. The local crush occurred in the main or side member. Mode II failure indicates the elastic state. Mode III is shown in Figure 3.13d,e. The bolt was deformed by the dowel-bending strength. In the case of Mode III_m, the bolt section in the main member was moving down because of the bearing strength of the main member. However, the bolt section in the side member did not deform. This indicates that the dowel-bending moment takes place in this segment. The bolt belonging to the side member makes a plastic hinge. Because a plastic hinge was formed, Mode III denotes a plastic state. Figure 3.13f depicts Mode IV. Near the shear plane, a local crush occurred. In that situation, both members had two bending moments. Two plastic hinges were formed by two dowel-bending moments. Therefore, Mode IV is related to the level of plasticity.

In the EYT prediction calculation, it is assumed that the length of the main member is 50 mm, length of the side member is 89 mm. The dowel-bearing strength of the side member is 25.8 MPa. For theoretical modeling, the concrete dowel-bearing strength is 51 N/mm^2 [45]. We conducted a brick dowel-bearing experiment. The dowel diameter was identical to the bolt diameter, assuming chemical adhesive for the C-type specimen. The bolt diameter was 2 mm greater than the dowel diameter for the A-type specimen.

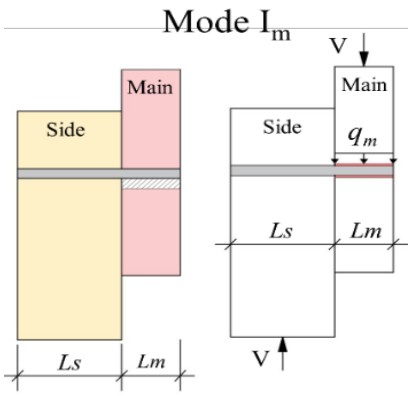

$$V = q_m \cdot l_m$$

(a)

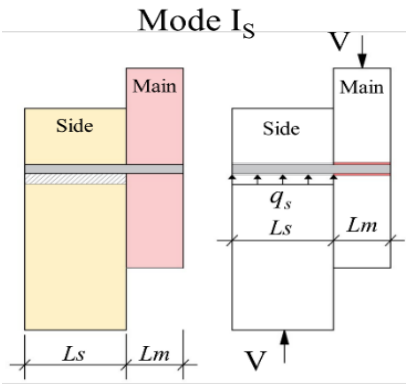

$$V = q_s \cdot l_s$$

(b)

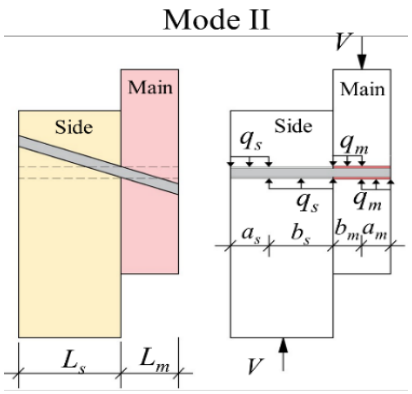

$$V^2\left(\frac{1}{4q_m}+\frac{1}{4q_s}\right)+V\left(\frac{l_m}{2}+\frac{l_s}{2}\right)-\left(\frac{q_m \cdot l_m^2}{4}+\frac{q_s \cdot l_s^2}{4}\right)=0$$

(c)

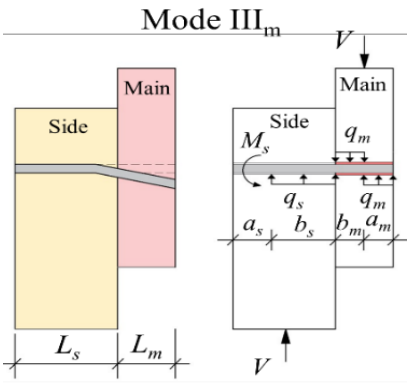

$$V^2\left(\frac{1}{4q_m}+\frac{1}{2q_s}\right)+V\left(\frac{l_m}{2}\right)-\left(M_s+\frac{q_m \cdot l_m^2}{4}\right)=0$$

(d)

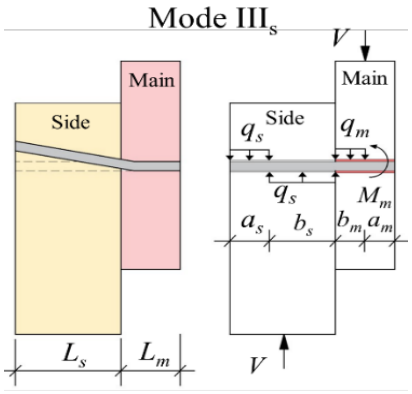

$$V^2\left(\frac{1}{2q_m}+\frac{1}{4q_s}\right)+V\left(\frac{l_s}{2}\right)-\left(M_m+\frac{q_s \cdot l_s^2}{4}\right)=0$$

(e)

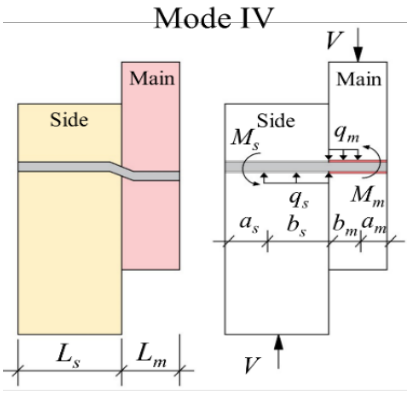

$$V^2\left(\frac{1}{2q_m}+\frac{1}{2q_s}\right)-(M_m+M_s)=0$$

(f)

Figure 3.13. Yield modes and formula. (**a**) Mode I_m; (**b**) Mode I_s; (c) Mode II; (**d**) Mode III_m; (**e**) Mode III_s; (**f**) Mode IV

Where V is the shear force of the dowel type fastener (N), q_m ($F_m \cdot l_m$) is the main member dowel-bearing resistance (N/mm), q_s ($F_s \cdot l_s$) is the side member dowel-bearing resistance (N/mm), M_m is the maximum moment in the main member ($N \cdot mm$), and M_s is the maximum moment in the side member ($N \cdot mm$).

3.6. Discussion

3.6.1. Pullout

Figure 3.12 depicts the prediction failure modes, whereas Table 3.7 highlights the calculations. Figure 3.14 represents the comparison result between the experimental and predicted pullout resistances. The predicted pullout failure comprises steel, cones, bonds, and combined bond–cone failure. The mean maximum load of the pullout test is compared with the predicted failure loads.

Steel failure prediction load differs by more than 40% from the test load. There was no damage to the bolt. The steel failure is less likely to occur due to the shallowness of the bolt installation.

The predicted cone failure load indicates 12.9 kN for three types of specimens. Since cone failure is directly related to the compressive strength of the brick and the installation depth, the same assumptions are given for the three types of pullout specimens. For specimens with M8 bolts, the experimental and theoretical resistance difference is 48%, 35% for specimens with M10 bolts, and 7% for specimens with M12 bolts. The formula for predicting cone failure is that the anchor distance from the concrete edge is equal to the bolt's installation depth. In our case, the anchor distance from the brick edge around 25 mm is less than the bolt installation depth (50 mm). This type of failure mode does not occur in the brick because the requirements of the cone failure formula cannot provide for a single brick.

Bond failure [23] can occur between the bolt and the chemical adhesive or the chemical adhesive and substrate element (brick). The adhesion between bolt–epoxy and epoxy–brick

has illustrated good results for our experiment. There was no failure in their connection. However, the prediction load of bond failure is close to the test load in Figure 3.14.

The combined cone–bond failure exhibits both bond and cone failure properties. There is a discrepancy of about 20% in the three types of specimens when the test load is compared to the predicted combined cone–bond failure. The experimental failure modes are both the combined cone–bond failure and splitting failure.

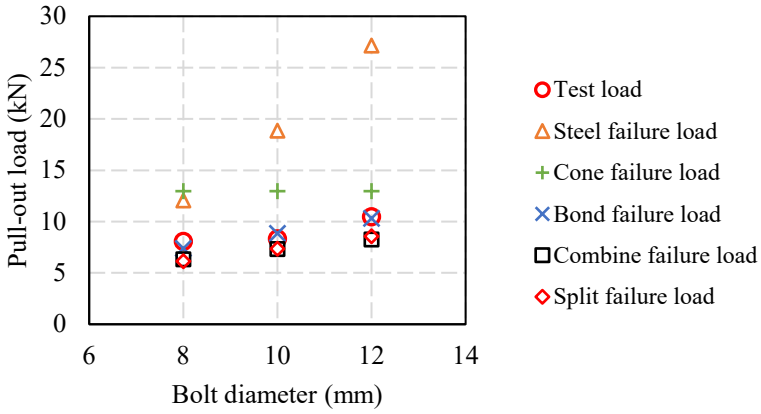

Figure 3.14. Comparison results of pullout test and prediction estimation.

As shown from the four failure mode assumptions shown in Figure 3.12, it is assumed that the combined cone–bond failure and splitting failure occurred because of the experiment in Figure 3.6. Failure theories indicate the minimum load value of all possible failure modes. The minimum loads of the prediction calculations are related to the combined cone–bond failure and splitting failure. It is suggested that the estimations of the predicted failure modes and loads are considered reasonable in this study. No case showed damage to the threaded rod during the pullout test. The failure occurred in the weak resistance surface with the high-stress concentration. Our pullout experimental result showed that the brick surface had low resistance, and then the connections between brick to epoxy and epoxy to bolt showed the brick material's damage. The chemical anchor in the brick wall can show

sliding failure. To attach the timber to the existing brick wall, the main role of timber is related to reducing the movement of brick and chemical anchors in a parallel direction to the load. The load acting on the out-of-plane wall concentrates the tensile force on the chemical anchor. In the case of only brick failure, it is necessary to withstand the tensile load for a thick threaded rod having high stiffness and strength. Therefore, the strengthened brick walls with wood are important to reduce out-of-plane damage.

3.6.2. Shear

Table 3.8 highlights the comparison results between the experimental and theoretical shear loads. It can be a reasonable estimation value, as seen in the comparison result. The minimal load of EYT modes determines the predicted yield load. For all specimens in the estimation, the minimum yield load of EYT modes is Mode IV. Mode IV failures were found in C8 and A8 specimens, but failures in other specimens were a different mode. As the bolt diameter increases, the yield load is the same for C8 and C10 test results in Table 3.8. As for the expected yield load of C8 and C10, it increases depending on the diameter of the bolt. For the A-type specimen, the expected and experimental shear load grows by raising the diameter of the bolt. The effect of bolt diameter for C-type specimens is low for test yield load.

Figure 3.15 illustrates the load-displacement curve of the shear test and the minimum load of EYT mode. In Figure 3.15, a narrow cross-section fastener (M8 bolt) can show the highest plasticity. In Figure 3.15a, the maximum shear load decreases as the bolt diameter increases.

Table 3.8. Comparison of experimental and theoretical results of shear specimen.

Type	Yield load *(kN)*	
	Expected *(Mode IV)*	**Experiment**
C8	4.2	4.3
C10	5.7	4.3
C12	8.3	6.2
A8	6.6	6.2
A10	8.3	7.0
A12	11.3	11.2

The experimental maximum shear load of the A-type specimens grows in Figure 3.15b, besides bolt diameter increases. As shown in Figure 3.15a,b, the ductility grows with declining the bolt diameter. The stiffness of A12 can show the highest performance in Figure 3.15b. However, the ductility ratio of the A12 specimen is the lowest value in Table 3.8.

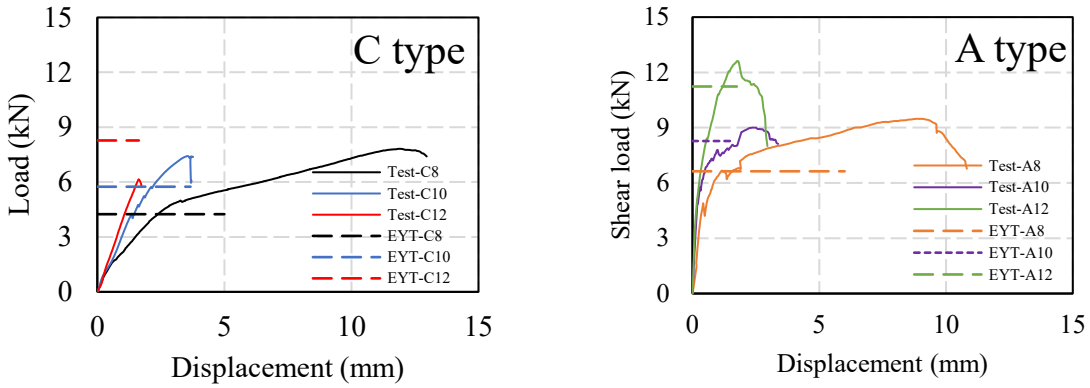

(a) **(b)**

Figure 3.15. Load-displacement diagram of shear test. (**a**) N-type; (**b**) A-type.

The ductility ratio of A-type specimens in Table 3.8 is higher than C-type specimens. The mean slip modulus of the C-type specimens is 2.3 kN/mm in Table 3.8. However, the slip modulus of the A8 specimen has the lowest value compared with A10 and A12 specimens, but it is four times higher than the slip modulus of the C-type specimen. It suggests that applying chemical adhesives to both the main and side elements increases the strength and slip modulus of the specimen. The use of chemical adhesives in the strengthening process

can provide high strength between brick-to-lumber material, according to experimental and theoretical results.

3.7. Conclusions

This chapter determined and compared the pullout and shear strengths of brick and brick-to-lumber material experimentally and theoretically. The prediction formulas of the pullout and shear strength could give a suitable result.

The pullout strength depends on the bolt diameter. The predicted failure load illustrates the combined cone–bond failure load. The experimental failure mode is also the combined cone–bond failure until the load reaches the maximum value. Then splitting failure occurs when the maximum load gradually decreases. For the single brick, the probability of steel and cone failure occurring is small.

The yield shear strength of the composite specimen (brick-to-wood) on the chemical anchor is reasonable to expect in the European Yield Theory (EYT). However, it is complex to determine the failure mode. When it comes to increasing the strength of masonry construction, the A12 type is recommended since it provides excellent strength and stiffness.

CHAPTER IV.

EXPERIMENTS OF UNREINFORCED AND REINFORCED BRICK WALLS

4.1.Introduction

This study emphasizes the in-plane shear behavior of the strengthening solution for the unreinforced brick masonry wall using the SPF (spruce, pine, and fir) frame and plywood panel. Advantage of our retrofitting technique is compared with other research, cost-effective and lightweight material, easy assembling, and masonry-to-timber connection has high stiffness. The effective connection which is an M12 bolt with a chemical anchor [30] was selected in this study. The aim of chapter 4 is to carry out experimental study of the unreinforced and reinforced brick walls.

4.2.Wall specimen

The unreinforced masonry (URM) wall and strengthened masonry (RM) wall with timber frame and plywood panel were constructed and tested at the laboratory of the Engineering faculty at the Kinki University in Japan [47]. The brick wall (BW), reinforced brick wall with timber (BW-T), and reinforced brick wall with timber including the hold-down anchor (BW-TA) are the three walls. The boundary condition of walls is that the upper part of the walls is free, and the bottom part of the wall is clamped by C-shaped channels on both sides. C-shaped channel is connected to the base of the experimental frame. Table 4.1 shows the

detailed wall dimensions, the pre-compressive stress. Dimension of BW-T and BW-TA wall includes timber frame and plywood panel in Table 4.1.

Table 4.1. Description of wall specimen

Wall index	**Dimension** *(mm)*	**Pre-compression stress** *(N/mm^2)*	**Ratio of height to length**
BW	1090 x 1060 x 100		
BW-T	1090 x 1060 x 201	0.2	0.97
BW-TA	1090 x 1060 x 201		

4.2.1. BW wall

Before building the brick wall, a wooden formwork in Figure 4.1a was prepared and placed on the base C-shaped channel beam. The sand-cement ratio of the cement mortar is 1:6, and the mortar thickness of the head and bed joint is 10 mm. A total of 15 brick layers were laid on the brick wall. The experimental walls are the single-leaf brick walls, and the wall specimens were built in June 2021, and the BW wall in Figure 4.1c was tested in early December 2021. The walls were built in a separate area from the experimental frame and placed on the experimental frame using a crane. The style of running bond was employed for the brick wall construction. After the wall was completed, the walls were covered with a polyethylene plastic sheet in Figure 4.1b and were stored in the Kindai University laboratory until the experimental day.

(a)

(b)

(c)

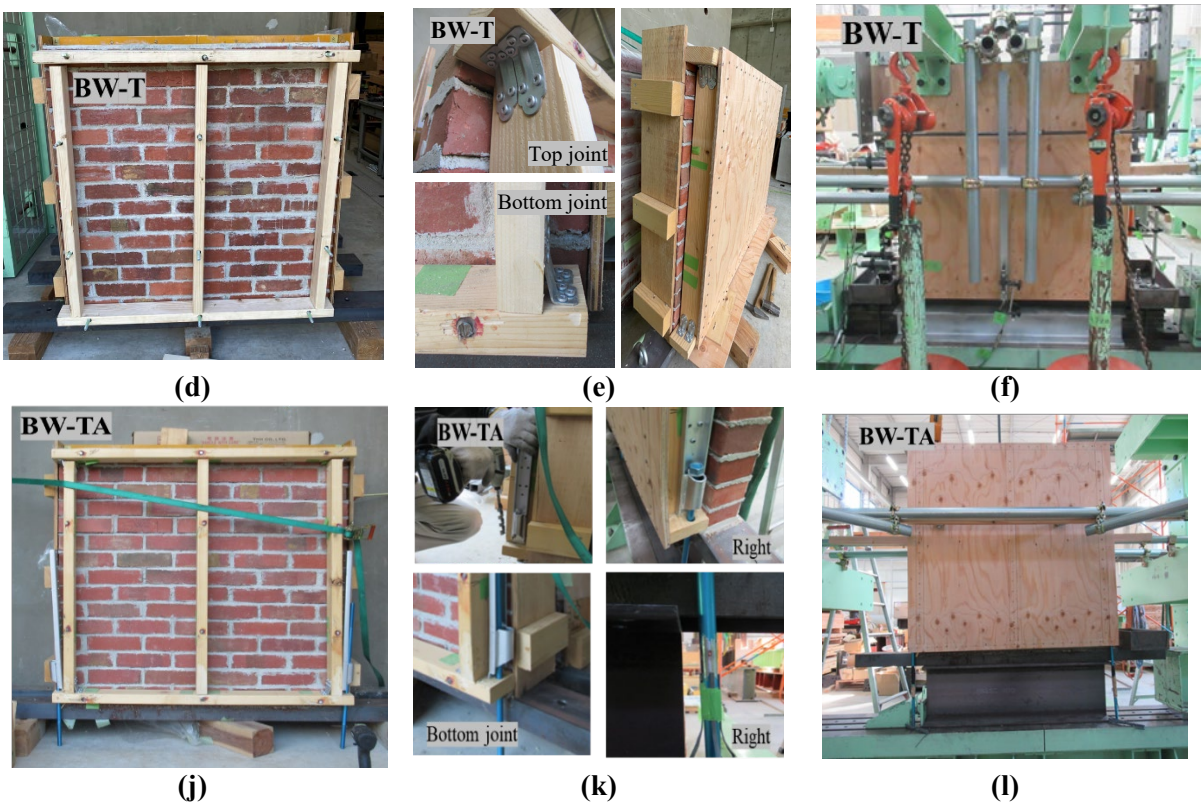

Figure 4.1. Photos of wall preparation. (a) Assembly site and mortar preparation; (b) BW wall with polyethylene plastic sheet; (c) BW wall on experimental base; (d) Brick wall with timber frame (BW-T); (e) The joint of timber frame; (f) Brick wall with timber frame and plywood panel (BW-T); (j) Brick wall with timber frame (BW-TA); (k) Bottom joint of BW-TA wall; (l) BW-TA wall on experimental base.

4.2.2. BW-T wall

The construction procedures of BW-T wall are illustrated in Figure 4.1d,e,f. The construction of BW-T and the stored condition are the same as the BW wall. There are several steps of installation to strengthen a brick wall with wooden materials. In the first step, the brick was pre-drilled, and the hole depth was 50 mm. The hole diameter was 2 mm greater than the M12 bolt diameter. Then the chemical adhesive is filled into two-thirds of the hole, and the bolt is poured slowly. Once the bolts are installed at the desired depth, the prepared specimens should be cured at ambient temperature for 24 hours. The prepared bricks were placed in marked positions during the brick wall construction. In the second step, SPF lumbers (2x4) were installed on the brick wall after 28 days. The chemical adhesive

was used to bond the brick-to-bolt and lumber-to-bolt. SPF lumber was placed on the brick wall and then injected the chemical adhesive into a gap between the bolts and the hole of lumber. As shown in Figure 4.1d, the length of bolt (200mm) is longer than width (89mm) of SPF lumber. Therefore, the excess length of the threaded rod was cut as shown in Figure 4.1e. After the chemical adhesive had hardened, the corners of the timber frame were secured with two corner hardware (DH tight corner guardian №1460) using 6 flat heat screws (ø5.6 mm × 45 mm) in Figure 4.1e. The corner hardware was connected outside the frame intersection for BW-T wall in Figure 4.1e. The final installation step is to connect the plywood panel to the SPF lumber. The plywood was pre-cut to the desired dimension. The plywood panel was nailed to SPF lumber using CN 65 nails. The nail space is 50 mm, and the nails are connected to all lumbers in the horizontal and vertical directions. When the nails are struck, it can reduce the adhesion strength of the brick-to-mortar. Figure 4.1e shows a photo connecting the lumber and plywood panel to the brick masonry wall. The strengthened masonry wall was moved to the test frame using a crane in Figure 4.1f.

4.2.3. BW-TA wall

For the BW-TA wall in Figure 4.1j,k,l, the assembling steps are all the same as the BW-T wall. The corner hardware was placed outside the top joint and inside the bottom joint, as shown in Figure 4.1j,k. Two hold-down bolt were installed on both sides of the timber frame to avoid the rocking failure in Figure 4.1j,k,l. The capacity of the bolted hold-down is 50 kN and the hold-down is attached to the SPF lumber by 18 screws in Figure 4.1k. The bolt diameter is 14.54 mm, the bottom part of the bolt is connected to the experimental frame's base in Figure 4.1l, and the top part of the bolt is connected to the hold-down by tightening the washer in Figure 4.1k. To measure the axial load on the bolt during the cyclic load, four

strain gauges were attached to each bolt in Figure 4.1k. After placing the strain gauges, the coating material was used to protect from moisture or waterproofing of strain gauges bonded on the surface, and the scotch VM (vinyl/mastic) tape was covered on the coating material.

4.3. Experimental setup

Figure 4.2 shows a schematic set-up of the BW and BW-T walls as well as the set-up photo of the BW-TA wall. The top of the masonry wall was subjected to a static vertical load and the top corner of the wall specimen was subjected to a cyclic horizontal load. The wall was subjected to a pre-compression stress of 0.2 N/mm2. Two steel beams were placed on the top side of the wall specimen to apply the pre-compression stress, and one steel beam has two steels suspended 5 kN loads (Fig.4.2). Following the crane transfer of the prepared masonry wall was moved to the test frame, additional horizontal supports were installed on the front and back side of the wall as shown in Figure 4.2e, f. In addition, the horizontal supports were double attached to the test frame. Figure 6g shows a rubber wheel being placed between the wall specimen and the additional support. When a horizontal load is applied to a brick wall, the rubber wheel rotates freely. It is assumed that the additional supports do not affect the result of the brick wall under the horizontal cyclic load. A C-shaped steel beam was placed at the top and bottom parts of the BW wall, and the steel plate was on the top part of the BW-T and BW-TA walls. The metal base of the test frame is bolted to the concrete floor of the laboratory. The oil jack and load cell have a capacity of 300 kN and are placed on the upper edge of the wall in the horizontal direction. The steel plates were placed on both sides of the upper edge of the wall in a vertical direction, and both steel plates were connected by long bolts to each other as shown in Figure 4.2a.

During the experiment, transducers were placed to measure the displacements of the BW, BW-T, and BW-TA walls, as shown in Figure 4.2a. The transducers were placed on the brick side of the wall specimen to measure the horizontal, vertical, and diagonal displacements. Transducers (capacity 50 mm, Tokyo Measuring Instruments Lab) were placed in the middle of the upper (index T1) and lower (index T2) parts of the wall specimen as shown in Figure 4.2a. For the vertical displacement of the wall, two transducers (index T3 and T4) were placed on both sides of the lower edge of the wall. To measure the displacement in the diagonal direction, transducers (indexes T5 and T6) were placed at the lower two corners of the wall. The nail was attached to the two small squares of wood that were glued to the top edges of the wall. A thin wire rope (index 23 in Figure 4.2a) is attached to a nail in the wooden piece and connected to the transducer (T5 or T6) in the diagonal direction.

An attempt was made for the reinforced walls to measure the relative displacement between the brick wall and the timber part. The transducers (index T9 to T14) were placed at the same level on the brick wall and wooden frame in Figure 4.2d, g to measure the relative horizontal displacement. The three transducers were placed at the top, middle, and bottom positions in the vertical direction on the brick and timber sides of the BW-T and BW-TA walls. While pre-compression stress was applied to the wall, the transducers (index T7 and T8 in Figure 4.2b) were placed in the middle of the lower part of the wall and then removed after the pre-compression stress was applied to the test wall.

Under cyclic loading, the brick walls were tested using the displacement method of control. Under the lateral cyclic load, a load control and the corresponding displacement in positive and negative loadings were measured. The first and second cycles each had three

runs. Table 4.2 shows the cyclic numbers, rotational angle, and horizontal maximum displacement. The displacement protocol was arbitrarily defined by the authors. Until the ninth cycle, all walls were tested. The horizontal load cell's capacity is necessary for the test. It is assumed that the experiment will be terminated if the load cell reaches its limitation.

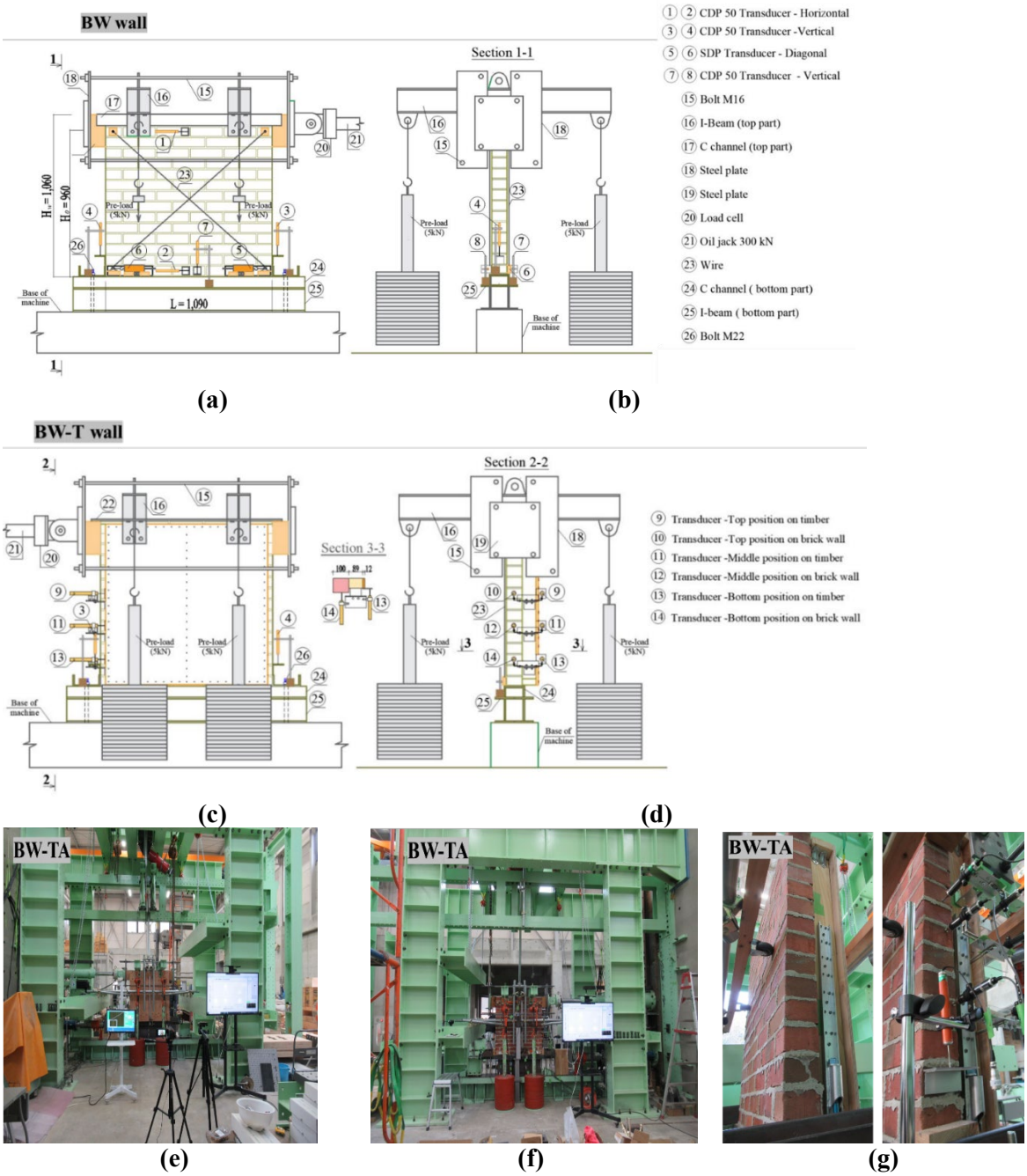

Figure 4.2. Test set-up for wall specimens. (a) Schematic view of back side (BW wall); (b) Elevation view (BW wall); (c) Schematic view of front side (BW-T wall); (d) Schematic view of

elevation (BW-T wall); (e) Front side photo of BW-TA wall; (f) Back side photo of BW-TA wall; (g) Elevation photo of BW-TA wall.

Table 4.2. Rotational angle and maximum displacement

Cycle №	**1**	**2**	**3**	**4**	**5**	**6**	**7**	**8**	**9**
Rotation	1/2000	1/1000	1/500	1/300	1/200	1/150	1/100	1/75	1/50
Displacement (mm)	0.5	1.0	1.9	3.2	4.8	6.4	9.6	12.9	19.3

4.4. Experimental results

The elastic modulus of the wall was determined during the pre-load process installation, as shown in Table 4.3. In Table 2.4, the wall elastic modulus presents the approximate value for the elastic modulus of the cement mortar specimen. According to the study [18], the mortar stiffness was reason for the small modulus of elasticity. It is assumed that height to thickness ratio is different between prism and wall specimen. That's why it is considered that the elastic modulus shows different values in Table 2.8 and Table 4.3. The hysteretic curve, the envelope curve, failure modes, the load at first crack and the corresponding displacement, and the maximum load and the corresponding displacement were used to evaluate the experimental findings of the walls under horizontal cycle load. Figure 4.3 shows the relationship between steps and experimental wall's top displacement.

Table 4.3. Elastic modulus obtained from pre-compression stress

Properties	**Unit**	**BW**	**BW-T**	**BW-TA**
Pre-compression stress	N/mm^2		0.2	
Elastic modulus	N/mm^2	2509	2790	3312

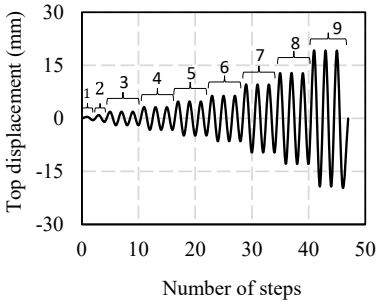

Figure 4.3. Steps and top displacement relation.

4.4.1. Hysteretic response and failure

Deformation measurements were taken in the horizontal, vertical, and diagonal directions. As shown in Figure 4.2a, the horizontal relative displacement is defined as the difference between transducers T1 and T2. The drift angle in Figure 4.4a shows the horizontal relative displacement divided by the wall height, indicated as a radian. In the case of wall height, transducer T1 was placed 960 mm from the bottom bricks to record horizontal displacement. The tensile and compression displacement can be recorded in the vertical direction during cyclic horizontal loading. The drift in Figure 4.4b is assumed that the tensile displacement is divided by the tensile length of the wall. When the rotation deformation occurs in the wall, it is assumed that the vertical rotational angle is equal to the horizontal rotational angle. The diagonal tension deformation is used to calculate the drift in Figure 4.4c. To determine the drift in that case, several simplifications were assumed. Transducers T5 and T6 are placed in the lower two corners of the wall to measure displacement in a diagonal direction as shown in Figure 4.2a. The tensile displacement measured by the T5 transducer increased as the positive load acted on the wall. The dashed red line in Figure 8c depicts the compression diagonal contraction and the tensile diagonal extension. The cosine rule can be used to determine the angle between the two elongated slopes ($l_{a'-5'}$, $l_{5'-6'}$) of the created deformation. For simplification, the length of the deformed slope ($l_{a'-5'}$ and $l_{5'-6'}$) is considered equal to the length of the undeformed state (l_{a-5} and l_{5-6}) in Figure 4.4c. In determining the angle by the cosine rule, it is necessary to determine the diagonal length of the compressed part. Therefore, it was assumed that the compressed of the diagonal was equal to the elongation of the tensile diagonal. Considering the above simplifications, the drift was determined by diagonal measurement.

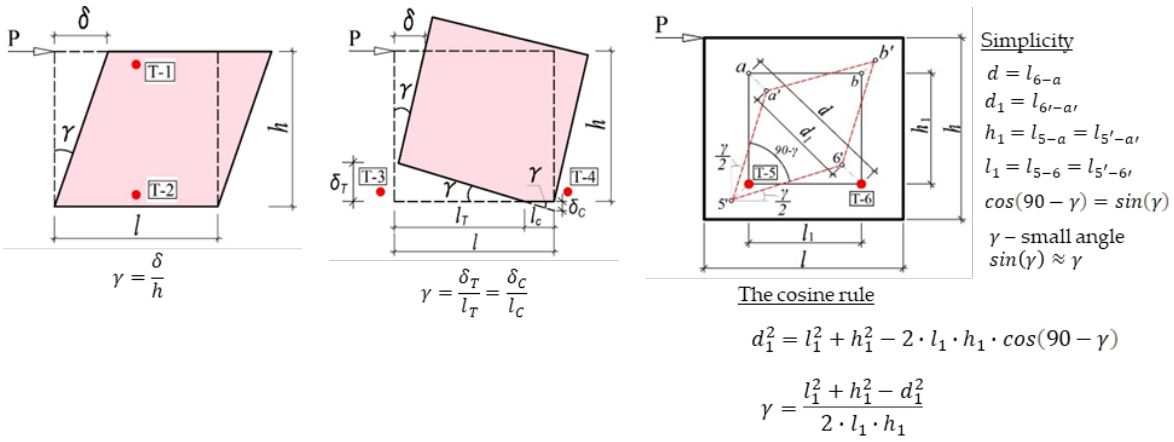

(a) **(b)** **(c)**

Figure 4.4. Deformations of panel. (a) Shear deformation; (b) Rotation of rigid-body; (c) Diagonal deformation.

Figure 4.5 illustrates the load-drift hysteretic curve and the envelop curve obtained under cyclic horizontal load. The envelope curve is created by connecting the maximum load line in each cycle. As shown in Figure 4.5, the direction in which the oil jack pushes to the wall specimen indicated the positive loading, whereas wall specimen is pulled in negative loading.

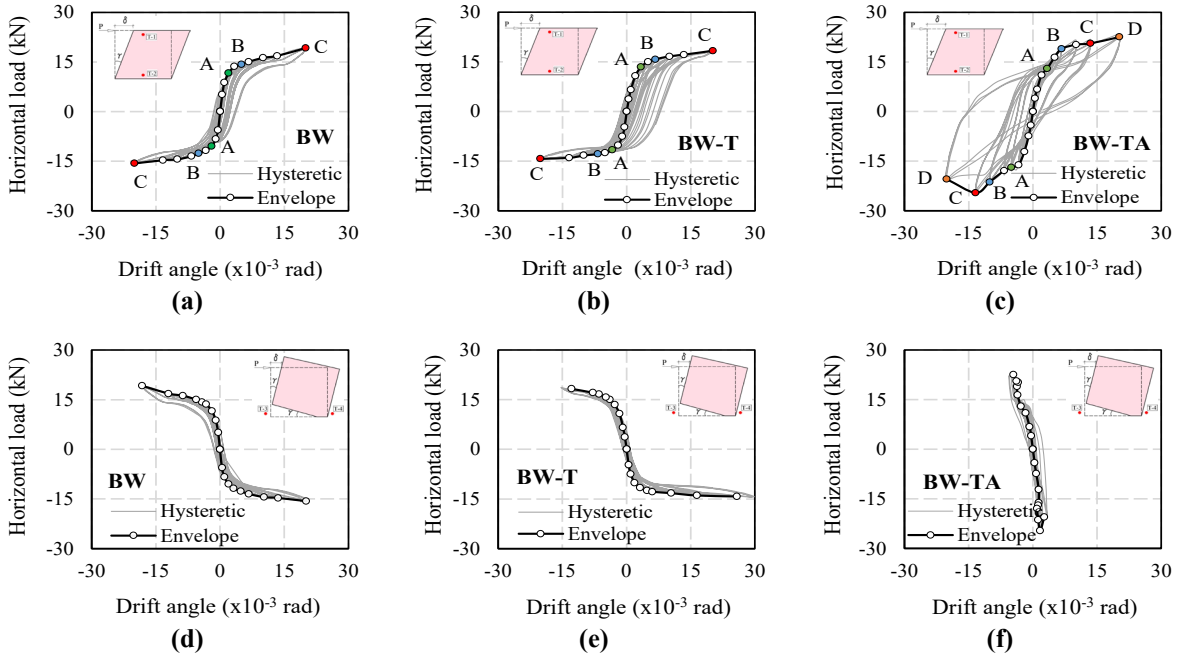

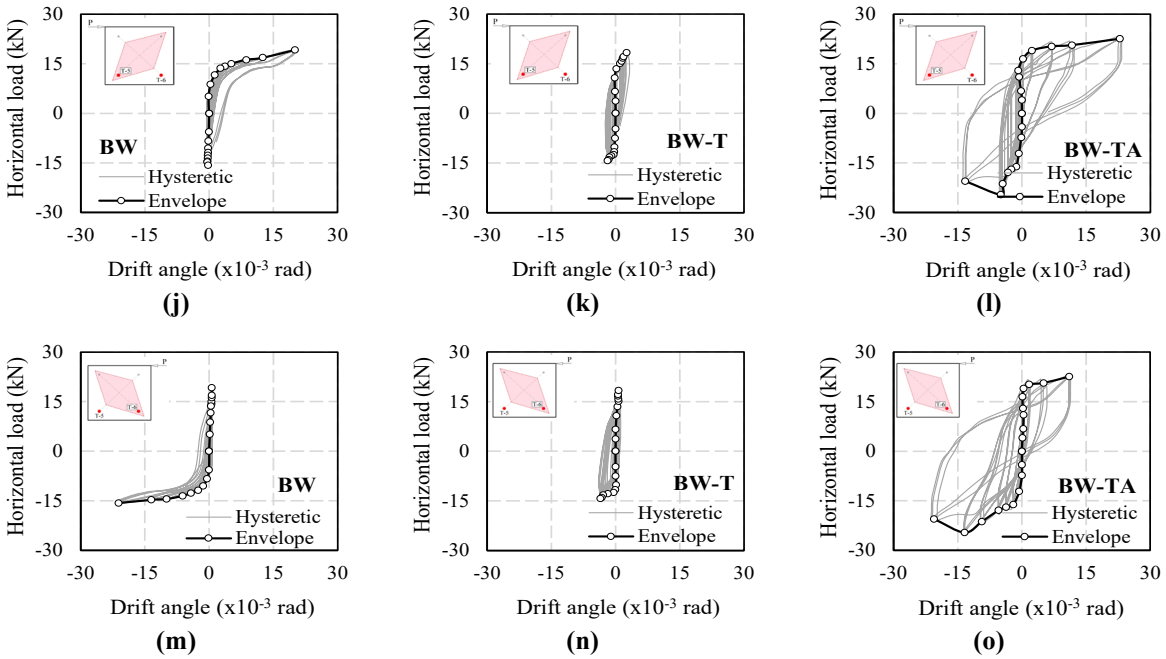

Figure 4.5. Horizontal load- drift hysteretic and envelope curve of experiments. (a) BW wall (horizontal); (b) BW-T wall (horizontal); (c) BW-TA wall (horizontal); (d) BW wall (vertical); (e) BW-T (vertical); (f) BW-TA wall (vertical); (j) BW wall (diagonal T5); (k) BW-T wall (diagonal T5); (l) BW-TA wall (diagonal T5); (m) BW wall (diagonal T6); (n) BW-T wall (diagonal T6); (o) BW-TA wall (diagonal T6).

4.4.2. BW wall

BW wall was tested until failure mode in Figure 4.6b. The load-drift angle curve of BW wall is illustrated in Figure 4.5a,d,j,m. The drift angle in Figure 4.5a is defined by the horizontal measurement and the load-drift angle curve is the S shape. The initial slope is going linearly until "A" point and then the line slope decreases and shows a nonlinear characteristic in Figure 4.5a,b,c. The first crack was appeared in "A" point and the load at the first crack (the 3rd cycle) is 11.6 kN (-10.5 kN) in the positive (negative) loading. The drift angle in Table 4.4 is obtained from the horizontal measurement. The corresponding drift angle at the first crack is 2.0 x 10^{-3} rad and 20.0 x 10^{-3} rad at the maximum load in both loading direction. The initial stiffness is defined by the load at the 2nd is over the displacement at the 2nd cycle. The initial stiffness is 9.2 kN/mm (8.6 kN/mm) in the positive

(negative) loading in Table 4.4. The load at the initial crack is 72.4% (71.6%) of the maximum load in the positive (negative) loading.

Table 4.4. Result of wall experiment

Loading direction	Wall	P_{cr} (kN)	γ_{cr} (10^{-3} rad)	P_{max} (kN)	γ_{max} (10^{-3} rad)	Initial stiffness K_e (kN/mm)
Positive	BW	11.6	2.0	19.2	20.1	9.2
	BW-T	13.5	3.3	18.3	20.2	6.9
	BW-TA	13.0	3.3	22.5	20.3	7.2
Negative	BW	-10.5	-2.0	-15.7	-20.0	8.6
	BW-T	-11.6	-3.3	-14.3	-20.1	7.8
	BW-TA	-16.9	-5.0	-24.6	-13.4	7.7

During the horizontal load, the drift angle from the vertical measurement increased for the BW wall in Figure 4.5. It means that the bottom of the BW wall is uplifted. The wall is assumed to be damaged due to bending deformation. Figure 4.5j,m show drift angles defined from the transducers 5 and 6, respectively. In Figure 4.5, the drift angle increases under the positive loading, but the very small displacements were recorded under the negative load. In Figure 4.5m, the drift angle raises under the negative loading, but the small displacements were measured under the positive loading. As the result of the diagonal measurement, it is assumed the BW wall is deformed along the diagonal direction from its original state.

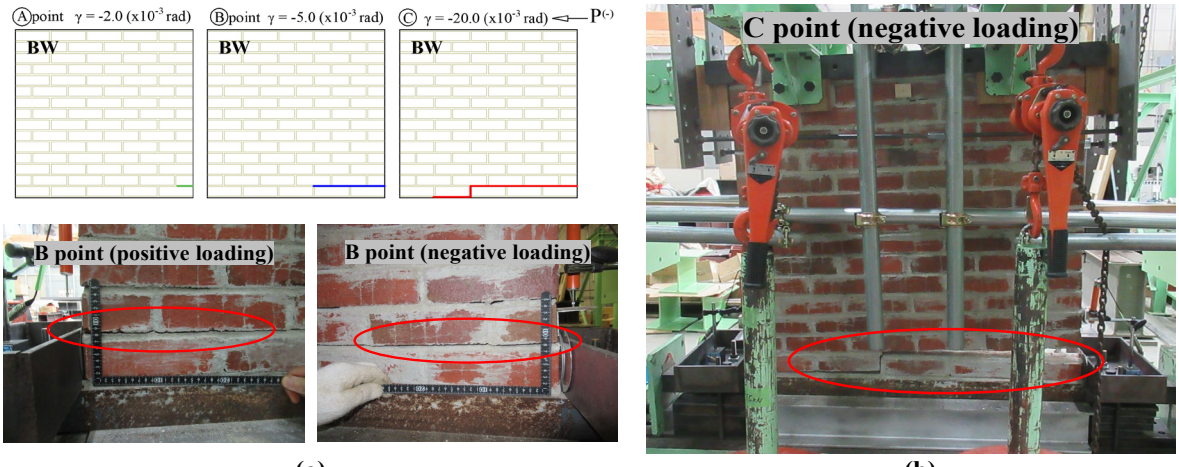

Figure 4.6. Failure and crack pattern of BW wall. (a) Scheme of the crack pattern and photo of crack at uplift (B point); (b) Photo of failure at maximum load.

The dominated failure of the BW wall is related to the in-plane flexural failure in Figure 4.6. As indicated as the "A" point in Figure 4.6a and Figure 4.5a, the initial crack was launched at the wall's bottom corner in the positive and negative loading. To increase the cyclic lateral load, the first crack was extending. The failure at the maximum load only occurred in the bottom part of the BW wall, and the vertical cracks were observed in the head-joint of the bottom brick layer in Figure 4.6b. "B" point in Figure 4.6a and Figure 4.5a marks the uplift at the BW wall. "C" point in Figure 4.6a and Figure 4.5a presents the failure at the maximum load. It is apparent from the failure photo and the vertical measurement results that the rocking failure has occurred.

4.4.3. BW-T wall

The load-drift angle curve of BW-T wall presents in Figure 4.5b,e,k,n and the drift angle in Figure 4.5b is calculated by the horizontal measurement. The first crack was observed in "A" point and the load at the first crack (the 4^{th} cycle) is 13.5 kN (-11.6 kN) in the positive (negative) loading. Table 4.4 presents drift at the first crack is 3.3 x 10^{-3} rad and 20.1 x 10^{-3} rad at the maximum load in both loading direction. The initial stiffness is 6.9 kN/mm (7.8 kN/mm) in the positive (negative) loading in Table 4.4. The load at the initial crack occurred 81.1% (73.7%) of the maximum load in the positive (negative) direction. During the horizontal load, the drift angle from the vertical measurement raised for the BW-T wall in Figure 4.5e. It is related that the bottom of the wall was lifted in the up direction due to the cyclic lateral load. In Figure 4.5k,n, the drift angle is the small value relying on the small displacements recorded under the positive and negative load. As the result of the diagonal measurement, it is assumed the BW-T wall is not deformed along the diagonal direction.

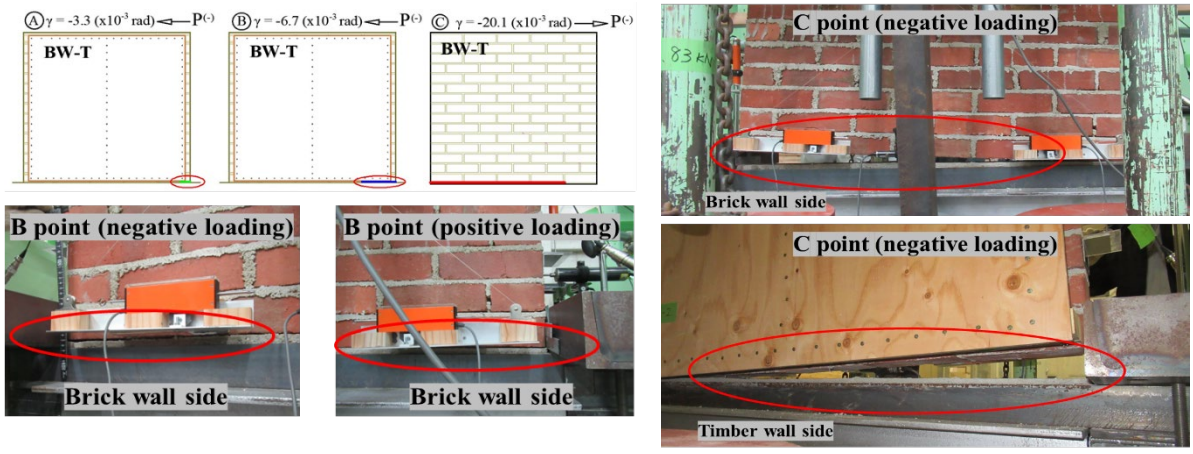

Figure 4.7. Failure and crack pattern of BW-T wall. (a) Scheme of crack pattern and photo of crack at uplift (B point); (b) Photo of failure at the maximum load.

Figure 4.7 shows the failure modes of BW-T wall. The first cracks started at the bottom of the wall corner, and the uplift occurred between the lowest mortar and the bottom of the lowest brick in Figure 4.7a. Failure caused by horizontal cycle loads indicated the in-plane flexural failure. There were no cracks in the brick walls, timber, connection, and the head-joint of the bottom brick layer. It shows that the head-joint of the bottom brick layer has good adhesion because of connecting the SPF lumber in the horizontal direction. The marked the point "B" is the uplift of the BW-T wall and the point "C" is the failure at maximum load in Figure 4.5b and Figure 4.7. The effect of the wooden wall did not increase the horizontal load of the BW-T wall during the cyclic load, but it retained the original shape of the brick wall. Therefore, the least strength part is damaged, which is the lowest part of the BW-T wall.

4.4.4. BW-TA wall

The initial crack of the BW-TA wall in the negative direction started at 4th cycle ("A" point and -16.2 kN) and at 5th cycle ("A" point and 16.4 kN) in the positive direction in Figure 4.5c. The maximum load is -24.6 kN ("C" point) in the negative direction and 22.5

kN (“D” point) in the positive direction. The uplift of BW-TA wall initiated at -21.3 kN in the 7th cycle (“B” point) for the negative direction. The load at the initial crack is 65.8 percent at the maximum load in the negative direction, and 72.8 percent in the positive direction. During the cyclic lateral load, the drift angle from the vertical measurement is -4.5 x 10^{-3} rad (-2.6 x 10^{-3} rad) in the maximum positive (negative) loading for the BW-TA wall in Figure 4.5f. It means that the bottom of the BW-TA wall was not uplifted until failure mode and the small displacements were recorded in the vertical direction. In Figure 4.5l,o, the drift angle increases under the positive and negative loading. As the result of the diagonal measurement, it is assumed the BW-TA wall is deformed along the diagonal direction from its original state.

Figure 4.8 presents the failure of the BW-TA wall, and the hold-down bolt connected the timber frame to the base of the experimental frame. Figure 4.8a presents the schematic crack pattern of the BW-TA wall at the “A” to “D” points as marked in Figure 4.5. Under the positive loading, the first crack started in the bottom right corner of the wall marked with the number “1” in Figure 4.8a and was observed in the 4th cycle (“A” point). Under the negative loading, the first crack appeared in the 5th cycle (“A” point) in the upper left corner of the wall marked with the number “1” in Figure 4.8a. Up to 7 cycles (“B” point), the crack in the middle of the wall formed at the bed-joint and the head-joint mortar’s intersections. At a horizontal load of 20.2 kN, the bottom right part of the wall is visibly uplifted. At a negative load of -21.3 kN, a slip occurred between the brick and mortar, marked with the number “1” in the upper left corner of the wall in Figure 4.8a.

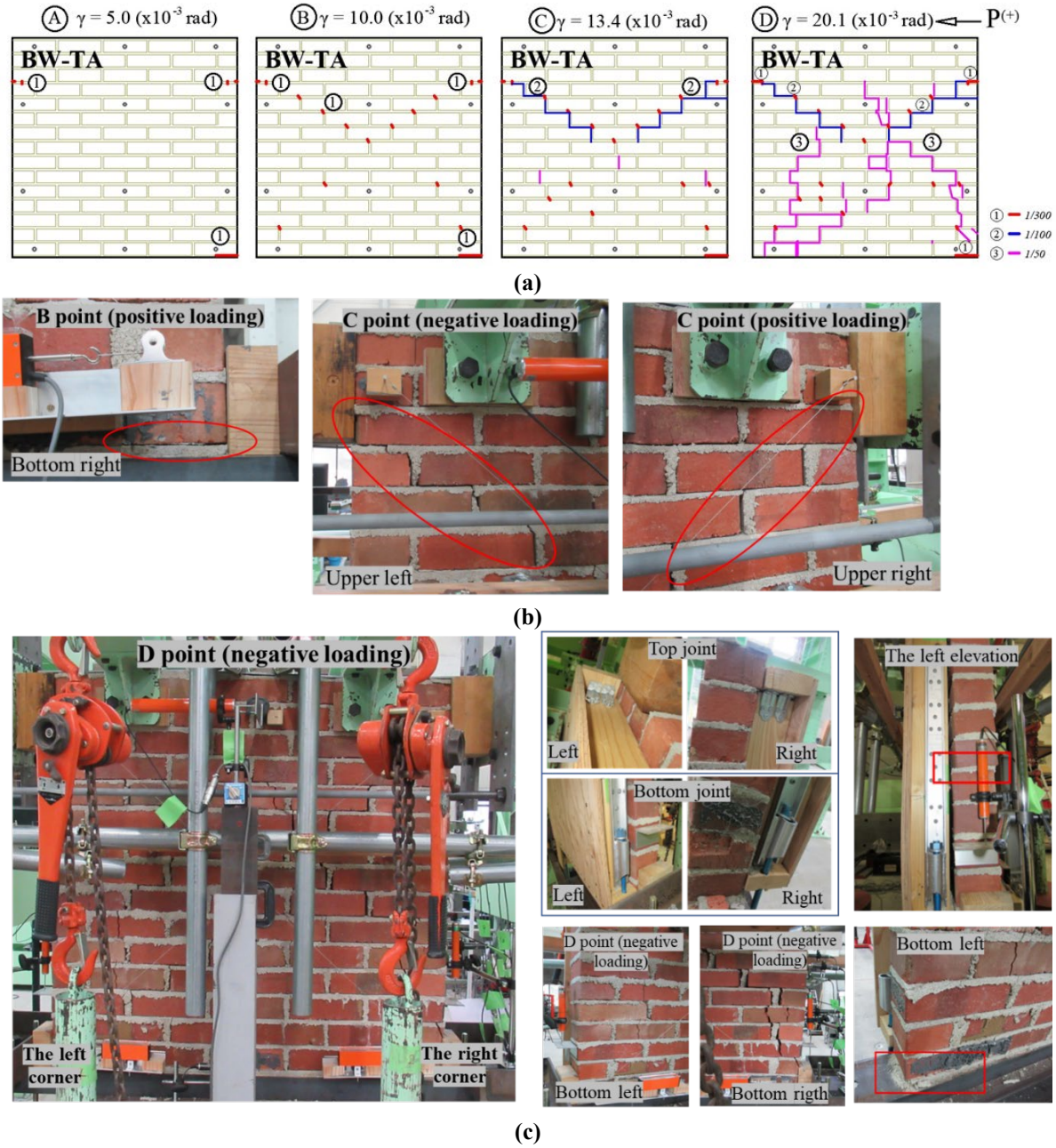

Figure 4.8. Failure and crack pattern of BW-TA wall. (a) Scheme of crack; (b) Failure photo at "C" point; (c) Failure photo at "D" point.

A slip occurred between the brick and mortar as marked by the number "1" in the upper left corner of the wall in Figure 4.8a. As the load increases, the vertical cracks are formed in the head-joint mortar, and the stepped diagonal cracks are shown as number "2" at the top part of the BW-TA wall. The stepped diagonal crack was the same for both positive and negative loads in the "C" point. When the ninth cycle ("D" point) began and the load

increased, vertical cracks were detected in the bricks. In the negative load, diagonal cracks dominated, and vertical cracks prevailed in the middle of the wall in the positive load. As shown in the crack pattern, the timber part and bolts have affected the wall damage. It indicates that the horizontal load was applied to the brick wall during a load until the initial crack appeared on the BW-TA wall. The vertical load from the moment was then received by the hold-down bolt of the BW-TA's timber wall. The results of the diagonal measurements in Figure 4.5l and o show that the timber wall can increase the deformation of the masonry part. The shear and tensile strength of the masonry part is much less than the timber wall. Therefore, the brick wall is considered damaged, while no damage or cracks occurred in the timber wall or the joint in Figure 4.8c. Figure 4.8c shows the lower base of the wall has moved from its original position, and the base of a brick wall is bent to the timber frame during in-plane horizontal loads.

To determine the drift between the brick wall and the timber frame, transducers were placed on the side of the BW-T and BW-TA walls in Figure 4.2d,g. The drift was calculated from the relative displacement divided by the transducer height, presented as a percentage in Figure 4.9. The relative displacement was determined by the difference between the horizontal displacement of the brick wall and the corresponding horizontal displacement of the timber frame. The relative displacement is assumed by the average value during the positive and negative loading. The transducers were placed on the side of the BW-T and BW-TA wall at three levels: top, middle, and bottom. Point "A" to "D" in Figure 4.9 indicates the failure modes as shown in Figure 4.5a,b,c. Figure 4.9 shows the relative displacement is almost non-existent until "A" point (4^{th} cycle). It is supposed that there is no deformation between the brick wall and the wooden wall until the first crack appears in

the BW-T and BW-TA walls. The measurement results indicated that the displacement in the brick wall was greater than the timber frame. The drift of the bottom part in Figure 4.9 is high for point "A" because the failure starts from the lower part of the BW-T and BW-T walls. For the BW-T wall, the failure was the lower part of the wall, and the drift at the “C” point is increased in Figure 4.9a. As for the BW-TA wall, failure mode was in-plane of the wall during the cyclic horizontal load. Therefore, the drift of the middle transducer height is greater than other at the “B” and “C” point in Figure 4.9b. The drift shows the low value in Figure 4.9 due to the high stiffness of the connection between the brick and wooden wall.

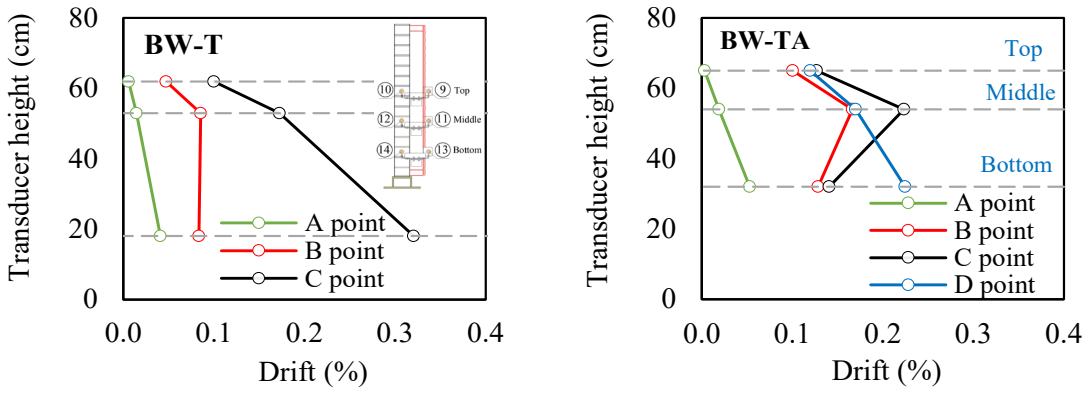

Figure 4.9. Relation between transducer height and drift of brick wall and timber part. (a) Result of BW-T wall; (b) Result of BW-TA wall.

The BW-TA wall’s timber frame is bolted to the base, and strain gauges (S1 and S2 in Figure 4.10) are attached in the middle of the bolts. Figure 4.10b illustrates the relation between the horizontal load and strain on the bolt, in the positive and negative loading. S-1 (black line) and S-2 (blue line) in Figure 4.10b are the names of the strains on the bolt, and S-1 is the strain placed on the left side of the BW-TA wall, and S-2 on the right side. In the positive loading, the value of S-1 strain increases, showing tensile properties, while the value of S-2 strain reduces. On the other hand, the strain values indicate the opposite state in negative loading.

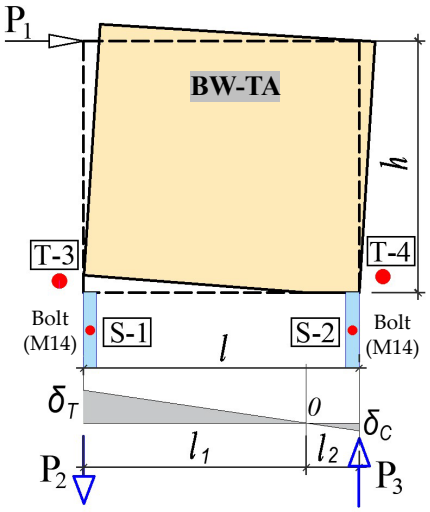

The tensile and compression axial load:

$$P_2 = E \cdot \varepsilon_1 \cdot A \qquad P_3 = E \cdot \varepsilon_2 \cdot A$$

The rotational equilibrium:

$$\sum M_0(P) = 0$$

$$\Downarrow$$

$$P_1 \cdot h - P_2 \cdot l_1 = P_0 \cdot h$$

The horizontal load on the brick wall:

$$P_0 = \frac{P_1 \cdot h - P_2 \cdot l_1}{h}$$

(a)

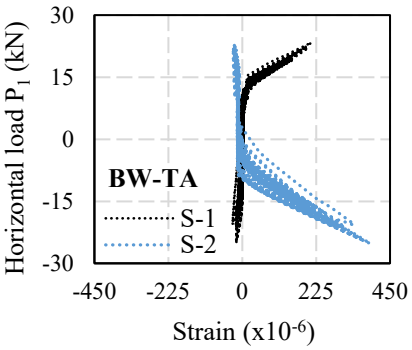

(b)

Figure 4.10. (a) Equilibrium condition of BW-TA wall; (b) Relation between horizontal load-strain on bolt.

Where: P_1 is the horizontal load recorded by the experiment; P_2 is the tensile load on the bolt during the positive loading; P_3 is the compression load on the bolt during the positive loading; E is the elastic modulus of the bolt; ε_1 (ε_2) is the strain value recorded by *S-1* (*S-2*) strain gauge; A is the cross-sectional area of the bolt M14; l_1 is the tensile length of the wall; l_2 is the compression length of the wall; P_0 is the horizontal load on the brick wall without the hold-down bolt; l is the length of the wall; h is the height of the wall.

Knowing the strain in the bolts makes it possible to determine the tensile and compression load. The tensile axial load (P_2 in Figure 4.10a) of a bolt is proportional to the elastic modulus (E), tensile strain (ε_1), and cross-sectional area (A). The axial compression load (P_3 in Figure 4.10a) is determined in the same way. In Figure 4.10a, the tensile displacement (δ_T) of the BW-TA wall was measured at transducer T-3 and the compressive displacement (δ_C) was measured at transducer T-4 under the positive loading. Point "0"

touches the horizontal axis when the tensile and compression displacement are connected in a straight line. The rotational equilibrium can be written using the "0" point. The compression length (l_2) is difficult to quantify for calculation simplification, and the compressive axial load is neglected in the calculation. We may calculate the horizontal load on the wall without the hold-down bolt using the rotational equilibrium conditions (P_0). It means that the experimental results of the BW-TA wall can be used to calculate the horizontal load acting on a brick wall

4.5. Discussion

Figure 4.11 presents the comparison result of the wall specimens and the curve is created by the envelope curve. Figure 4.11a is the load-drift angle envelope curve under the positive loading. Figure 4.11a is the load-drift angle envelope curve under the negative loading, and the sign of the negative load and drift angle is presented by the positive. Figure 4.11c is the mean envelope curve calculated by the average between the positive and negative values. A load-drift angle diagram created by P_0 is shown in Figure 4.11, denoted by BW-TA-P0. The result of the BW-TA-P0 is almost the same compared with BW and BW-T wall in the positive loading, but a little lower value is shown in the negative loading. Also, the BW and BW-T wall results are similar to each other. The initial stiffness of the BW-T and BW-TA wall in Table 4.4 reduced from the initial stiffness of the BW wall. It is related to the impact force when the plywood is fixed to the wall with nails. The horizontal load on the timber wall of the BW-TA wall can be obtained by the difference between BW-TA and BW-TA-P0 diagrams as illustrated in Figure 4.11. The maximum horizontal load of the timber wall is 4.4 kN (12.9 kN) in the positive (negative loading), and the mean value in negative and positive loading is 8.2 kN.

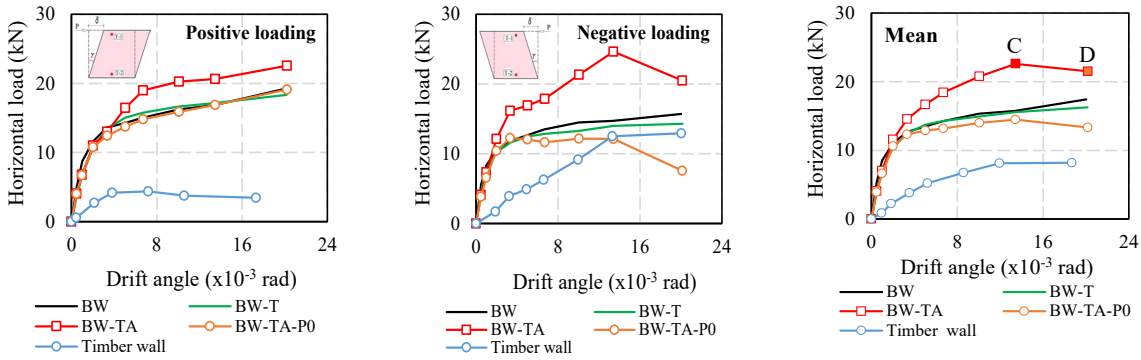

Figure 4.11. Comparison envelope curve of horizontal load and drift angle for walls (BW. BW-T, BW-TA, BW-TA-P0, and timber wall). (a) Result of positive loading; (b) Result of negative loading; (c) Mean result.

As shown in Figure 4.11, the horizontal load of the BW-TA wall is 14.8% (36.2%) higher than the BW wall in the positive (negative) loading, and it is 22% greater in the mean. The combined effect of the timber wall and the hold-down anchor started when the flexural crack appeared on the BW-TA wall. The lateral load and stiffness of the timber wall in Figure 4.11 are low, but it is possible to improve the shear deformation of the unreinforced brick wall. Figure 4.5d,f present the result of the vertical measurement of BW and BW-TA walls. The drift angle of BW wall in Figure 4.5d is same as the horizontal measurement. Therefore, it can be determined how many times the vertical displacement of the BW wall decreases after strengthening in Figure 4.12a. The ratio of the BW and BW-TA wall's drift angle estimated by the vertical measurement is 4.6 at "C" point (the mean maximum load in Figure 4.11c). Figure 4.12b,c show the drift angle obtained from the diagonal transducers T5 and T6 of the BW-T and BW-TA walls. The result of the diagonal measurement of the BW-T wall was low value. It was assumed the BW-T wall did not deform in the diagonal direction. Therefore, the drift angle of the BW-T and BW-TA walls were compared and it means the drift angle of the BW-T wall can increase 4.8 times at "C" point in Figure 4.12b,c. It is assumed that the shear deformation of the BW wall can be improved by the strengthening

technique using the timber material. The experimental result of the BW-TA wall displays that the initial stiffness did not increase after strengthening. It is considered that the brick wall received the horizontal load in the initial cyclic loading.

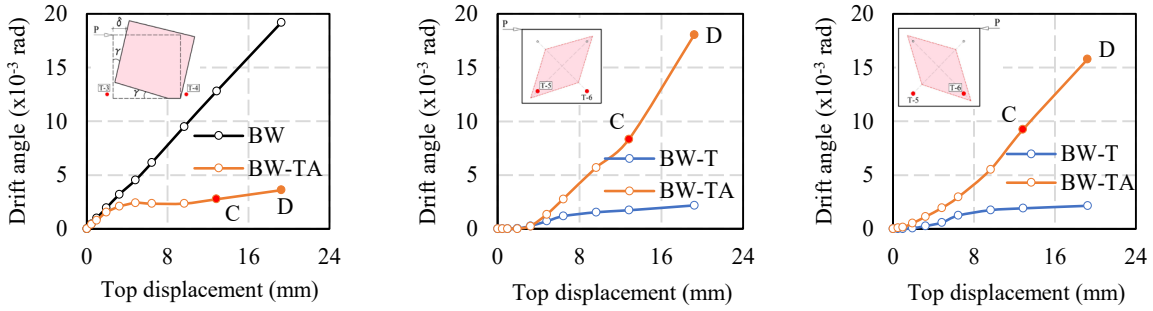

Figure 4.12. Drift angle and top displacement relation. (a) Vertical measurement of BW and BW-TA walls; (b) Diagonal measurement by T5 of BW-T and BW-TA walls; (c) Diagonal measurement by T6 of BW-T and BW-TA walls.

4.6. Conclusions

The study carried out the strengthening method of the single-leaf brick masonry wall using timber to improve the in-plane shear strength under the cyclic horizontal load. Three types of walls were tested, including BW wall (the brick wall), BW-T wall (the strengthened brick wall with timber) and BW-TA wall (the strengthened brick wall with timber connecting by hold-down anchor to the base). During the cyclic horizontal load, three different position measurements such as horizontal, vertical, and diagonal directions were recorded on all walls. The shear deformation was determined and compared by the horizontal, vertical, and diagonal measurements.

Maximum horizontal load of BW and BW-T wall are almost same value. For BW-TA wall, horizontal load increased around 20 percent compared with BW wall's result. Three wall's initial stiffness shows same value. Drift angle of BW-TA defined by diagonal measurement was increased by 4.8 at maximum load compared with BW-T wall. BW and BW-T walls presented same failure mode which is rocking failure. Failure mode of BW-TA wall showed diagonal compression failure.

CHAPTER V.

PREDICTION OF UNREINFORCED AND REINFORCED BRICK WALLS

5.1. Introduction

This chapter includes the prediction analysis of the unreinforced brick masonry wall (URM) and the reinforced brick masonry wall with timber frame and plywood panel. The required material properties were determined in Chapter II. The in-plane shear capacity of the unreinforced brick wall was calculated by the simple theories, and masonry wall was assumed by elastic and homogeneous.

5.2. Unreinforced brick masonry wall (BW wall)

Due to lateral loads, sliding, diagonal and flexural failures shown in Figure 5.1 occur in the unreinforced masonry walls for the in-plane direction. Sliding and diagonal tensile failure are related to the shear resistance, and flexural failure is caused by the bending moment. To predict the shear strength capacity of the unreinforced masonry wall, the effective stiffness, shear capacity and drift capacity of the wall are required [48]. In this study, the load-drift angle relationship is predicted by the bi-linear curve. The corresponding material properties were obtained by the experiment. The in-plane shear capacity of the unreinforced brick wall was calculated by the simple theories, and masonry wall was assumed by elastic and homogeneous.

The prediction horizontal load formulas present in Table 5.1. The theory of bed-joint sliding failure showing formula (5.1) in Table 5.1 is based on the well-known failure criterion Morh-Coulumb. The Morh-Coulumb formula contains parameters that express the nonlinear properties of the masonry wall, including the adhesion strength and the friction coefficient. The nonlinear material properties such as the adhesion strength and frictional coefficient were obtained by the pre-compression shear test in this study [35]. The horizontal load causing the sliding failure was calculated from the cross-sectional area of the wall. The diagonal failure prediction is calculated by the formula (5.2) in Table 5.1 and the failure occurs from a combination of the normal and shear stress on the wall [49].

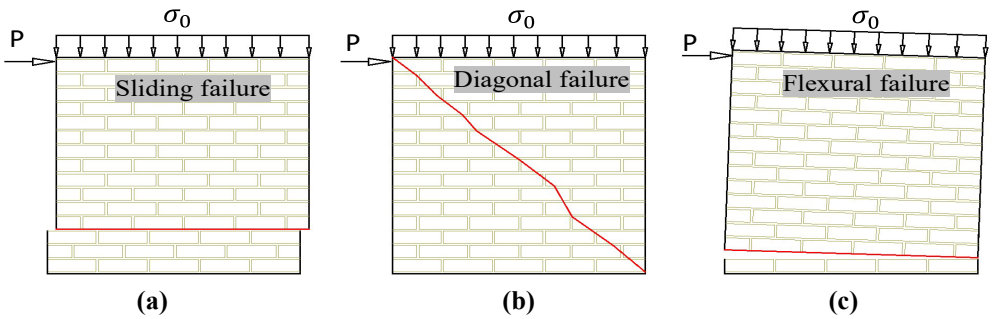

Figure 5.1. In-plane failure modes. (a) Sliding failure; (b) Diagonal compression failure; (c) Flexural failure.

In that case, the principal tensile strength in the cross-section of the wall exceeds the diagonal tensile strength of the masonry wall [10,50]. Diagonal cracks can be the stepped and straight modes in the masonry wall [12]. The tensile strength of a masonry wall is 3 to 9 percent of the compressive strength of a masonry wall obtained from the experiment [51]. The flexural failure prediction is shown in formula (5.3) of Table 5.1. Due to the bending moment, cracks are formed in the tensile part of the wall. The crack increases with increasing horizontal load while the length of the compressed wall decreases and the compressed area received the most stress concentration [51]. The determination of flexural capacity depends on parameters such as the pre-compression stress, the thickness of the wall,

the length of the wall, and compressive strength of the masonry. The horizontal load from the bending moment is defined by comparing the height of the wall and the boundary conditions. The minimum horizontal load of sliding failure, diagonal failure, and flexural failure is assumed by the predicted failure load at the ultimate state ($P_{BW,U}$).

Table 5.1. Prediction formula of horizontal load

№	Failure	Shear and flexural capacity	Shear load
(5.1)	Sliding	$\tau = c + \mu \cdot \sigma_0$	$P_s = \tau \cdot t \cdot l$
(5.2)	Diagonal	$\tau_t = \frac{f_t}{b}\sqrt{\frac{\sigma_0}{f_t} + 1}$	$P_t = \tau_t \cdot t \cdot l$
(5.3)	Flexural	$M_u = \frac{\sigma_0 \cdot t \cdot l^2}{2}\left(1 - \frac{\sigma_0}{f}\right)$	$P_f = \frac{M_u}{\alpha \cdot h}$

Where; τ–shear strength (N/mm^2); c–the adhesion strength (N/mm^2); μ–the frictional coefficient; t–thickness of wall (mm); f_t–tensile strength of wall (N/mm^2); b–shear stress distribution factor, depending on the geometry of the wall (h/l=1, b=1); σ_0–the pre-compression stress (N/mm^2); τ_t–shear strength from diagonal tensile strength (N/mm^2) ; l–length of the wall (mm); M_u–the ultimate bending moment (Nmm); f–compression strength of the masonry (N/mm^2); α–the boundary condition (α =1 the cantilever and α =0.5 the fixed–ended); h–height of the wall (mm).

Initial stiffness in equation (5.4) can be defined by the Timoshenko beam theory assuming the lateral displacement obtained from the shear and flexural strength [50,52]. The ratio between shear and elastic modulus (G/E) is 0.05 for the 0.2 N/mm^2 pre-compression stress by experiment in Table 2.8. The BW wall's elastic modulus was determined during the pre-compression loading presented in Table 4.3.

$$K_e = \frac{H}{d} = \frac{G \cdot A_w}{1.2h\left[1 + \alpha' \frac{G}{E}\left(\frac{h}{l}\right)^2\right]} \tag{5.4}$$

In the prediction calculation, the near-collapse drift was considered according to EN 1998-3 [52,53]. Table 5.2 shows the drift occurring in the shear and flexural failure.

Table 5.2. Near collapse of drift (EN 1998-3)

Failure	Near collapse drift
Shear	$\frac{4}{3} \cdot 0.4\%$
Flexural	$\frac{4}{3} \cdot 0.8\% \cdot \left(\frac{h}{l}\right)$

5.3. Reinforced brick masonry wall with timber (BW-TA wall)

The shear capacity of the reinforced brick wall ($P_{BW\text{-}TA}$) is the sum of the horizontal load from the URM wall (P_{BW}) and the timber wall (P_{TA}).

$$P_{BW-TA} = P_{BW} + P_{TA}$$

Timber wall consists of the lumber frame, plywood panel and CN65 nails in this study. The horizontal load called the racking load acts on the nailed wall. There are the literature review [54,55] to predict the racking strength. In this study, the prediction calculation are used by the model Kamiya and Inayama Murakami [56] in Figure 5.2. This prediction model presents the non-linear characteristic of the nailed wall. The model is assumed by the rigid body, and the rotational angles (θx and θy) are in the *X* and *Y* axis when the pin-joint frame deforms into a parallelogram in Figure 5.2b. The rotational angles are defined by equilibrium condition of the moments in the X and Y axis (M_x=M_y) in Figure 5.2b.

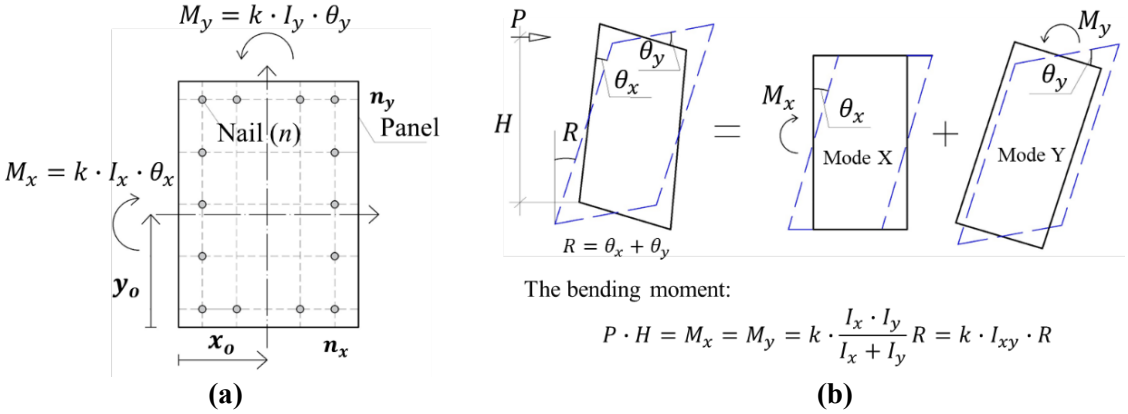

Figure 5.2. Model of Kamiya and Inayama Murakami. (a) Coordinates of nails and moments acting on wall; (b) Deformation shape by rotation.

Under the influence of the horizontal load (*P*) acting on the wall, the moment of resistance applies to each nail in the X and Y directions. Therefore, the moment ($P \cdot H = M_x = M_y$) from the external and internal forces is assumed to be equal based on the energy method in Figure 5.2b. The model of the Kamiya and Inayama Murakami [56] consists of

the elastic stiffness, the yield moment, the plasticity ratio, and the ultimate moment in Table 5.3. The predicted yield displacement is determined by the ratio between the yield horizontal load and elastic stiffness. The predicted ultimate displacement is the yield displacement multiplied by the plasticity ratio shown in Table 5.3.

Table 5.3. Parameter of Kamiya and Inayama Murakami model.

The parameter	The formula
The yield moment	$M_y = \Delta P \cdot Z_{xy} \cdot A_w$
The ultimate moment	$M_u = C_{xy} \cdot M_y$
Elastic stiffness	$k_0 = \frac{A_w}{\frac{1}{I_{xy} \cdot k} + \frac{1}{G_B \cdot t}}$
The plasticity ratio	$\mu = \frac{\delta_u \cdot G_B \cdot t + \delta_v \cdot I_{xy} \cdot k}{\delta_v (G_B \cdot t + I_{xy} \cdot k)}$

Where: ΔP is the yield horizontal load (*kN*); Z_{xy} is the nail arrangement coefficient per unit area (cm/cm^2); A_w is the cross-sectional area of the sheathing material (cm^2); C_{xy} is the nail arrangement ratio of yield and ultimate; M_y is the yield moment (*kNcm*); M_u is the ultimate moment (kNcm); δ_u is the ultimate shear displacement of one nail (*cm*); G_B is the shear modulus of the plywood panel (kN/cm^2); t is thickness of the plywood panel (*cm*); δ_v is the yield shear displacement of the one nail (*cm*); I_{xy} is the second moment of area of the nails (cm^2); k is the shear stiffness of one nail (*kN/cm*).

Table 5.4. Shear values per CN65 nail

Joint	Fastener type	k (kN/cm)	δ_v (cm)	δ_u (cm)	ΔP (kN)	G_B (kN/cm^2)
Timber to 12 mm plywood	CN65 nail	8.26	0.25	2.17	2.05	40

The shear behavior of the nailed joint is the perfect elasto-plasticity and the shear values per CN65 nail are taken from the reference experimental results in Table 5.4 [57]. The prediction calculation of the timber wall is compared with the experimental result as shown in Figure 5.6a. The yield and ultimate of the prediction timber is much higher than the experimental wall. However, the initial stiffness of timber wall is 1.7 kN/mm for the experiment and 2.6 kN/mm for the prediction in Table 5.5. The prediction yield load of the nailed wall ($P_{y,T}$) indicates until the nails are distorted. The test of the BW-TA wall did not reveal any damage to the wooden walls or nail joints during the test. The load-drift angle curve of the timber wall shown in Figure 5.3a is determined from the load-drift angle curve

of the BW-TA wall test. Therefore, it is assumed that the brick wall has already been damaged while the nail joint was not deformed.

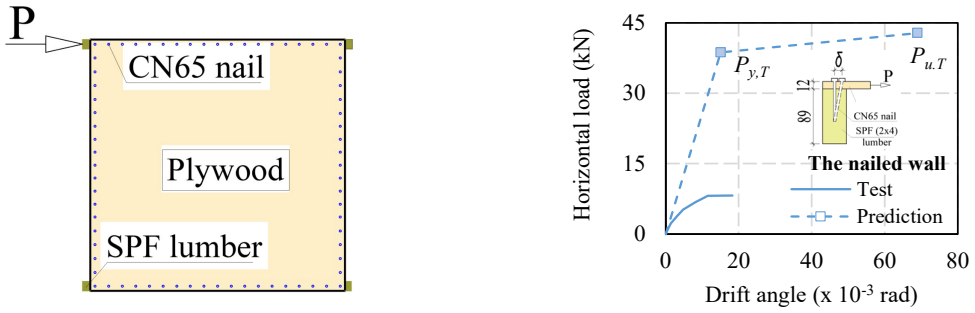

(a) **(b)**

Figure 5.3. (a) Scheme of timber wall; (b) Comparison results of experimental and prediction load-drift curve

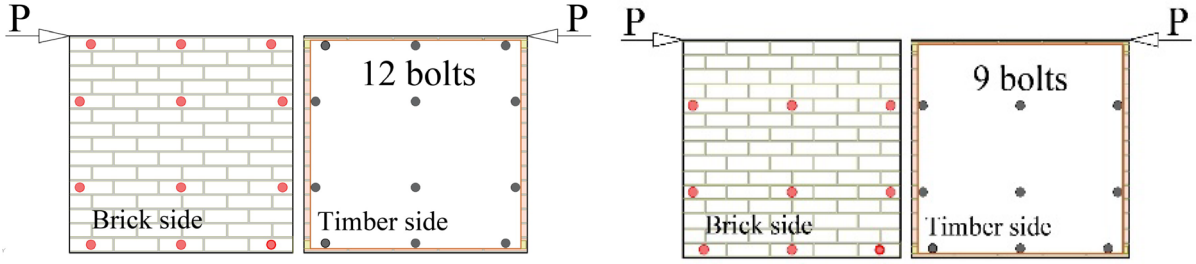

(a) **(b)**

Figure 5.4. Prediction model of BW-TA wall. (a) Prediction-1 (BW-TA wall with 12 bolts); (b) Prediction-2 (BW-TA wall with 9 bolts).

Nails were used to fasten the plywood to the lumber frame. Similarly, the M12 bolts with the chemical epoxy were employed to attach the wood to the brick wall. The materials used in these cases are different, but the overall structures of the walls are the same. Connection calculations are not only important for the timber structure but also it is important for a joint calculation between timber and brick wall. In this study, Kamiya and Inayama Murakami model was used in the prediction estimation to define the load-drift curve of the BW-TA wall. The BW-TA wall has 12 bolts (the prediction-1) connected to wood and brick wall in Figure 5.2a, and the horizontal load is applied to the top corner of the wall. Figure 5.2b shows the prediction-2 result and the BW-TA wall is assumed to have 9 bolts. As shown in the failure scheme of the BW-TA wall, the crack pattern did not appear on the top three of

the brick layers. In the prediction-2, the effect of the upper three bolts on the masonry wall was not considered, and the panel size did not change because the effect of the upper nail of the timber wall is considered to be greater under the horizontal load.

5.4. Discussion

5.4.1. BW wall

The bi-linear predicted curves are compared with the experimental results, as illustrated in Figure 5.5. The flexural capacity is the minimum value of the predicted horizontal load in this study. As shown in Figure 5.5, the predicted horizontal load ($P_{BW,U}$) is 12.2 kN and the load at the initial crack in the experiment (P_{cr}) is 11 kN. The predicted load represents the value after the first crack appeared on the BW wall. The unreinforced masonry wall has brittle behavior under the cyclic load, and the BW wall was damaged along the initial crack when the pre-compression stress was low for our study. The assumption is considered to be reasonable.

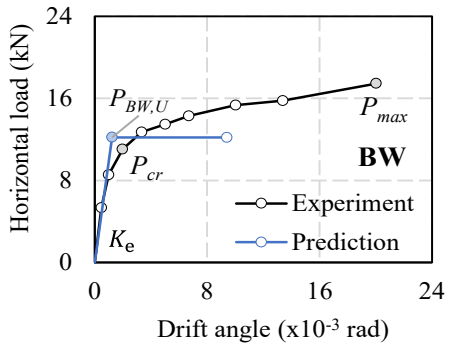

Figure 5.5. Comparison curve of prediction and experimental result

The initial stiffness obtained from formula (14) and the experiment present almost the same value such as 10.21 kN/mm for formula (14) and 8.9 kN/mm for the test. The initial stiffness of the experiment was determined by the horizontal load of the second cycle and the corresponding displacement. The slope of the initial stiffness depends on the shear

modulus (G). Material tests in this study have shown that the G/E ratio is the low value at the low vertical loads in Table 2.8. For the prediction deformation capacity, the drift is estimated from the flexural failure shown in Table 5.2. After the first cracks appeared in the experiment, the vertical displacement in the bottom corners of the BW wall increased. It indicates that the wall is already in a state of failure mode. Therefore, it is considered appropriate to limit the expected drift.

5.4.2. BW-TA wall

Table 3.6 shows the required material parameter to calculate the masonry wall with timber by the Kamiya and Inayama Murakami model. The slip modulus (k), the ductility ratio and the yield load (ΔP) of the brick and timber joint were taken from the single shear test and the shear modulus of the timber wall ($G_B = 17.1\ kN/cm^2$) is estimated from the BW-TA wall's experimental result. The comparison results of the experimental and prediction load-drift angle curve is shown in Figure 5.6. Figure 5.6a presents the load-drift angle curve between the experimental and prediction-1. Figure 5.6b illustrates the load-drift angle curve of the experimental and prediction-2.

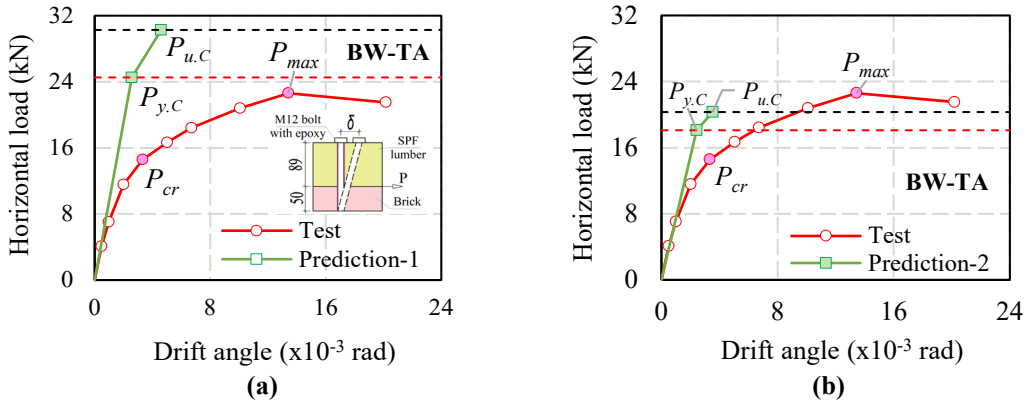

Figure 5.6. Comparison results of experimental and prediction load-drift curve. (a) Prediction-1 of the BW-TA wall; (b) Prediction-2 of BW-TA wall.

Table 5.5 shows the comparison result of the experimental and prediction calculation of the BW-TA wall. The experimental yield load is assumed by the load at the initial crack on the BW-TA wall and the ultimate load is 90 percent of the maximum load in Table 5.5. The initial stiffness of the prediction-1 is 21 percent greater than the experimental stiffness. But the yield horizontal load of the prediction-1 is 1.67 times higher than test value and the ultimate horizontal load is 33 percent greater than the experimental value. As for the result of the prediction-2, the initial stiffness is 14.7% greater than the test value and the ultimate load are almost the same as the experimental value. The yield horizontal load is 1.23 times greater than the experimental value. The result of the prediction-2 can give a reasonable value of the initial stiffness and the ultimate horizontal load compared with the prediction-1. The yield load is assumed that it is related to the solid body model. It means Kamiya and Inayama Murakami model indicates until the joint is deformed and not considered brick-mortar sliding. The BW-TA wall failure showed that vertical cracks appeared on the bricks when the horizontal load was reaching its maximum load. The BW-TA wall test ended with brick cracks. The ductility ratio in the prediction calculation could not show a suitable value. Low ultimate displacement is presented for BW-TA wall in Figure 5.6. In that case, the brick-mortar slip effect did not consider in the prediction calculation.

Table 5.5. Comparison results of horizontal load and stiffness of walls

Wall type	**State**	**Drift angle**		**Horizontal load**		**Stiffness**
		Yield	**Ultimate**	**Yield**	**Ultimate**	
		(x 10^{-3})		*(kN)*		*(kN/mm)*
Timber	Test	-	18.3	-	7.38	1.7
	Prediction	15.1	68.9	38.7	42.8	2.6
BW-TA	Test	3.3	20.2	14.6	20.3	8.7
	Prediction-1	2.6	4.6	24.5	30.3	9.5
	Prediction-2	2.4	3.5	18.1	20.3	8.8

5.5. Conclusions

In this chapter, the predictions of unreinforced and reinforced brick walls were estimated and compared with the experimental results.

The experimental result of the BW wall is compared with the bi-linear prediction curve. The prediction estimation of the BW wall can give the reasonable initial stiffness and the ultimate horizontal load.

The proposed theoretical method (KIM model) has shown good results in determining the initial stiffness and the ultimate horizontal load. The prediction-1 initial stiffness is 21% greater than the experimental stiffness. However, the prediction-1 yield horizontal load is 1.67 times higher than the test value, and the ultimate horizontal load is 33% greater than the experimental value. The prediction-2 result shows that the initial stiffness is 14.7% greater than the test value and the ultimate load is almost the same as the experimental value. The experimental value is 1.23 times greater than the yield horizontal load. When compared to prediction-1, the result of prediction-2 can give a reasonable value for the initial stiffness and ultimate horizontal load.

CHAPTER VI.

CONCLUSIONS

Chapter II

Material properties of brick, cement mortar, small masonry specimen, lumber, bolt, and epoxy resin were used in the predictions of pull-out and shear strength of connection, the unreinforced and reinforced brick walls. Brick used in experiment has high quality, high burning degree, no weathering behavior, and low pores in bricks. The flexural strength is 3.9 N/mm^2 and the compression strength is 31.4 N/mm^2. The compression strength of cement mortar is 10.9 N/mm^2 at 6 months. Frictional coefficient of small masonry specimen is 0.68 and initial shear strength is 0.41 N/mm^2. The compression strength of small masonry specimen is 14.4 N/mm^2 and the elastic modulus is 1202.9 N/mm^2. G/E ratio of masonry specimen is 0.05 for the 0.2 N/mm^2 pre-compression shear test.

Chapter III

Strength properties of the connection between brick and timber were determined, and the result was compared with experimental and prediction estimation. The prediction formulas of the pullout and shear strength could give a suitable result. The pullout strength depends on the bolt diameter. The predicted failure load illustrates the combined cone–bond failure load. The experimental failure mode is also the combined cone–bond failure until the load reaches the maximum value. Then splitting failure occurs when the maximum load gradually decreases. For the single brick, the probability of steel and cone failure occurring is small.

The yield shear strength of the composite specimen (brick-to-wood) on the chemical anchor is reasonable to expect in the European Yield Theory (EYT). However, it is complex to determine the failure mode. When it comes to increasing the strength of masonry construction, the A12 type is recommended since it provides excellent strength and stiffness.

Chapter IV

In Chapter IV, three types of walls were tested, including BW wall (the brick wall), BW-T wall (the strengthened brick wall with timber) and BW-TA wall (the strengthened brick wall with timber connecting by hold-down anchor to the base). During the cyclic horizontal load, three different position measurements such as horizontal, vertical, and diagonal directions were recorded on all walls. The shear deformation was determined and compared by the horizontal, vertical, and diagonal measurements.

Maximum horizontal load of BW and BW-T wall are almost same value. For BW-TA wall, horizontal load increased around 20 percent compared with BW wall's result. Three wall's initial stiffness shows same value. Drift angle of BW-TA defined by diagonal measurement was increased by 4.8 at maximum load compared with BW-T wall. BW and BW-T walls presented same failure mode which is rocking failure. Failure mode of BW-TA wall showed diagonal compression failure.

Chapter V

The experimental results of the walls (BW and BW-TA walls) were compared with the proposed analytical method. The experimental result of the BW wall is compared with the bi-linear prediction curve. The prediction estimation of the BW wall can give the reasonable initial stiffness and the ultimate horizontal load.

The proposed theoretical method (Kamiya and Inayama Murakami model) has shown good results in determining the initial stiffness and the ultimate horizontal load of the BW-TA wall. The prediction-1 initial stiffness is 21% greater than the experimental stiffness. However, the prediction-1 yield horizontal load is 1.67 times higher than the test value, and the ultimate horizontal load is 33% greater than the experimental value. The prediction-2 result shows that the initial stiffness is 14.7% greater than the test value and the ultimate load is almost the same as the experimental value. The experimental value is 1.23 times greater than the yield horizontal load. When compared to prediction-1, the result of prediction-2 can give a reasonable value for the initial stiffness and ultimate horizontal load.

The advantage of the proposed strengthening technique is the light weight, cost-effective and easy to assemble. Timber with the hold-down anchor is an effective retrofitting method to enhance the in-plane shear strength and the shear deformation of the masonry wall.

Limitation

Pull-out and Shear strength - The limitation is that the substrate material is only brick, and the bolt depth is shallow. The number of specimens is three. However, if high deviations are shown, the number of tests should be increased, and the specimens should be well prepared.

Wall behavior - The pre-compression stress and the number of specimens need to increase. In the prediction calculation, it is necessary to approximate the values of the yield load and the in-elastic stiffness.

Future study

This research will define the target strength of the reinforced brick wall with timber material.

This study will also contribute to the numerical analysis of the reinforced brick wall with timber.

The proposed retrofitting method will be installed in the existing unreinforced brick buildings.

The strengthening method of out-of-plane behavior in the masonry building will be proposed and carried out by the experimental and theoretical methods.

References

1. Rahman, A.; Ueda, T. In-Plane Shear Performance of Masonry Walls after Strengthening by Two Different FRPs. *J. Compos. Constr.* **2016**, *20*, 04016019, doi:10.1061/(ASCE)CC.1943-5614.0000661.
2. Konthesingha, K.M.C.; Masia, M.J.; Petersen, R.B.; Page, A.W. Experimental Evaluation of Static Cyclic In-Plane Shear Behavior of Unreinforced Masonry Walls Strengthened with NSM FRP Strips. *J. Compos. Constr.* **2015**, *19*, 04014055, doi:10.1061/(ASCE)CC.1943-5614.0000512.
3. Banerjee, S.; Nayak, S.; Das, S. Seismic Performance Enhancement of Masonry Building Models Strengthened with the Cost-Effective Materials under Bi-Directional Excitation. *Engineering Structures* **2021**, *242*, 112516, doi:10.1016/j.engstruct.2021.112516.
4. Giaretton, M.; Dizhur, D.; Garbin, E.; Ingham, J.M.; da Porto, F. In-Plane Strengthening of Clay Brick and Block Masonry Walls Using Textile-Reinforced Mortar. *J. Compos. Constr.* **2018**, *22*, 04018028, doi:10.1061/(ASCE)CC.1943-5614.0000866.
5. Bilgin, H.; Shkodrani, N.; Hysenlliu, M.; Baytan Ozmen, H.; Isik, E.; Harirchian, E. Damage and Performance Evaluation of Masonry Buildings Constructed in 1970s during the 2019 Albania Earthquakes. *Engineering Failure Analysis* **2022**, *131*, 105824, doi:10.1016/j.engfailanal.2021.105824.
6. Vlachakis, G.; Vlachaki, E.; Lourenço, P.B. Learning from Failure: Damage and Failure of Masonry Structures, after the 2017 Lesvos Earthquake (Greece). *Engineering Failure Analysis* **2020**, *117*, 104803, doi:10.1016/j.engfailanal.2020.104803.
7. Stepinac, M.; Lourenço, P.B.; Atalić, J.; Kišiček, T.; Uroš, M.; Baniček, M.; Šavor Novak, M. Damage Classification of Residential Buildings in Historical Downtown after the ML5.5 Earthquake in Zagreb, Croatia in 2020. *International Journal of Disaster Risk Reduction* **2021**, *56*, 102140, doi:10.1016/j.ijdrr.2021.102140.
8. Mazumder, R.K.; Rana, S.; Salman, A.M. First Level Seismic Risk Assessment of Old Unreinforced Masonry (URM) Using Fuzzy Synthetic Evaluation. *Journal of Building Engineering* **2021**, *44*, 103162, doi:10.1016/j.jobe.2021.103162.
9. Takagi, J.; Wada, A. Higher Performance Seismic Structures for Advanced Cities and Societies. *Engineering* **2019**, *5*, 184–189, doi:10.1016/j.eng.2018.11.023.
10. Tomaževič, M. Shear Resistance of Masonry Walls and Eurocode 6: Shear versus Tensile Strength of Masonry. *Mater Struct* **2009**, *42*, 889–907, doi:10.1617/s11527-008-9430-6.
11. Zhang, Y.; Lin, X.; Wang, T.; Skalomenos, K. Seismic Behavior of Masonry Walls Strengthened by Precast Reinforced Concrete Panels with Different Connection Details. *Engineering Structures* **2021**, *242*, 112597, doi:10.1016/j.engstruct.2021.112597.
12. Kišiček, T.; Stepinac, M.; Renić, T.; Hafner, I.; Lulić, L. Strengthening of Masonry Walls with FRP or TRM. *JCE* **2020**, *72*, 937–953, doi:10.14256/JCE.2983.2020.
13. Yao, X.; Guo, Z.-X.; Basha, S.H.; Huang, Q. Innovative Seismic Strengthening of Historic Masonry Walls Using Polymer Mortar and Steel Strips. *Engineering Structures* **2021**, *228*, 111507, doi:10.1016/j.engstruct.2020.111507.
14. Wang, C.; Sarhosis, V.; Nikitas, N. Strengthening/Retrofitting Techniques on Unreinforced Masonry Structure/Element Subjected to Seismic Loads: A Literature Review. *TOBCTJ* **2018**, *12*, 251–268, doi:10.2174/1874836801812010251.

15. Guerrini, G.; Damiani, N.; Miglietta, M.; Graziotti, F. Cyclic Response of Masonry Piers Retrofitted with Timber Frames and Boards. *Proceedings of the Institution of Civil Engineers - Structures and Buildings* **2021**, *174*, 372–388, doi:10.1680/jstbu.19.00134.
16. Dizhur, D.; Giaretton, M.; Giongo, I.; Ingham, J. Seismic Retrofit of Masonry Walls Using Timber Strong-Backs. **2017**, *30*, 30–44.
17. Miglietta, M.; Damiani, N.; Guerrini, G.; Graziotti, F. Full-scale Shake-table Tests on Two Unreinforced Masonry Cavity-wall Buildings: Effect of an Innovative Timber Retrofit. *Bull Earthquake Eng* **2021**, *19*, 2561–2596, doi:10.1007/s10518-021-01057-5.
18. Giongo, I.; Rizzi, E.; Riccadonna, D.; Piazza, M. On-Site Testing of Masonry Shear Walls Strengthened with Timber Panels. *Proceedings of the Institution of Civil Engineers - Structures and Buildings* **2021**, *174*, 389–402, doi:10.1680/jstbu.19.00179.
19. Iuorio, O.; Dauda, J.A. Retrofitting Masonry Walls against Out-Of-Plane Loading with Timber Based Panels. *Applied Sciences* **2021**, *11*, 5443, doi:10.3390/app11125443.
20. Sustersic, I.; Dujic, B. Seismic Strengthening of Existing Concrete and Masonry Buildings with Crosslam Timber Panels. In *Materials and Joints in Timber Structures*; Aicher, S., Reinhardt, H.-W., Garrecht, H., Eds.; Springer Netherlands: Dordrecht, 2014; pp. 713–723 ISBN 978-94-007-7810-8.
21. Cook.A, R. Behavior of Chemically Bonded Anchors. *Journal of Structural Engineering* **1993**, *119*, 2744–2762, doi:10.1061/(ASCE)0733-9445(1993)119:9(2744).
22. Subramanian, N.; Cook, R.A. Installation, Behaviour and Design of Bonded Anchors. *The Indian Concrete Journal* **2002**, *76*, 47–56.
23. Muñoz, R.; Lourenço, P.B.; Moreira, S. Experimental Results on Mechanical Behaviour of Metal Anchors in Historic Stone Masonry. *Construction and Building Materials* **2018**, *163*, 643–655, doi:10.1016/j.conbuildmat.2017.12.090.
24. Riccadonna, D.; Giongo, I.; Schiro, G.; Rizzi, E.; Parisi, M.A. Experimental Shear Testing of Timber-Masonry Dry Connections for the Seismic Retrofit of Unreinforced Masonry Shear Walls. *Construction and Building Materials* **2019**, *211*, 52–72, doi:10.1016/j.conbuildmat.2019.03.145.
25. Porcarelli, S.; Shedde, D.; Wang, Z.; Ingham, J.M.; Giongo, I.; Dizhur, D. Tension and Shear Anchorage Systems for Limestone Structures. *Construction and Building Materials* **2021**, *272*, 121616, doi:10.1016/j.conbuildmat.2020.121616.
26. Giresini, L.; Puppio, M.L.; Taddei, F. Experimental Pull-out Tests and Design Indications for Strength Anchors Installed in Masonry Walls. *Mater Struct* **2020**, *53*, 103, doi:10.1617/s11527-020-01536-2.
27. Lucchini, A.; Mazzucchelli, E.S.; Mangialardo, S.; Persello, M. FAÇADISM AND CLT TECHNOLOGY: AN INNOVATIVE SYSTEM FOR MASONRY CONSTRUCTION REFURBISHMENT. **2014**, doi:10.13140/2.1.3510.8163.
28. Maduh, U.J.; Shedde, D.; Ingham, J.; Dizhur, D. In-Plane Testing of URM Wall Panels Retrofitted Using Timber Strong-Backs.; Newcastle, 2019; p. 13.
29. Busselli, M.; Cassol, D.; Prada, A.; Giongo, I. Timber Based Integrated Techniques to Improve Energy Efficiency and Seismic Behaviour of Existing Masonry Buildings. *Sustainability* **2021**, *13*, 10379, doi:10.3390/su131810379.
30. Ganbaatar, A.; Mori, T.; Inoue, R.; Danzandorj, S. Strength Performance of the Connection between Brick and SPF Lumber. *Buildings* **2022**, *12*, 465, doi:10.3390/buildings12040465.

31. ASTM C67/C67M - 20 *Test Methods for Sampling and Testing Brick and Structural Clay Tile*; 2020;
32. ASTM C349-18 *Test Method for Compressive Strength of Hydraulic-Cement Mortars (Using Portions of Prisms Broken in Flexure)*;
33. ASTM C348-20 *Test Method for Flexural Strength of Hydraulic-Cement Mortars*;
34. ASTM C128-01 *Standard Test Method for Density, Relative Density (Specific Gravity), and Absorption of Fine Aggregate*;
35. CEN 1052-3 *Methods of Test for Masonry - Part 3: Determination of Initial Shear Strength. European Standard*; European Committee for Standardization: Brussels: Belgium, 2002;
36. ASTM C1314-18 *Test Method for Compressive Strength of Masonry Prisms; Merican Society for Testing and Materials (ASTM): West Conshohochen*; PA,USA, 2018;
37. CEN Eurocode 6-EN 1996-1-1 *Design of Masonry Structures-Part 1-1: General Rules for Reinforced and Unreinforced Masonry Structures*; European Committee for Standardization: Brussels: Belgium, 2005;
38. Architectural Institute of Japan *Standard for Structural Design of Timber Structures*; Tokyo, Japan, 2002;
39. Abi, A.; Jason, V. *Structural Wood Design A Practice - Oriented Approach Using the ASD Method*; John Wiley & Sons: New Jersey, 2007;
40. HILTI *The North American Product Technical Guide, Volume 2: Anchor Fastening, Edition 17*; Hilti, Inc: Dallas Parkway, TX, US;
41. ASTM E754 - 80 *Test Method for Pullout Resistance of Ties and Anchors Embedded in Masonry Mortar Joints*; 2014;
42. ASTM D5764-97a *Test Method for Evaluating Dowel-Bearing Strength of Wood and Wood-Based Products*; 2018;
43. McLain, T.E. Connector Code Development and Application in the United States: Generic Fasteners. In Proceedings of the 1992 International Workshop on Wood Cinnectors; Forest Product Society: Madison, WI, 1993; pp. 52–56.
44. Rolf, E.; Ronald A, C.; Jorg, A. Behavior and Design of Adhesive Bonded Anchors. *ACI Structural Journal* **2006**, *103*, 822–831.
45. NDS 2015, National Design Specification for Wood Construction *General Dowel Equations for Calculating Lateral Connection Values with Appendix A*; Leesburg, VA 20175, 2015;
46. Donald E, B.; Kelly, C.; Zeno, M. *Design of Wood Structures - ASD/LRFD, Eighth Edition (8th Ed.)*; 8th ed.; McGraw-Hill Education, 2019; ISBN 978-1-260-12868-0.
47. Ganbaatar, A.; Mori, T.; Matsumoto, S.; Inoue, R. Reinforced Effect on Brick Wall Using Timber Wall as a Retrofitting Method. **2022**, 26.
48. Wilding, B.V.; Beyer, K. Prediction of stiffness, force and drift capacity of modern in-plane loaded URM walls: Vorhersage von Steifigkeit, Festigkeit und horizontaler Verformungskapazität von unbewehrten Mauerwerksscheiben. *Mauerwerk* **2018**, *22*, 77–90, doi:10.1002/dama.201800001.
49. Turnšek.V; Čačovič.F Some Experimental Results on the Strength of Brick and Block Masonry Walls. In Proceedings of the In Proceedings of the 2nd International Brick and Block Masonry Conference; Stoke-on-Trend, 1971; pp. 149–156.

50. Elghazouli, A.Y.; Bompa, D.V.; Mourad, S.A.; Elyamani, A. In-Plane Lateral Cyclic Behaviour of Lime-Mortar and Clay-Brick Masonry Walls in Dry and Wet Conditions. *Bull Earthquake Eng* **2021**, *19*, 5525–5563, doi:10.1007/s10518-021-01170-5.
51. Miha, T. *Earthquake-Resistance Design of Masonry Buildings*; Imperial College Press, 1999; Vol. Vol.I; ISBN 1-86094-066-8.
52. Messali, F.; Esposito, R.; Ravenshorst, G.J.P.; Rots, J.G. Experimental Investigation of the In-Plane Cyclic Behaviour of Calcium Silicate Brick Masonry Walls. *Bull Earthquake Eng* **2020**, *18*, 3963–3994, doi:10.1007/s10518-020-00835-x.
53. CEN Eurocode 8-EN 1998-3 *In Design of Structures for Earthquake Resistance-Part3: Assessment and Retrofitting of Buildings*; European Committee for Standardization: Brussels: Belgium, 2005;
54. Tuomi, R.L.; McCutcheon, W.J. Racking Strength of Light-Frame Nailed Walls. *J. Struct. Div.* **1978**, *104*, 1131–1140, doi:10.1061/JSDEAG.0004955.
55. McCutcheon, W.J. Racking Deformations in Wood Shear Walls. *Journal of Structural Engineering* **1985**, *111*, 257–269, doi:10.1061/(ASCE)0733-9445(1985)111:2(257).
56. Architectural Institute of Japan *Fundamental Theory of Timber Engineering (in Japanese)*; Tokyo, Japan, 2010;
57. Architectural Institute of Japan *Allowable stress design of wooden framed houses 1 (in Japanese)*; Tokyo, Japan, 2017;

List of publications

Peer review article

Ariunaa Ganbaatar, Takuro Mori, Ryo Inoue, and Sunjidmaa Danzandorj. “Strength Performance of the Connection between brick and SPF lumber”. Building Structures. Buildings 2022 12 (4), 465.

Ariunaa Ganbaatar, Takuro Mori, Shinya Matsumoto, and Ryo Inoue. “Reinforced Effect on Brick Wall Using Timber Wall as A Retrofitting Method”. Building Structures. Buildings 2022 12 (7), 978.

Conference papers

Ariunaa Ganbaatar, Takuro Mori, Ryo Inoue and Sunjidmaa Danzandorj. “Experimental Study of Seismic Enhancement Technique for Brick Masonry Walls by Using Wooden Wall Part 1: Strength performance of the connection between brick and lumber” 17th World Conference of Earthquake Engineering, Sendai, Japan. 2021.9